University of Calgary

PRISM Repository **https://prism.ucalgary.ca**

The Vault Open Theses and Dissertations

2015-04-24

Permeability Characterization and Prediction in a Tight Oil Reservoir, Edson Field, Alberta

Di, Jianwei

Di, J. (2015). Permeability Characterization and Prediction in a Tight Oil Reservoir, Edson Field, Alberta (Master's thesis, University of Calgary, Calgary, Canada). Retrieved from https://prism.ucalgary.ca. doi:10.11575/PRISM/27310

http://hdl.handle.net/11023/2165

Downloaded from PRISM Repository, University of Calgary

UNIVERSITY OF CALGARY

Permeability Characterization and Prediction a Tight Oil Reservoir, Edson Field, Alberta

by

Jianwei Di

A THESIS
SUBMITTED TO THE FACULTY OF GRADUATE STUDIES
IN PARTIAL FULFILMENT OF THE REQUIREMENTS FOR THE
DEGREE OF MASTER OF SCIENCE

GRADUATE PROGRAM IN CHEMICAL AND PETROLEUM ENGINEERING

CALGARY, ALBERTA

APRIL, 2015

© Jianwei Di 2015

ABSTRACT

Extremely low and heterogeneous permeability is an important characteristic of tight oil reservoirs and poses major challenges to predict. The aim of this work is to develop a permeability predictor based on a tight area of the Cardium Formation, Edson Field, Alberta using log and core measurements from one well.

Experimental design analysis indicates that the deep resistivity, GR, and SGR logs show stronger correlation with permeability than other conventional wireline measurements. We also tested a literature permeability estimation model designed for tight formations using conventional well logs which worked better in the shaly siltstone ($R^2 = 0.94$) than the shale and conglomerate ($R^2 < 0.5$) facies.

Among the less conventional logs run in this well, we used the NMR log to predict permeability. A pore size-related lithofacies model was built based on the T_2 spectrum decomposition. It gave accurate lithofacies proportion estimates based on our core analysis and data from published studies. Integrating the NMR analysis with probe permeability, our approach provides a 'bridge' to connect the permeability between the probe scale (<1 cm laminations) and core size (>15 cm thin beds) samples.

ACKNOWLEDGMENTS

I would like to express my deepest gratitude to my supervisor professor Jerry L. Jensen for his help, invaluable assistance, and patient guidance during my study. Without his support, I could not have accomplished this work. I wish to thank the whole TOC group, Dr. Clarkson, Dr. Krause, Dr. Pedersen…. I would like to thank Santanu Bhowmik for sample analyses in Dr. Clarkson's lab.

Also, I would like to thank all my colleagues including Mammad Mirzayev, Kushagra Kakar, Mohammad Soroush, and Maryam Moghadasi for their help.

My thanks also go to Dr. Kantzas, Dr. Clarkson and Dr. Meyer for giving me their valuable time to review my thesis.

Funding for this project was provided by the Tight Oil Consortium (TOC). This support is gratefully acknowledged.

Finally, I would like to thank my family for their love and support.

TABLE OF CONTENTS

ABSTRACT iii

ACKNOWLEDGMENTS iii

TABLE OF CONTENTS iv

LIST OF FIGURES vi

LIST OF TABLES x

CHAPTER 1: INTRODUCTION 1

1.1 Background 1

1.1.1 Cardium Formation Review 2

1.1.2 Challenges in Permeability Characterization for the Tight Cardium 4

1.2 Literature Review 9

1.2.1 Core-based Permeability Prediction 9

1.2.2 Conventional Log Permeability Prediction 10

1.2.3 NMR-based Permeability Prediction 12

1.3 Data Available 14

1.4 Methods Overview 15

CHAPTER 2: CORE STUDY AND LITHOFACIES ANALYSIS 18

2.1 Lithofacies Characterization 18

2.2 Core and Well Log Depth Matching 21

2.3 Core Petrophysical Analysis 26

2.4 Mineralogical Compositions Analysis—XRD 32

2.5 Conglomerate Permeability Analysis 38

CHAPTER 3: PERMEABILITY CHARACTERIZATION AND PREDICTION USING CONVENTIONAL LOGS 43

3.1 Permeability Distribution and Variability 43

3.2 Experimental Design 47

3.2.1 Single Factor 51

3.2.2 Two-Factor Analysis 55

3.3 Literature Permeability Calculation Model 56
3.4 Semivariogram Analysis 59

CHAPTER 4: COMBINING NMR LOG AND PROBE PERMEABILITY TO PREDICT WHOLE CORE PERMEABILITY 66

4.1 Introduction 66
4.2 Data Set Description 67
4.3 NMR T_2 Processing for Lithofacies Proportions 69
4.3.1 NMR Response Physics 69
4.3.2 Pore Size Distributions and T_2 72
4.4 Model Testing 74
4.5 Permeability Prediction 79
4.6 Discussion 88
4.7 Conclusions 89

CHAPTER 5: SUMMARY, CONCLUSIONS, AND FURTHER WORK 90

5.1 Summary 90
5.2 Future Work 92

REFERENCE 94

APPENDIX 1 99

APPENDIX 2 100

APPENDIX 3 101

LIST OF FIGURES

Figure 1.1. Middle Cardium deposition plot (from WCSB, Atlas). 2
Figure 1.2. Unconventional and conventional formations permeability range, including core samples from the Cardium (Modified from US Department of Energy). 2
Figure 1.3. History of oil and bitumen production from Western Canada (from Canadian Association of Petroleum Producers)..... 4
Figure 1.4. Cardium tight oil production and well counts (from Divestco). 4
Figure 1.5. Vertical whole core permeability measurements in the Cardium Formation... 5
Figure 1.6. A) The gamma ray log measurement; B) core image; C) the probe permeability in the same core from the Cardium A..... 6
Figure 1.7. Horizontal whole core measurement and probe permeabilities compare from the Cardium A..... 7
Figure 1.8. The ratio of horizontal to vertical permeability (k_{90}/k_{vert}) in the Cardium A... 8
Figure 1.9. A) Box and whisker permeability plot of two similar facies in the Cardium A; B) two similar facies core photos..... 8
Figure 2.1. A) Study area location (from www.canadianoilstocks.ca) B) study well location (from Accumap)..... 19
Figure 2.2. Distribution of the grain diameters of the Cardium A conglomerate..... 20
Figure 2.3. Distribution of the grain diameters of the Cardium B conglomerate. 20
Figure 2.4. Lithofacies change in the study well (modified from Mageau et al., 2012)... 21
Figure 2.5. Raw core (samples every 4 to 5 cm) and well log (samples ~20 cm) GRs before depth matching in the Cardium Formation..... 22
Figure 2.6. Core and well log GRs after depth matching in the Cardium Formation..... 22
Figure 2.7. Core and well log densities after 2.5m shift in the Cardium Formation. 23
Figure 2.8. Density log versus core porosity in the Cardium A. 24
Figure 2.9. One homogenous core sample from the Cardium A. 24
Figure 2.10. GR comparison between 2.5 m and 2.1 m shift. 24
Figure 2.11. Density log comparison between 2.5 m and 2.1 m shift. 25
Figure 2.12. NMR T_2 versus probe k in the Cardium A..... 26
Figure 2.13. NMR T_2 versus probe k in the Cardium B. 26
Figure 2.14. Whole core porosity versus whole core permeabilities in Cardium A. The k_{max} of one sample was not measured..... 27
Figure 2.15. k_v/k_{90} versus porosity in the Cardium A (The line approximates the trend). 28
Figure 2.16. Whole core porosity versus whole core permeabilities in the Cardium B. .. 28
Figure 2.17. k_v/ k_{90} versus porosity in the Cardium B..... 29
Figure 2.18. Density log versus core porosity in the Cardium A. 30
Figure 2.19. Density log versus core porosity in the Cardium B..... 30
Figure 2.20. Core analyzed grain density between conglomerate and shale. 31
Figure 2.21. Permeability (k_p and k_{max}) vs. whole core porosity crossplot for the Cardium Formation. For the probe permeability, the arithmetic average is calculated for each whole core sample..... 32
Figure 2.22. XRD mineral analysis result for Cardium A and B..... 33
Figure 2.23. Clay mineral relative contents of the Cardium Formation. 33
Figure 2.24. 3×11 probe permeability measurement grid..... 34

Figure 2.25. An example of the probe permeability measurements on different grids. ... 34
Figure 2.26. Simple GR log versus lithofacies in the Cardium A. 35
Figure 2.27. Simple GR log versus lithofacies in the Cardium B..... 35
Figure 2.28. XRD clay content versus GR log. 36
Figure 2.29. XRD illite content versus the potassium log. 36
Figure 2.30. The clay and clay minerals relationships with the probe permeability of siltstones in the Cardium A (A. total clay; B. kaolinite; C. chlorite; and D. illite)..... 37
Figure 2.31. GR and SGR relationship with the siltstones permeability in the Cardium A (A. GR; B. potassium; C. uranium; D. thorium)..... 38
Figure 2.32. Box and Whisker plots of conglomerate permeability from the Cardium A and Cardium B, along with their Trask grain size coefficients..... 40
Figure 2.33. Grain volume proportion versus permeability in the conglomerate. 40
Figure 2.34. Schematic of preferential probe flow path to the sample surface (from Meyer and Krause, 2001) 41
Figure 3.1. A) Probability plot of k in the Cardium A; B) Probability plot of log(k) in the Cardium A..... 43
Figure 3.2. A) Probability plot of k in the Cardium B; B) Probability plot of Log(k) in the Cardium B. 44
Figure 3.3. Permeability of the Cardium A and its five intervals. 45
Figure 3.4. A) Log (k) probability plot of interval 1 and 5; B) Log (k) probability plot of interval 3; C) Log (k) probability plot of interval 3; D) Log (k) probability plot of interval 4..... 45
Figure 3.5. Log (k) probability plot of the conglomerate in the Cardium B..... 46
Figure 3.6. Typical well logs and core porosity and permeability in the Cardium A. Track 1: depth. Track 2: GR and caliper logs. Track 3: Density, neutron, and core porosity. Track 4: Array induction resistivity logs. Track 5: SGR logs. Track 6: Probe, horizontal and vertical whole core permeabilities. 48
Figure 3.7. Typical well logs and core porosity and permeability in the Cardium B. Track 1: depth. Track 2: GR and caliper logs. Track 3: Density, neutron, and core porosity. Track 4: Array induction resistivity logs. Track 5: SGR logs. Track 6: Probe, horizontal and vertical whole core permeabilities. 49
Figure 3.8. Plot of different well log effects in the Cardium A (significant factors are shown in circles). 50
Figure 3.9. Plot of different well log effects in the Cardium B (significant factors are shown in circles). 50
Figure 3.10. Deep resistivity (A090) versus permeability in the Cardium A. 52
Figure 3.11. Box and Whisker plots of the permeability (left) and resistivity (right) in similar facies. 52
Figure 3.12. CDF of different log-permeability values in Cardium A. 53
Figure 3.13. Total errors with different resistivity cutoff value. 53
Figure 3.14. CDF of different log-permeability values in Cardium B..... 54
Figure 3.15. Total errors with different GR cutoff values. 54
Figure 3.16. Contour plots of permeability versus A090 and GR in the Cardium A. 55
Figure 3.17. Contour plots of permeability versus potassium and thorium in the Cardium B. 56

Figure 3.18. A) Measured and modeled shaly siltstone k versus depth in the Cardium A; shaly siltstone measured versus modeled k in the Cardium A. 58
Figure 3.19. A) Measured and modeled shale k versus depth in the Cardium A; shale measured versus modeled k in the Cardium A. 58
Figure 3.20. Measured and modeled shale k versus depth in the Cardium B. 59
Figure 3.21. A) measured and modeled conglomerate k versus depth in the Cardium B; B) conglomerate measured versus modeled k in the Cardium B. 59
Figure 3.22. Slip-corrected probe permeability in the Cardium A. 61
Figure 3.23. K_p and Log k_p SV in the Cardium A. 61
Figure 3.24. GR and k_p SVs in Cardium A. 62
Figure 3.25. GR and k_p SVs in Cardium B. 62
Figure 3.26. Actual (above) and processed (below) core imaged from Cardium A. 63
Figure 3.27. Probe permeability SV plot. 64
Figure 3.28. Core image pixel SV plot. 64
Figure 3.29. GR log, core image pixel, and k_p SVs. 65
Figure 4.1. k_p ,k_{max}, and k_{vert} measurements from the Cardium A. 68
Figure 4.2. k_p ,k_{max}, and k_{vert} measurements from the Cardium B. 68
Figure 4.3. Core sample with shale and siltstone laminations showing core permeability measurements and a possible location for a probe permeability measurement (red circle). 69
Figure 4.4. NMR interpretation plot in the Cardium formation (Schlumberger, 2010). .. 70
Figure 4.5. Core, density, and NMR porosities in the Cardium A. 71
Figure 4.6. A) Example decomposition of Cardium B Log T_2 spectrum; B) Nine parameters from the decomposition 74
Figure 4.7. Pore size related lithofacies model and associated responses on the NMR log (T_2) spectrum. 74
Figure 4.8. A) actual conglomerate core image; B) processed conglomerate core image in the Cardium A. 75
Figure 4.9. A) actual tiny laminated shaly siltstone; B) processed tiny laminated shaly siltstone in the Cardium A. 75
Figure 4.10. A) actual conglomerate core image; B, C) processed conglomerate core image in the Cardium B. 76
Figure 4.11. Shale proportion from core image versus α_1, A) is the Cardium A; B) is the Cardium B. 77
Figure 4.12. XRD clay content versus α_1 77
Figure 4.13. NMR experimental results of sand-shale laminations (Minh and Sundaraman, 2006). 78
Figure 4.14. A) Measured (from Minh and Sundaraman, 2006) and modeled log T_2 curves; B) parameters from the decomposition. 78
Figure 4.15. A) Borehole measured (from Minh and Sundaraman, 2006) and modeled log T_2 curves; B) parameters from the decomposition. 79
Figure 4.16. Micropore proportions (collected from Ostroff et al., 1999 Minh and Sundaraman, 2006; Bansal, 2013) versus α_1 from log T_2 decomposition. 79
Figure 4.17. A) Flow along the layers; B) flow across the layers. 80
Figure 4.18. A) T_2 spectrum of very shaly zone ($\alpha_1 = 1$) in Cardium A; B) probe measurement locations on the core. 81

Figure 4.19. Probability plot of probe permeability from facies i = 1 in the Cardium A. 81
Figure 4.20. Probability plot of probe permeability from second and third facies (corrected for shale content) in the Cardium A. 82
Figure 4.21. A) k_{along} versus k_{max} and k_{90}; B) k_{across} versus k_{vert} in the Cardium A. 83
Figure 4.22. A) k_{TIM} versus core permeability; B) k_{SDR} versus core permeability in the Cardium A..... 84
Figure 4.23. 100 k_{along} values created by Monte Carlo in the Cardium A. 85
Figure 4.24. 100 k_{along} created by Monte Carlo in the Cardium A. 85
Figure 4.25. A) k_{along} versus horizontal core permeability (k_{max} and k_{90}) in the Cardium B; B) k_{across} versus vertical core permeability (k_{vert}) in the Cardium B. 87
Figure 4.26. 100 k_{along} values created by Monte Carlo in the Cardium B. 88
Figure 4.27. 100 k_{across} values created by Monte Carlo in the Cardium B..... 88

LIST OF TABLES

Table 1.1. Equations for permeability empirical estimates using core-derived quantities 10
Table 1.2. Permeability calculation prediction models derived from well log measurements 12
Table 1.3. Different data properties (Rider and Kennedy, 2011). 15
Table 2.1. Grain parameter in the conglomerate (red color from the Cardium A; green color from the Cardium B) 42
Table 3.1. Permeability variability parameters. 47
Table 3.2. Parameter values from the Cardium A and B. 57

CHAPTER 1: INTRODUCTION

1.1 Background

This research concerns permeability prediction in low permeability (tight) reservoirs. The analysis and application of our results focus on the Cardium Formation, located in the Western Canadian Sedimentary Basin (WSBC) (Fig. 1.1). Among all the reservoir properties, permeability is one of the most important. Throughout the oil industry process, permeability plays a very important role. Accurate permeability values help to determine the perforation location and length in the early oilfield stage. During the reservoir development, it is useful to optimize injection and production rates, as well as enhanced oil recovery strategies. It is also a critical factor in reservoir simulation and production history matching and prediction, etc. An accurate prediction of permeability is thus essential in the oil industry.

The typical techniques for permeability prediction include core and wire line measurements. Researchers have frequently and successfully investigated these methods in conventional formations for many years. In conventional formations, the permeability usually exceeds 0.1md. However, in the tight Cardium Formation we studied for this project, only a very small proportion of the permeability is greater than 0.1 md. Few parts of relatively clean siltstone and the conglomerate reach this range (Fig. 1.2), while most parts show very low permeability (<0.1 md). Apart from low values, scale and resolution are also big issues in tight formations when the traditional permeability prediction techniques are applied. For example, the plug scale permeability is usually adequate to characterize conventional core. In tight formations, the permeability variations are typically at the cm-scale. Traditional permeability predictors used in tight formations will give large errors without considering these factors properly.

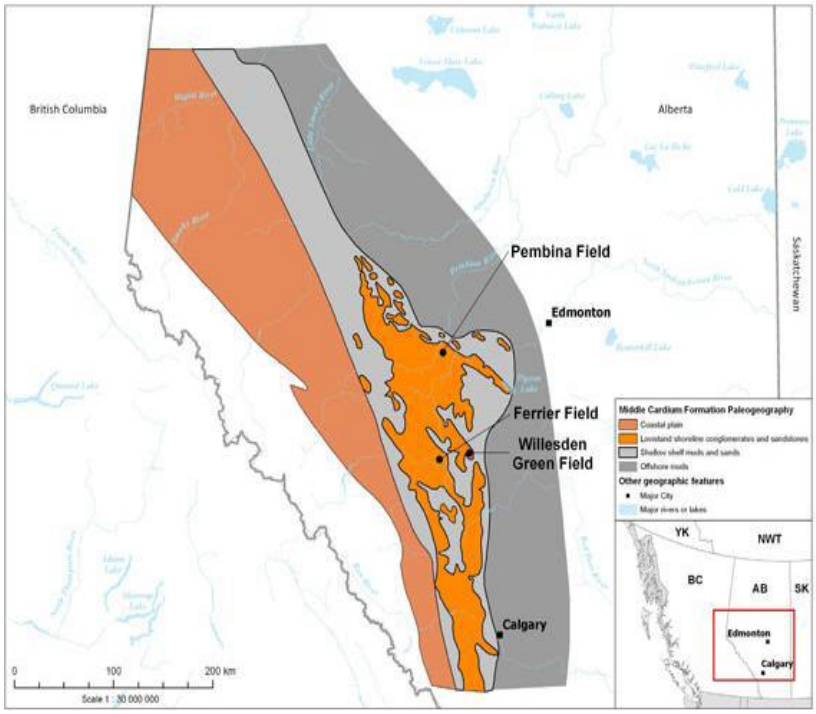

Figure 1.1. Middle Cardium deposition plot (from WCSB, Atlas).

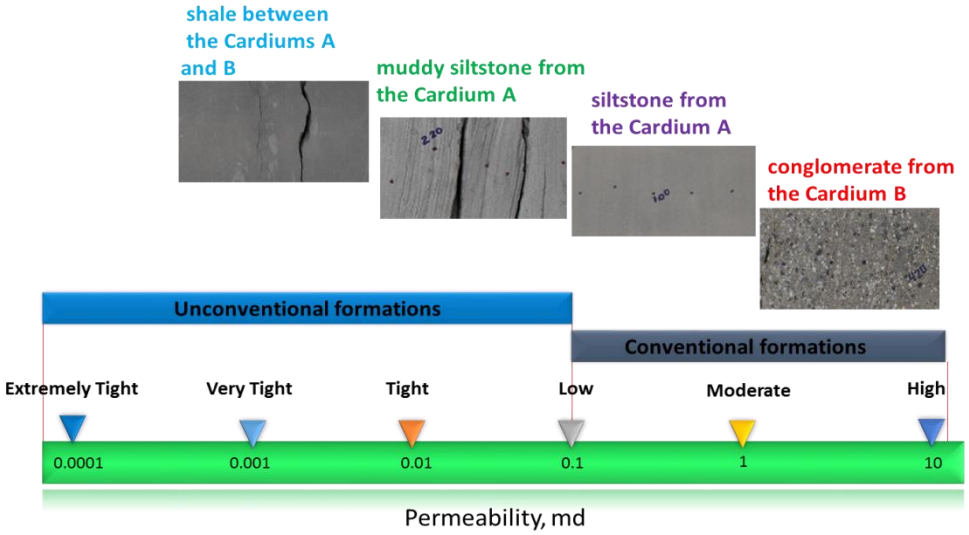

Figure 1.2. Unconventional and conventional formations permeability range, including core samples from the Cardium (Modified from US Department of Energy).

1.1.1 Cardium Formation Review

There were several stages of oil production in the West Canadian Sedimentary Basin (WCSB). The first stage was conventional oil production begun in the 1950s. It increased

quickly and reached a peak in the 1970s. After that, the conventional light oil production steadily declined. The second stage was heavy oil production, including conventional heavy and oil sand raised up, since the 1980s (Fig.1.3). Heavy oil production exceeded the conventional oil in the early 2000s. Because of oil price increasing and technology progress (mainly horizontal wells widely applied), tight oil wells have rapidly developed since 2010 (Fig.1.4). The recent stage in WSBC is tight hydrocarbon production.

A similar trend occurred in the Cardium Formation, which is a very important formation in the WSBC. The Cardium Formation has been a productive formation since it was first discovered in the 1950s (Krause et al., 1994). It was estimated that there are over 1.7 billion m^3 of oil in the Cardium Formation (Energy Resources Conservation Board, 2011). However, previous production mainly came from conventional parts of the Cardium, including high permeability conglomerates and sandstones (Energy Briefing Note, 2011). In recent years, attention has been focused on the tight portions of the Cardium Formation, which were supported by new drilling technology for horizontal wells. Successful application of these new techniques in other tight formations, such as the Bakken formation, increased confidence for the tight Cardium recovery (Clarkson and Pedersen, 2011). The tight Cardium continues to be an important part for the Alberta oil industry.

One recently drilled well from the Cardium Formation in the Edson Field, was processed using the latest well logs, including NMR, and full core analysis. This well provides a rich dataset to attempt permeability characterization in the tight Cardium Formation and this study reports on the analysis of these data.

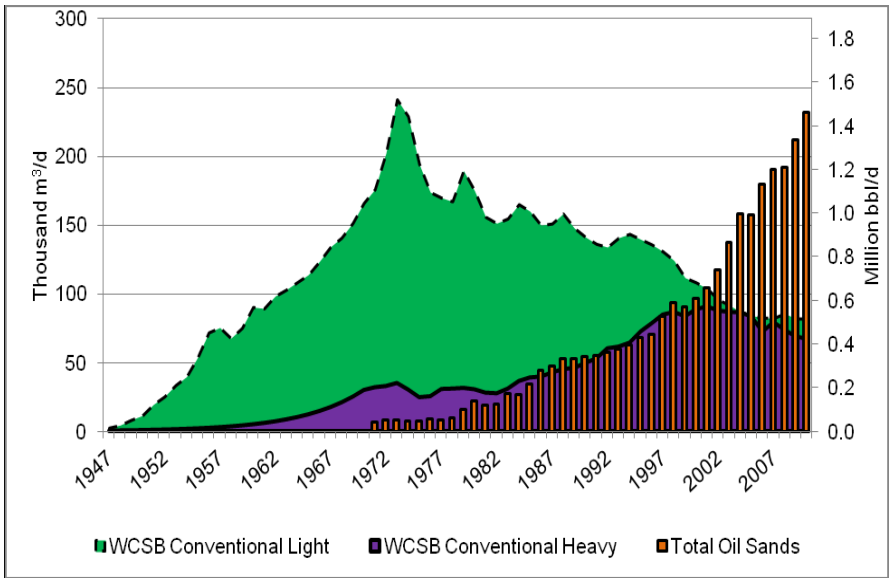

Figure 1.3. History of oil and bitumen production from Western Canada (from Canadian Association of Petroleum Producers)

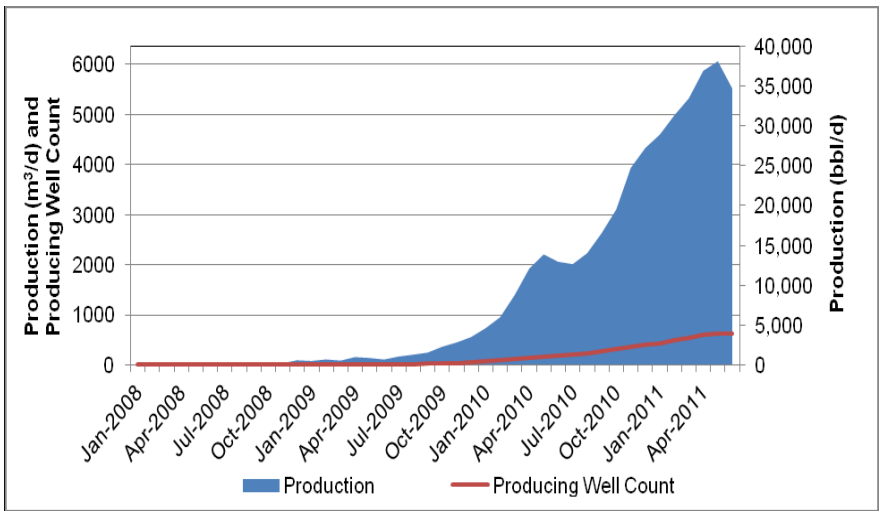

Figure 1.4. Cardium tight oil production and well counts (from Divestco).

1.1.2 Challenges in Permeability Characterization for the Tight Cardium

The permeability estimation is based on two distinct methods, direct and indirect. In this study, the term direct measurement includes profile and press-decay derived permeability. These measurements are based on core samples, including core plugs, core slabs, and full diameter cores. In order to measure the permeability, fluid flow is required. The measurement fluids used in this work are gas. The indirect method mainly consists of wireline logs. All methods have their strengths and weaknesses. The direct techniques

usually give an accurate permeability estimate based on lab conditions. Most measurements ignore the original formation conditions, such as rock stress, wetting condition and reservoir temperature. The downhole well log based prediction keeps the initial reservoir conditions, but its accuracy cannot be guaranteed. In tight formations such as the Cardium, these weaknesses are amplified.

Because of the low permeability in tight formations, how we obtain accurate estimates is important. The permeability value in formations sometimes goes beyond the tool measurement limits. For example, there may be whole core sample measurements taken. Because the lower limit of this measurement is 0.01 md, many measurements only show the maximum permeability of the samples (Fig. 1.5). For these samples, the exact vertical permeability cannot be obtained through the whole core measurement.

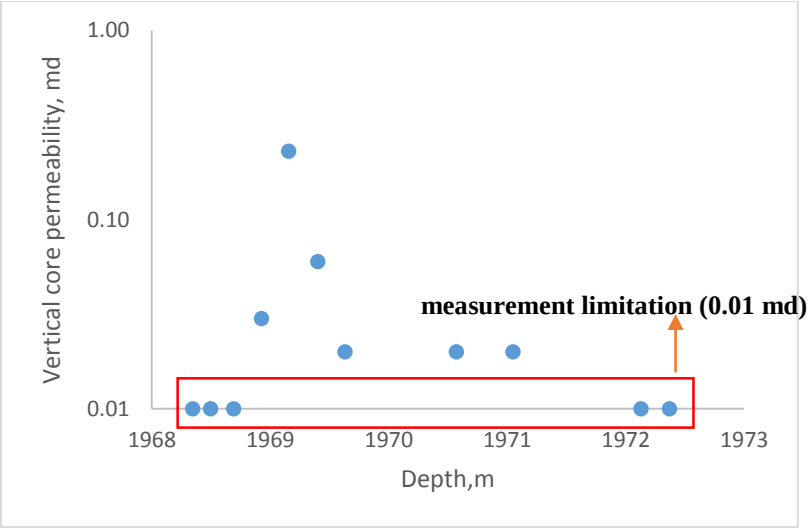

Figure 1.5. Vertical whole core permeability measurements in the Cardium Formation.

Wireline log derived permeability does not explicitly suffer value limitations, but there may be several implicit limitations to its accuracy. One important factor concerns the scale and resolution. Although high resolution logging technology is used today, its resolution is still restricted to a relatively large scale (>20 cm), compared to the cm-scale heterogeneity in tight formations (Solano et al., 2012). There is one 20cm core sample from the Cardium A (Fig.1.6 B). The gamma ray log (GR) shows very mild heterogeneity, which has not presented any significant change (Fig.1.6 A). The probe permeability from the same core sample presents a significant difference, exceeding one

order of magnitude variation (Fig.1.6 C). The well log is impossible to detect the cm-scale change, which affects the permeability in the tight formation.

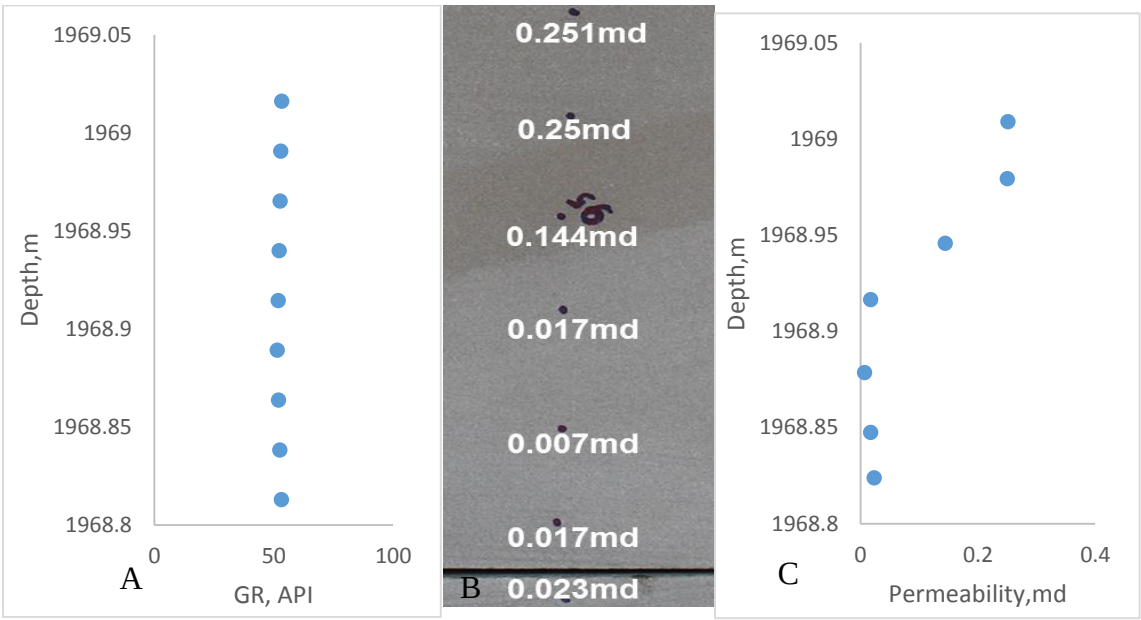

Figure 1.6. A) The gamma ray log measurement; B) core image; C) the probe permeability in the same core from the Cardium A.

This problem remains when comparing lab measurements. For example, when we correlate pulse decay-derived permeability with probe derived permeability values, the scale and resolution problems become particularly important. For example, whole core permeability measurements have larger scales (>15 cm) than the probe permeability (<1 cm). These two techniques give significantly different permeabilities. The horizontal whole core permeability (k_{max}) is larger than the probe result in most samples (Fig.1.7).

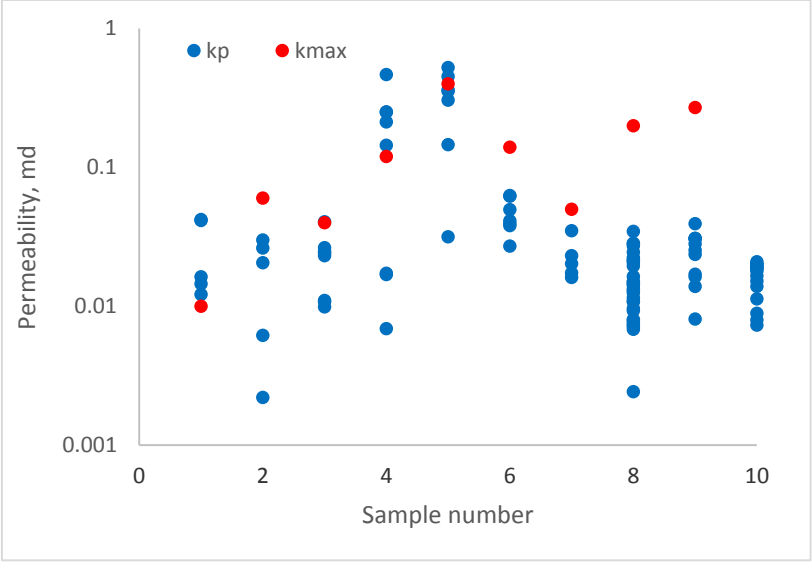

Figure 1.7. Horizontal whole core measurement and probe permeabilities compare from the Cardium A.

Besides the low value and scale problems, the other challenge for permeability characterization of tight formations is heterogeneity. The heterogeneity in this study includes two levels: one is caused by directional anisotropy and another is lithofacies dependent. The permeability anisotropy caused by directions is mainly because of sedimentary structures. In tight formations, the laminations can be up to a few cm thick. These laminations cause large differences between vertical and horizontal permeabilities. The ratio of horizontal to vertical permeability (k_{90}/k_{vert}) can reflect this difference. All the horizontal permeabilities are larger than the vertical values and some differences can reach an order of magnitude (Fig. 1.8). Another reason for the heterogeneity is the facies variations. There are two facies which appear to be similar (Fig. 1-9.B). However, the probe permeability values between them show considerable differences (Fig. 1-9.A).

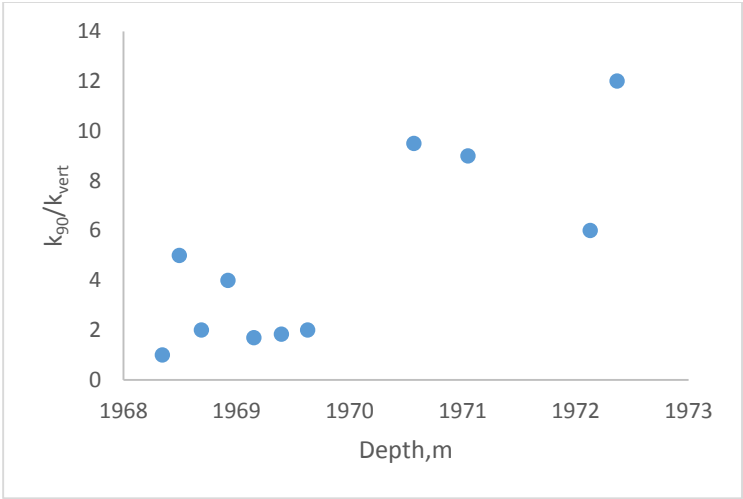

Figure 1.8. The ratio of horizontal to vertical permeability (k_{90}/k_{vert}) in the Cardium A.

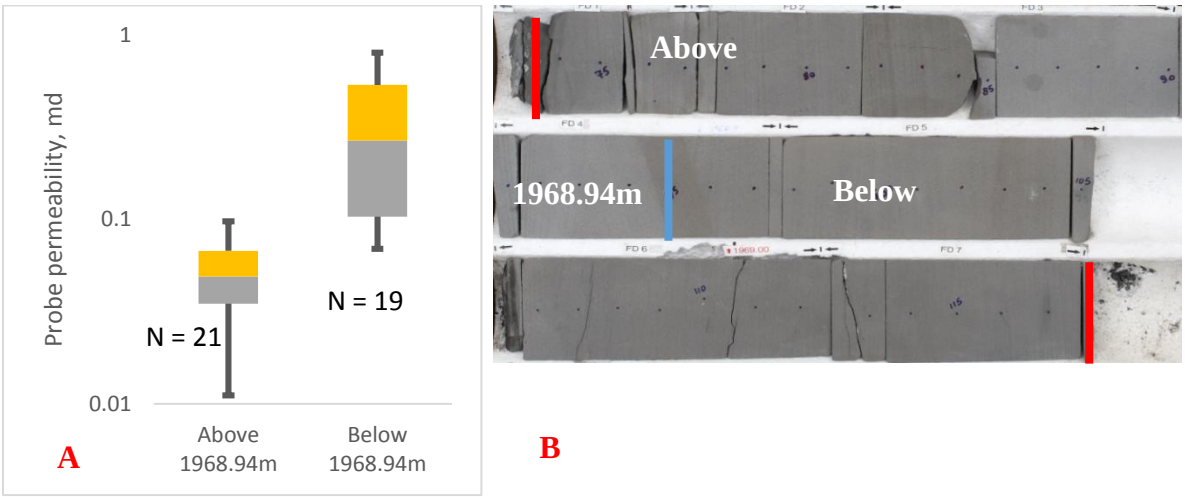

Figure 1.9. A) Box and whisker permeability plot of two similar facies in the Cardium A; B) two similar facies core photos.

There are many errors created when traditional techniques are used for permeability prediction in tight formations. The core based methods give reliable estimates, but suffer from the value limitation and measurement environmental effect. Well log based predictions approach the reservoir conditions, but the result is questionable and the resolution cannot reach the small scale of micro-facies in tight formations. This thesis tries to solve these challenges based on the tight Cardium Formation and provides reference for other tight formations.

1.2 Literature Review

In this work, we focus on different permeability predictions in the tight Cardium Formation. To begin, we discuss permeability estimate methods in the literature from three categories:

1) Permeability prediction from core data
2) Permeability calculation based on conventional logs
3) Permeability estimation from the NMR log

1.2.1 Core-based Permeability Prediction

Many studies have discussed permeability prediction using different methods. For example, Poiseuille (1846), Kozeny (1927), and Carman (1939) developed some theoretical relationships to calculate permeability. But these expressions were based on the assumption of a single capillary tube, which can fail for actual porous rocks. Krumbein and Monk (1942) have investigated the effects of rock properties on permeability. Their study found permeability was proportional to the square of the mean of grain size and the exponential of the standard deviation of the grain size (Eq. 1.1, Table 1.1). Berg (1970) derived a theoretical estimate of permeability which agreed with Krumbein's results (Eq. 1.2). Shepherd (1989) summarized previous work and proposed a simple equation between grain size and permeability (Eq. 1.3). But, in tight formations, it is difficult to directly measure the grain size distribution.

Several studies found that porosity (ϕ) and residual water saturation (S_{wi}) have shown good correlations with permeability. Wyllie and Rose (1950) developed a simple empirical expression using ϕ and S_{wi} (Eq. 1.4). But, they reported that it was impossible to find an accurate general constant for all situations. Morris and Biggs (1967) also determined an estimate for permeability using ϕ and S_{wi} (Eq. 1.5). In their equation, they recommended the c = 250 and 79 for oil and gas, respectively. Timur (1968) obtained an empirical formula for permeability calculation from laboratory tests (Eq. 1.6). He processed 155 sandstone samples with different relations and found Eq. 1.6 has the highest coefficient of determination (R^2) and the lowest error, compared to other equations. These equations are accurate in relatively clean, consolidated sandstone with

medium porosity (15% - 25%) (Coates and Dumanoir, 1973). In the tight Cardium Formation, the unique and clean lithofacies is uncommon and shale plays an important role, which impairs the accuracy of these relationships.

Table 1.1. Equations for permeability empirical estimates using core-derived quantities

Authors	Permeability Correlations	Parameters	Eq.
Krumbein and Monk, 1942	$k = N \cdot D^2 \exp(-\mathrm{a} \cdot \sigma)$	D mean of grain size; σ standard deviation of the grain size	1.1
Berg,1970	$k = 5.1 \times 10^{-6} \phi^{5.1} D \exp(-\mathrm{a} \cdot \sigma)$	D mean of grain size; σ standard deviation of the grain size;ϕ porosity	1.2
Shepherd, 1989	$k = c \cdot D^2$	D mean of grain size	1.3
Wyllie and Rose, 1950	$k^{1/2} = c_1 \frac{\phi}{S_{wi}} + c_2$	ϕ porosity; S_{wi} irreducible	1.4
Morris and Biggs, 1967	$k^{1/2} = c \frac{\phi^3}{S_{wi}}$	ϕ porosity; S_{wi} irreducible	1.5
Timur, 1968	$k = 0.136 \cdot \frac{\phi^{4.4}}{S_{wi}^2}$	ϕ porosity; S_{wi} irreducible	1.6

1.2.2 Conventional Log Permeability Prediction

Yao and Holditch (1993) compared the cost of permeability estimates from cores and well logs. The costs from core analysis were nearly 10 times greater than well logs. So many attempts have been made to find well log permeability predictors. Some investigators derived specific correlations (Table 1.2).

Tixier (1949) first used electric logs to calculate the permeability. He introduced the resistivity gradient concept ($\frac{\triangle R}{\triangle h}$). The parameters, besides the resistivity gradient in his model, also included the sample resistivity and the oil and water densities (Eq. 1.7). This

model was assumed applicable only in homogeneous sandstones without significant amounts of shale.

Coates and Dumanoir (1973) also used resistivity logs to estimate the permeability. In their model, they also included the porosity and cementation and tortuosity factor w (Eq. 1.8). The key and difficult point of this model was the determination of the parameter w.

Yao and Holditch (1993) presented a method to calculate permeability using well log data in tight formations. The model included porosity, deep and shallow resistivities, and GR (Eq. 1.9) and showed a moderate to strong correlation with core permeability, $R^2 > 0.7$.

Saner et al. (1997) established an experimental estimator for permeability with water saturation and resistivity, which were determined by resistivity well log data. The study was done using carbonate samples. They gave one simple relation between formation factor and permeability (Eq. 1.10).

Mohaghergh et al. (1997) developed a multiple regression model using gamma ray, bulk density and deep resistivity to calculate the permeability (Eq. 1.11).

Xue et al. (1997) used sonic travel time (Δt), density porosity (ϕ_d), gamma ray (GR), and ratio of deep resistivity to shallow resistivity (RR) as variables to predict the permeability (Eq. 1.12). But this model gave a weak correlation with core results, $R^2 = 0.49$. Then they applied the alternating conditional expectation (ACE) technique to find one more optimal multiple regression function. The ACE actually increased the model regression from $R^2 = 0.49$ to $R^2 = 0.62$, which was not a significant increase.

Lim et al. (2004) used a fuzzy logic technique to rank the effects of well logs on permeability. They found the sonic, GR and density logs were most important for permeability.

These methods were mainly used in conventional formations, and sometimes required relatively “clean” formation. So applications of these models were mostly suitable for high permeability or specific areas. It is difficult to directly copy and apply these relationships in the Cardium tight reservoir. Among these reports, only the geological conditions from Yao and Holditch (1993) are similar to the Cardium tight formation. So in this thesis, their model will be selected as one potential method to use.

Table 1.2. Permeability calculation prediction models derived from well log measurements

Authors	Equations	Parameters	Eq.
Tixier, 1949	$k = C(\frac{2.3}{R_o(\rho_w - \rho_o)}\frac{\Delta R}{\Delta h})$	R_o sample resistivity; ρ density; ΔR/Δh resistivity gradient	1.7
Coates and Dumanoir, 1973	$k^{1/2} = \frac{c}{w^4}(\frac{\phi^{2w}}{R_w / R_t})$	w tortuosity factor; R_w ,R_t water and true resistivity	1.8
Yao and Holditch,1993	$k = \frac{\phi^{e1}(1-\mathrm{I}_{GR})^{e2} R_{ild}{}^{e3}}{(R_{ild} / R_{sfl})^{e4}}$	I_{GR} gamma log index; R_{ild},R_{sfl} deep ,shallow resistivity	1.9
Saner et al.,1997	$\log(\mathrm{k}) = 7.04 - 4.19 * \log(\mathrm{F})$	F formation factor	1.10
Mohaghergh et al.,1997	$k = 126.5 + 0.001 * R_t - 50.3 * \rho_D$ $+0.06 * I_D$	R_t deep resistivity; ρ_D bulk density; I_{GR} gamma log index	1.11
Xue et al.,1997	$\log(\mathrm{k}) = 0.15\Delta\mathrm{t} - 0.019\phi_d -$ $0.039GR + 0.022RR - 7.73$	Δt sonic travel time; ϕ_d density porosity; GR gamma ray; RR ratio of deep resistivity to shallow resistivity	1.12

1.2.3 NMR-based Permeability Prediction

Apart from conventional log measurements, the NMR log is playing an important role in recent permeability prediction efforts. Coates et al. (2000) introduced an NMR-based permeability prediction model based on Eq. 1.5 in Table 1.2. The model needs to determine the residual water saturation, which depends on the transverse relaxation time cutoff (T_2 cutoff) selection. Usually the value 33 ms is chosen for the T_2 cutoff in sandstone, which is an overestimation in our tight formation compared to the core measured S_{wi}. So this model applied in tight formations will underestimate the permeability. Another commonly used model was called the SDR model by Kenyon et al. (1988, 1997). This model works well in conventional clean water zones. There are drawbacks of the SDR model used in tight formations, however. For example, the porosity from the NMR usually is underestimated, compared to core porosity in tight formations (see below Fig.4.6 in Chapter 4). Besides these two empirical models, Lowden (2003) used a thickness-weighted permeability calculation model with the NMR

log. The weights of different facies determination were based on the 'typical' sand zone assumption. He divided the formation into clean sand, silt, and shale parts according to the GR value < 30 API, 30-100 API, and > 100 API, respectively. But in the Cardium Formation and many other tight reservoirs, there are not clean sand zones. Even the cleanest silt intervals still have over 10% clay in the Cardium Formation. So this method will overestimate the sand weights and permeability. Another weakness of this method is ignoring the shale permeability. Because it was used in conventional formations, the shale permeability was assumed zero, which is unrealistic in tight formations.

Genty et al. (2007) decomposed the log (T_2) spectrum into at most three Gaussian components and got nine parameters, which were used to identify pore and porosity types in carbonate rocks. For the NMR well log, the dominant T_2 time is directly proportional to the pore size, ignoring fluid effects (Coates et al. 1999). For pore size, many studies have demonstrated that the lognormal probability density function (PDF) is the best fitting. The mercury intrusion porosimetry (MIP) method has found pore size to be lognormal distribution (Diamond and Dolch, 1971, 1972; Shi, Brown and Ma, 1991). Lindquist and Venkatarangan (2001) again found the lognormal PDF for sandstone pore sizes using X-ray tomographic image analysis. Another technique called mercy injection capillary pressure testing (CMICPT), used by Chuanyan et al. (2013), and also showed the lognormal PDF of pore size in very tight core samples. In a heterogeneous rock with several rock types, we can therefore expect that the T_2 spectrum will consist of a mixture of lognormally distributed pore size components. That is, the log (T_2) distribution will be assumed to consist of normal (Gaussian) components of various amplitudes, means, and standard deviations.

In this research, we applied the NMR decomposition method of Genty et al. (2007) for permeability prediction. Based on parameters from a similar decomposition, we build a pore size-related lithofacies model (fine size- shale, medium size – fine silt, and coarse size – coarse silt or sand) and verified by core image. XRD, and some literature data. In order to calibrate the model, some probe permeability data are used to identify facies permeabilities. Arithmetic and harmonic permeability using the model was calculated to compare with whole core permeability (k_{max}, k_{90} and k_{vert}).

1.3 Data Available

The data used in this study can be divided into four categories according to their relationships with permeability (Fig. 1.10). All the data come from well 4-33-053-18 in the Edson Field.

1. Lab measurements of permeability, which include the whole core (k_{90}, k_{max}, and k_{vert}) and probe (k_p) permeabilities. The whole core measurements were performed by the Core Laboratories Canada, in 2010. The probe permeability was measured in the lab of University of Calgary, in 2012.
2. Rock petrophysical, textural, and compositional properties, such as porosity, grain size, clay volume, and XRD (X-ray diffraction) analysis. The XRD result was measured by Core Laboratories Canada, in 2011.
3. Conventional well logs, such as GR, SGR, resistivity, and density logs. All these logs were measured by Schlumberger, in 2010.
4. NMR well log T_2 spectrum, which is digitized from the NMR log interpretation plot.

The vertical resolutions and investigation depths of different data sources are variable and need to be taken into account. For example, well logs can only capture bed scales (>15 cm); however, probe permeability can distinguish small laminations (<1 cm) (Table 1.3).

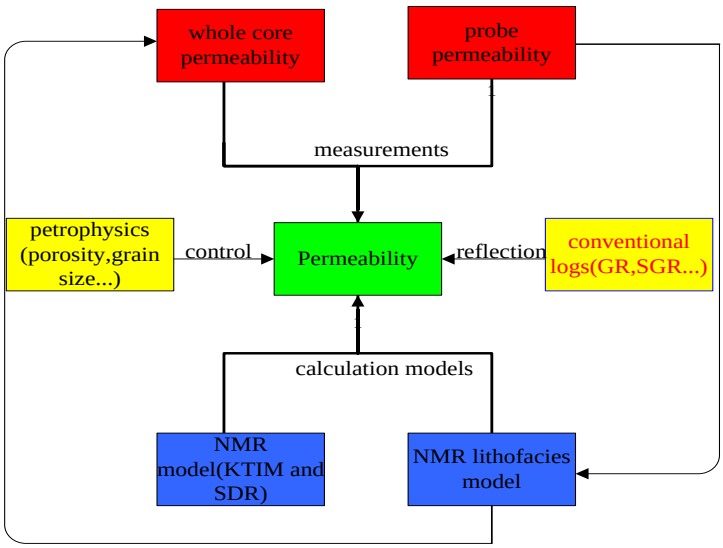

Figure 1.10. Available data in this research.

Table 1.3. Different data properties (Rider and Kennedy, 2011).

Data		Vertical Resolution (cm)	Investigation depth (cm)
Whole core measurement		>15	10
Probe k		0.6	0.6
Conventional logs	GR	30-40	10-15
	Density	10-40	<10
	Neutron	50	15-25
	Array Inductions	20	>25
	Sonic	>50	>20
NMR		15	1.3-3.2

1.4 Methods Overview

This thesis can be divided into three main parts: lithofacies and core analysis, conventional logs-permeability calibration, and NMR prediction for permeability. Different methods and techniques are used.

- Lithofacies and core analysis
  - The pore throat aperture (r_{p35}) proposed by Aguilera (2002) has been used for pore throat radius characterization in both conventional and tight formations. r_{p35}s are calculated using core data (k_p, k_{90}, and core porosity) and compared with literature results.
  - There are many important statistical properties of permeability, which include its PDF and variability. Probability plots will be used to assess the permeability distribution and coefficients of variation (C_v) to describe the permeability heterogeneity.
  - X-ray diffraction (XRD) techniques provided content of different minerals, including relative amount of clay minerals. The spectral gamma ray (SGR) log can also be used to identify and distinguish clay minerals. These two measurements should be associated.

- From XRD analysis, clay contents have been measured. In order to decrease measurement uncertainties, we choose locations where XRD were measured and draw 3 × 11 grids. So there are 33 probe measurements at every XRD sampled location. After this, we check the effect of clay contents on permeability.

- Conventional logs for permeability prediction
  - Conventional logs are potential predictors for permeability. It is critical to choose factors which are significant to permeability. Factorial design can help to select potential and important permeability predictors.
  - Take significant impact factors from factorial design and check their relationships with permeability. If there are no clear relationships, calculate conditional probabilities of different permeability occurrences.
  - If there are no clear relations between logs and permeability, use semivariogram model to connect well logs, probe permeability and core data.
  - Apply Yao and Holditch (1993) permeability calculation model to the Cardium formation.
- NMR log for permeability
  - From NMR well logs, T_2 spectrum can be obtained. Because log pore size has been observed to have a Gaussian distribution and T_2 is proportional to pore size, the NMR T_2 spectrum can be decomposed into at most three Gaussian components. Then the Gaussian parameters can be obtained. Because different T_2 values represent pore sizes, a pore size related lithofacies model can be proposed.
  - Core image analysis is used to determine shale proportion. According to the color differences, specific facies volume proportions can be calculated. Core image analysis results are compared to facies ratio from the T_2 decomposition.
  - In order to calibrate the model, some probe permeability data are used to identify facies permeabilities. Arithmetic and harmonic averaged

permeabilities using the model can be calculated to compare with whole core permeabilities (k_{max}, k_{90} and k_{vert}).

- In order to decrease uncertainty of the result, Monte Carlo will be used to assess the variability.

CHAPTER 2: CORE STUDY AND LITHOFACIES ANALYSIS

2.1 Lithofacies Characterization

The Cardium Formation is divided into two units: the Pembina River Member (deeper) and the Cardium Zone Member (shallower) (Krause and Nelson, 1984). The Pembina River member can be further sub-divided into two separate parts: the Cardium A and Cardium B (Krause et al., 1994; Mageau et al., 2012). The lower sequence is the Cardium B interval, also called the lower Pembina River Member. The upper Pembina River is the Cardium A. The Cardium A and Cardium B usually are separated by a shale section. The Cardium A was deposited in a relatively broader, shallow shelf, shoreface and coastal plain environment, making the facies more uniform and cleaner than the Cardium B (Mageau et al., 2012). The Cardium A starts with a conglomerate interval with its thickness varying from several centimeters to meters. Below the conglomerate is a relatively clean siltstone with high porosity and permeability, which is typically the main target for hydrocarbon exploration. Below the clean siltstone, the lithofacies become more muddy or argillaceous, decreasing the porosity and permeability. The lower portion of the Cardium A is a "pure" shale interval. A thick conglomerate interval forms the top of the Cardium B. Different from the Cardium A, the conglomerate has better sorting and higher porosity and permeability. Below the conglomerate, the Cardium B changes to shale or muddy siltstone.

This research is based on a new well 00/4-33-053-18 W5M/0 in the Edson field, which was drilled by Talisman in 2010 (Fig. 2.1). In this well, the depth of the Cardium A is from 1967m to 1975m. I viewed the core and made the following observations.

1. At the top, there is about 0.4 m matrix-supported conglomerate. The sorting is poor and the grain size varies from 1mm to 20mm. Most grains (>65%) have diameters 1 mm to 3 mm (Fig. 2.2). The permeability varies from 0.01 md to 0.2 md (Fig. 2.4).
2. There are about 2 m relatively clean siltstones, with high porosity (~10%) and permeability (0.1 to 0.5 md). The remains are very muddy siltstone intervals in

the Cardium A, which decrease the porosity and permeability by about 40% and 90%, respectively (Fig. 2.4).

Between the Cardium A and Cardium B, there is about 17m of shale. Below the shale interval, the Cardium B starts as 2.5m conglomerates. Compared with the Cardium A, the conglomerate in the Cardium B is mainly clast-supported, better sorted and rounded. Most grain diameters are between 1 mm and 2 mm (>90%) (Fig. 2.3). The permeability is higher than the Cardium A, with a range of 0.1 to 40 md (Fig. 2.4). Homogenous shale, with permeability of approximately 0.01md, is then below the conglomerate in the Cardium B. The lithofacies and main permeability variation in the study well are shown in Fig. 2.4.

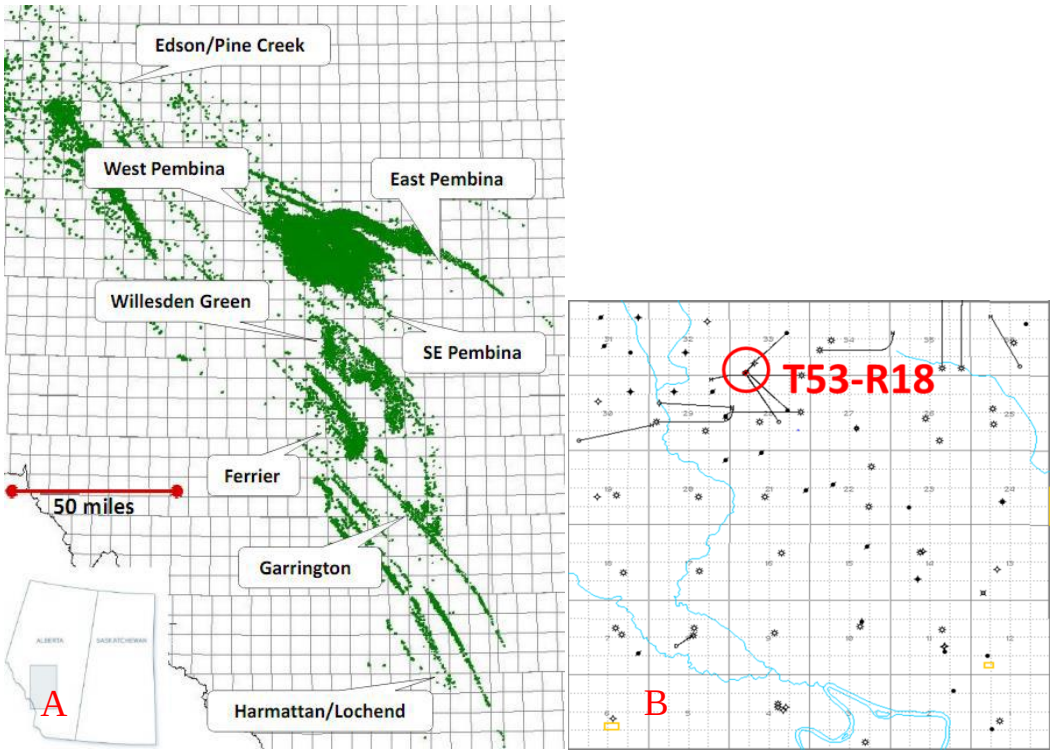

Figure 2.1. A) Study area location (from www.canadianoilstocks.ca) B) study well location (from Accumap).

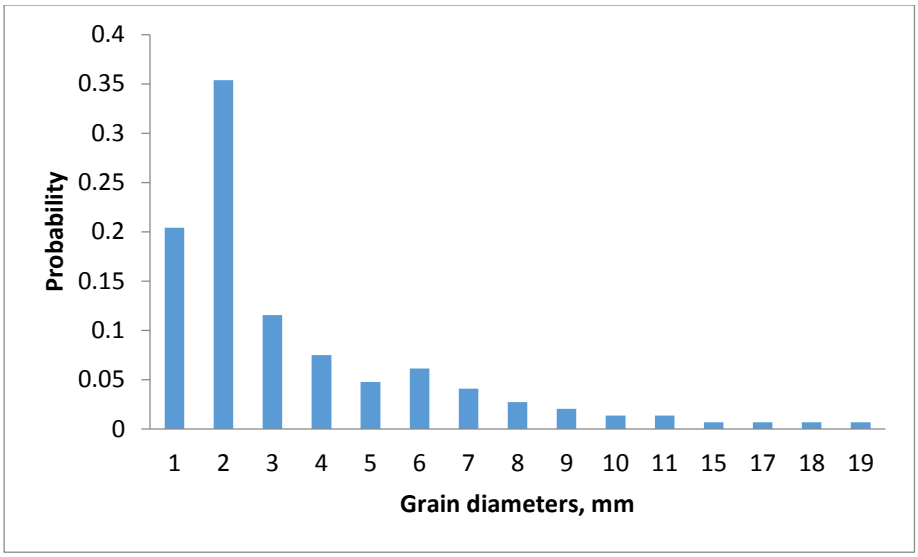

Figure 2.2. Distribution of the grain diameters of the Cardium A conglomerate.

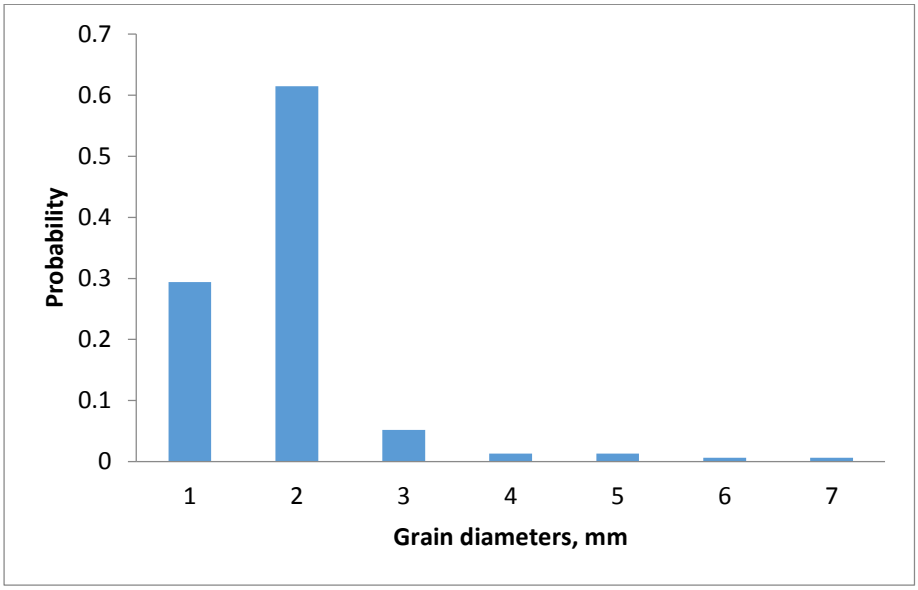

Figure 2.3. Distribution of the grain diameters of the Cardium B conglomerate.

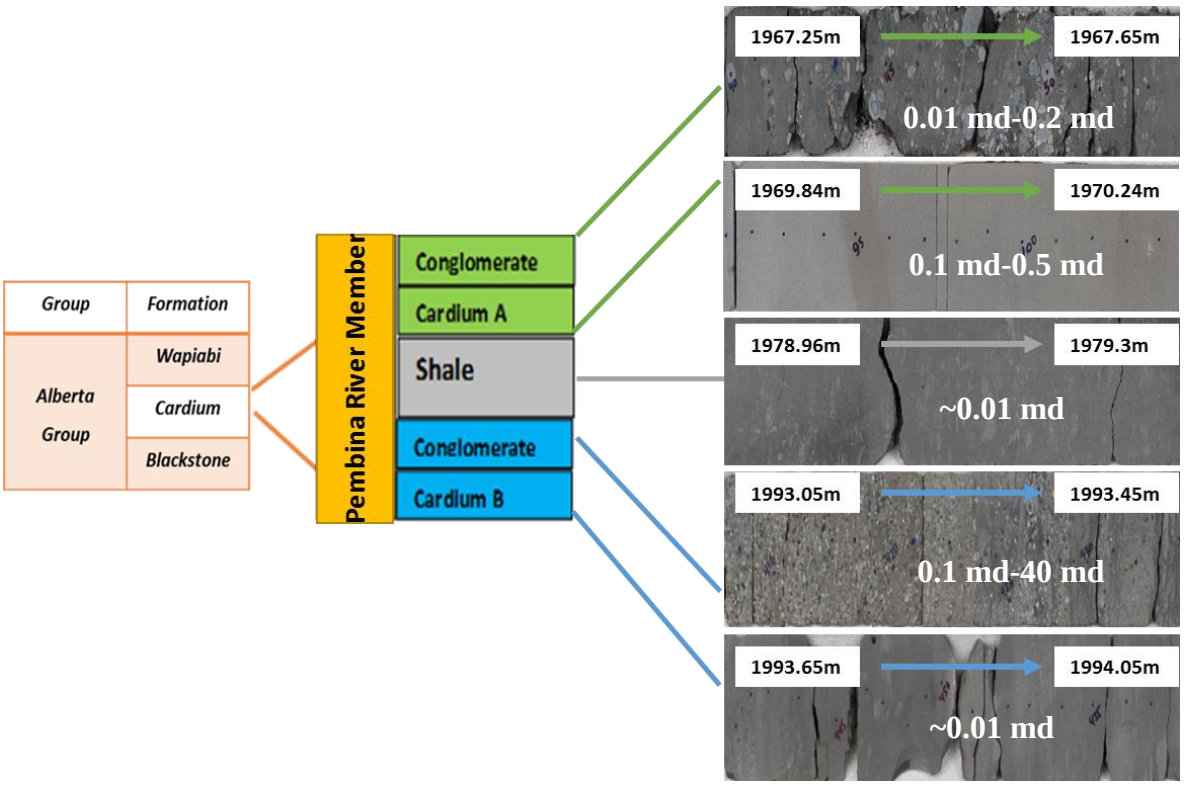

Figure 2.4. Lithofacies change in the study well (modified from Mageau et al., 2012).

2.2 Core and Well Log Depth Matching

Due to differences in drilling and logging tools and incomplete core recovery, the core and well logging depths are normally inconsistent. To assist the depth-shifting with wireline gamma ray (GR) and bulk density well logs, core gamma ray and bulk density were measured by a core laboratory after coring to assist the depth-shifting. There is a significant difference between the original core measurements and well log GR values before shifting, especially in small GR regions (Fig. 2.5). The core depth appears to be 2.5m shallower than in the logs. After adding 2.5m to the core depths, these two GR measurements match well (Fig. 2.6). However, even after this depth shift, the core and well log density measurements are not consistent in certain sections. Some locations even show opposite changes (red rectangle in Fig. 2.7). Further refinement in depth shifting is required. Because of the high heterogeneity in the tight formation, even a small mismatch will create a large difference.

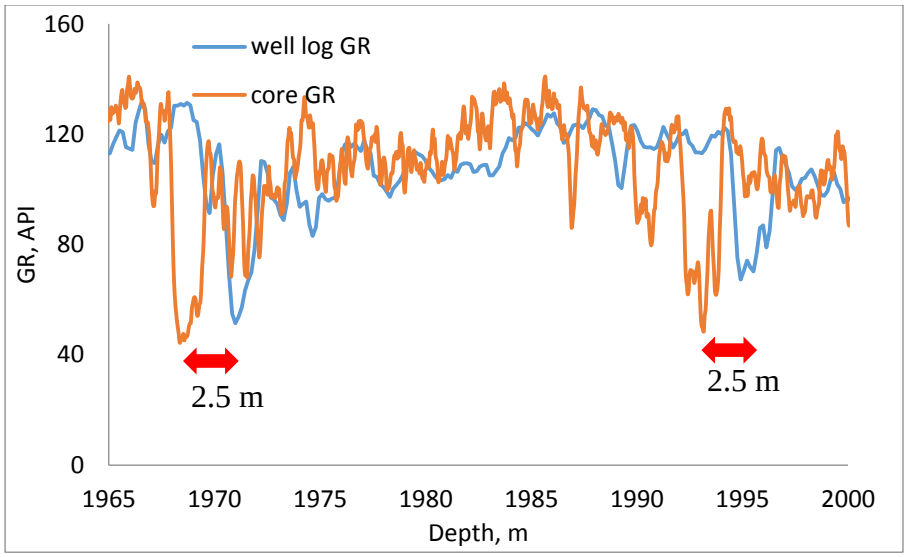

Figure 2.5. Raw core (samples every 4 to 5 cm) and well log (samples ~20 cm) GRs before depth matching in the Cardium Formation.

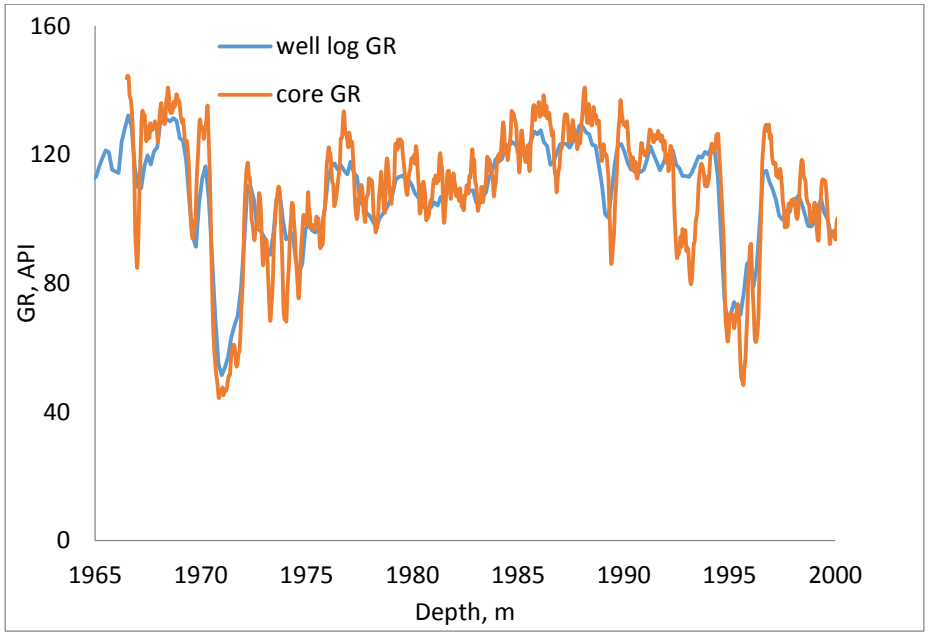

Figure 2.6. Core and well log GRs after depth matching in the Cardium Formation.

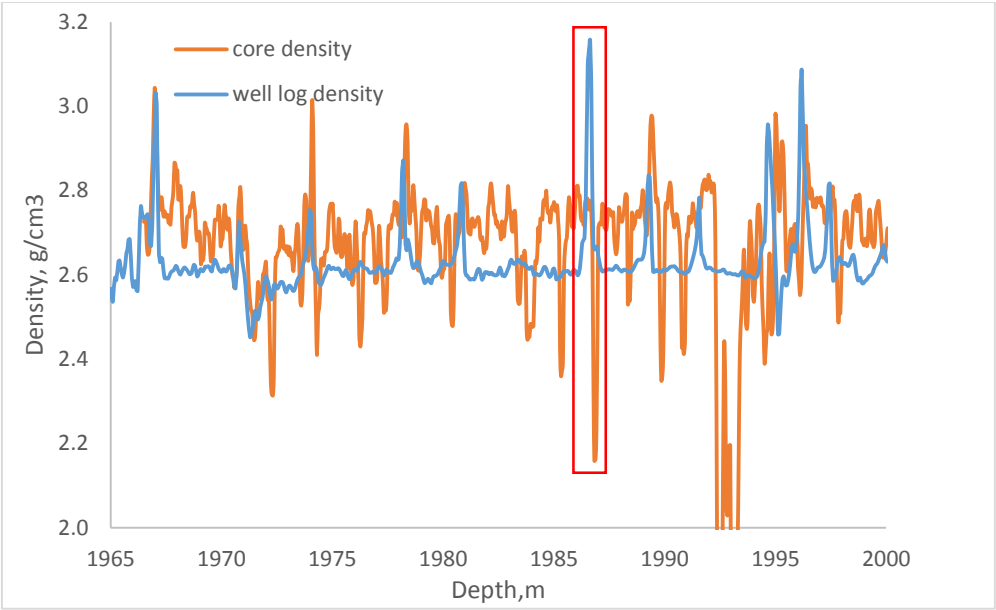

Figure 2.7. Core and well log densities after 2.5m shift in the Cardium Formation.

The comparison between core and well log GRs and densities are based on the same measurements. Relevant parameters, such as density log and core porosity, can also be used to examine the depth shift. From a core and well log GRs comparison, 2.5 m should be added to the core depth to match with the depth of the well log. After the 2.5 m shift, there is still an error comparing the density log and core porosity. The biggest core porosity should correspond to the lowest density. However, in the Cardium A, there is still an error of approximate 0.4 m between the smallest density and the highest porosity depths (Fig. 2.8). Based on this, the adjusted depth shift changed from 2.5 m to 2.1 m in the Cardium A. To evaluate these two shifts, a 0.5 m (1967.79-1968.27 m) relatively homogenous core interval is chosen, which should have similar properties (Fig. 2.9). For the GR log, there is a difference of approximately 50 API in this sample before re-shifting. It is questionable whether the GR value decreases nearly 50% in such a homogenous and small shale sample (Fig. 2.10). After re-shifting, the difference is 15 API, an acceptable change. Similarly, a density log change is observed. There is an approximate 0.06 g/cm^3 density difference in this sample using a 2.5 m shift. However, when the core depth is shifted with 2.1 m, the density log has a small difference (0.007 g/cm^3) (Fig. 2.11). Based on this specific interval, a 2.1 m shift is more suitable than the 2.5 m shift in the Cardium A.

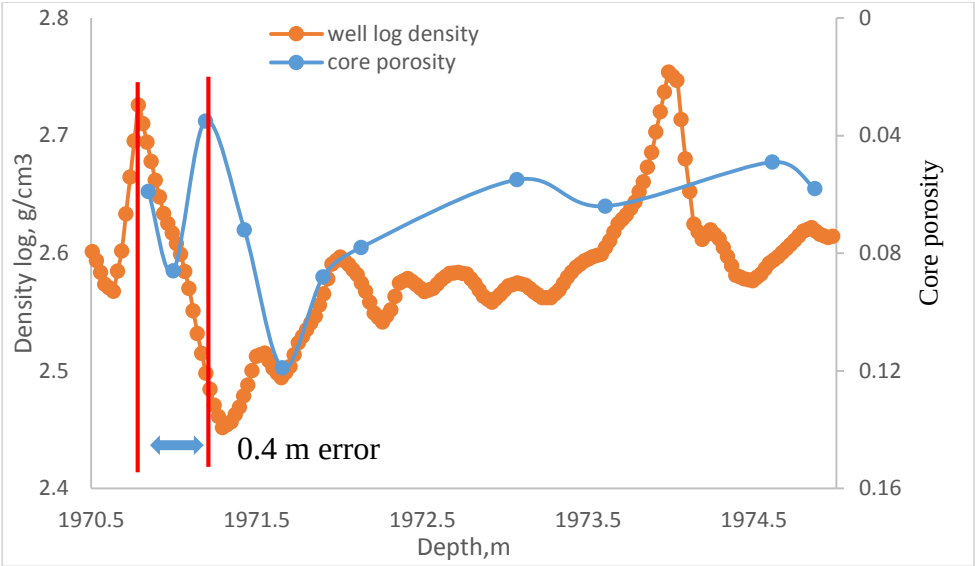

Figure 2.8. Density log versus core porosity in the Cardium A.

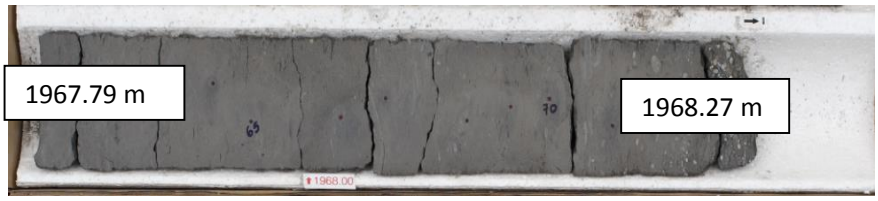

Figure 2.9. One homogenous core sample from the Cardium A.

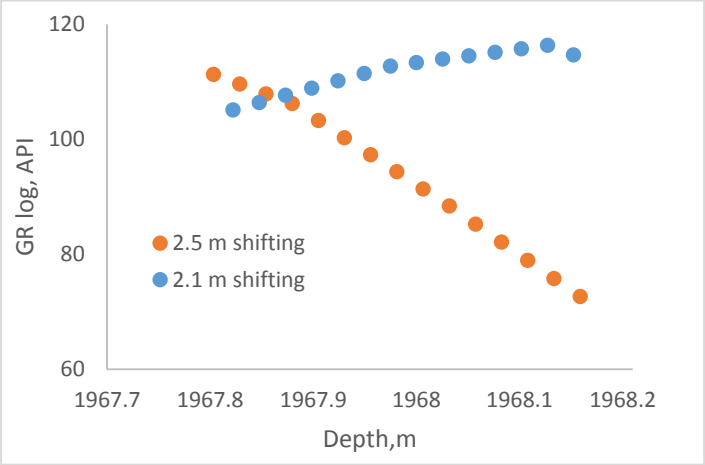

Figure 2.10. GR comparison between 2.5 m and 2.1 m shift.

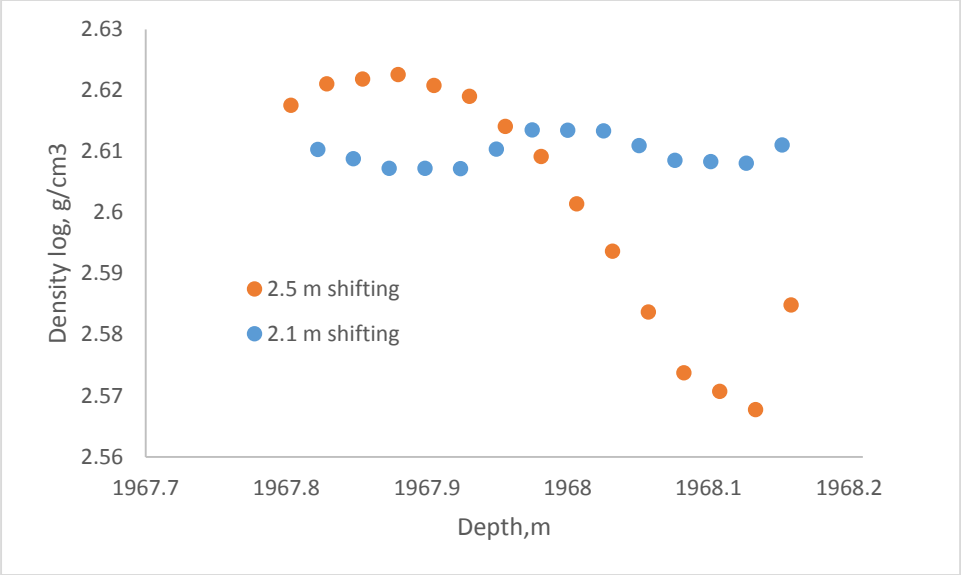

Figure 2.11. Density log comparison between 2.5 m and 2.1 m shift.

In the Cardium Formation, probe permeabilities were measured with spacing 1 to 6 cm. The probe permeability data were collected using a PDPK-400 probe permeameter. The probe tip supplies nitrogen (N_2) gas against the core slab surface and calculates the permeability according to the pressure decrease vs. time (Jones, 1994). The measurement range of this tool is between 0.001 md and 20 d (Clarkson et al, 2012). The probe permeability data used in this study are slip-corrected (Klinkenberg corrected). A total of 610 points were collected: 330 came from the Cardium A and the remainder from the Cardium B.

The probe permeability, combined with other well logs, can also be used for the depth shift testing. The nuclear magnetic resonance (NMR) T_2 value is directly proportional to the pore size (Coates, et al., 1999). Usually, the larger NMR T_2 should correspond to higher permeability. After the 2.5 m shift, the high probe k peak mismatches with the largest T_2 value, with an error of 0.4 m (Fig. 2.12). Based on all the data, the 2.1 m depth shift is more accurate in the Cardium A. In the Cardium B, the larger T_2 correlates with the higher probe k well using a 2.5 m depth shift (Fig. 2.13), so the Cardium B does not need to be re-shifted.

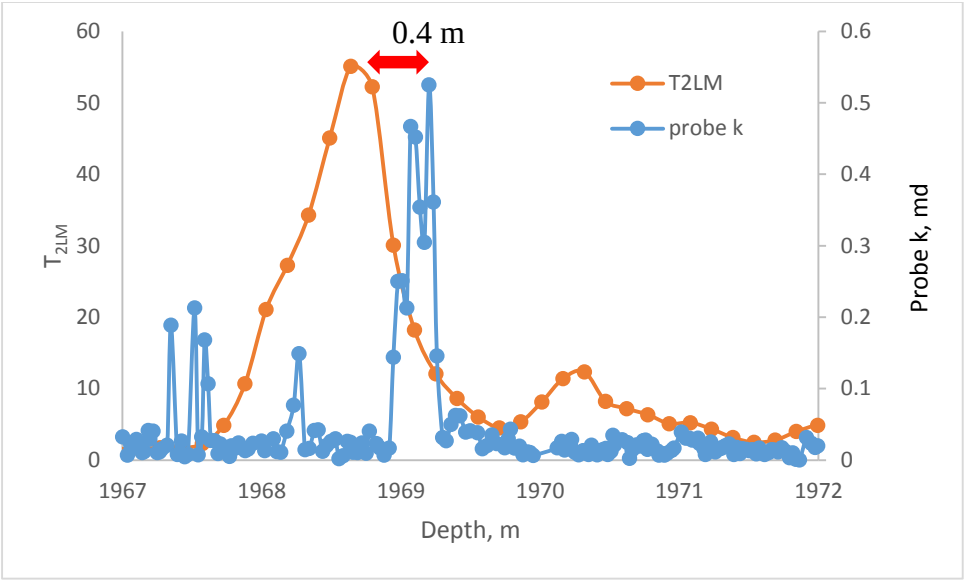

Figure 2.12. NMR T_2 versus probe k in the Cardium A.

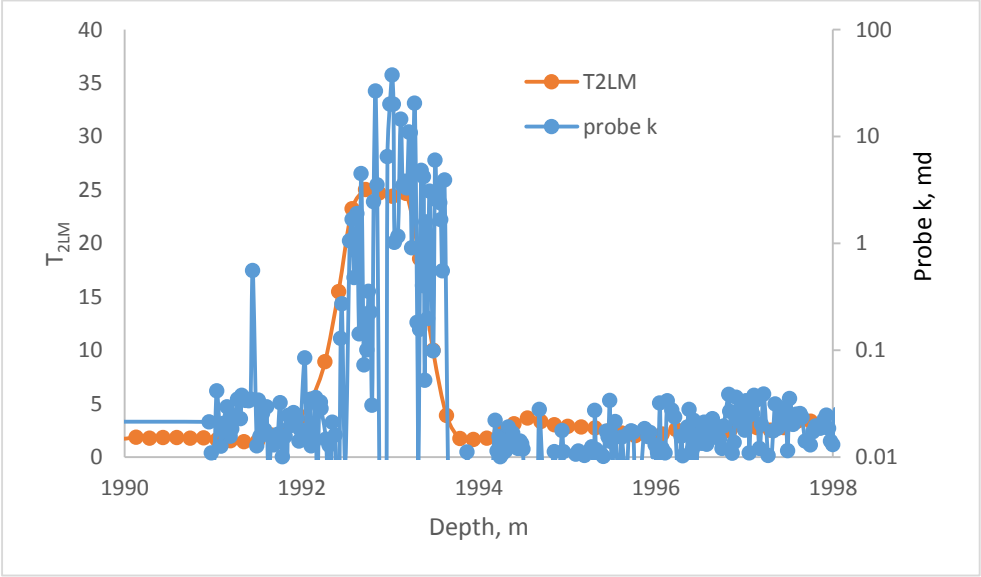

Figure 2.13. NMR T_2 versus probe k in the Cardium B.

2.3 Core Petrophysical Analysis

In addition to the probe measurements, 17 full diameter intervals were evaluated for routine core analysis from the Cardium A and Cardium B by Core Laboratories Canada. These core intervals were first put into Dean Stark distillation to measure the residual water saturations. Then the samples were cleaned using toluene extraction and prepared for the permeability to be measured in both horizontal (k_{max} and k_{90}) and vertical (k_{vert})

directions. Finally, Boyle's law technique was applied to determine the porosity using helium.

The whole core porosity shows a weak correlation with whole core permeabilities (k_{max}, k_{90} and k_{vert}) in the Cardium A (Fig. 2.14). This indicates that porosity is not the unique factor controlling the permeability in this well. k_{max} is approximately equal to k_{90} in most samples; however, there is a large difference between the horizontal and vertical permeabilities. The ratio of k_{vert} /k_{90} is commonly used to identify the anisotropy of a layered system. When the porosity is around 6 %, the anisotropy is strongest (k_{vert} /$k_{90} \approx$ 0.1) (Fig. 2.15). When the porosity is below or higher than 6 %, the anisotropy weakens. When the porosity is smaller than 6 %, the facies tends to be pure shale, which decreases the anisotropy. The vertical and horizontal permeabilities become closer, approaching isotropic and homogenous in the shale interval. On the other hand, increasing porosity with decreasing shale proportion also weakens the heterogeneity.

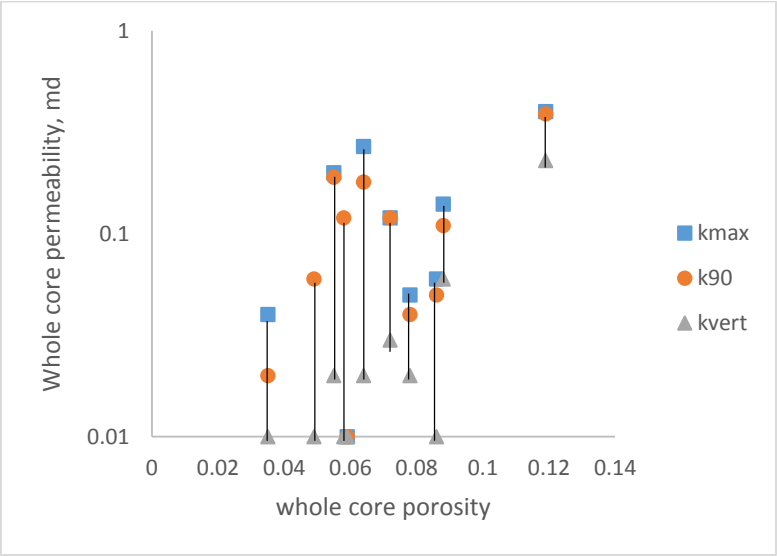

Figure 2.14. Whole core porosity versus whole core permeabilities in Cardium A. The k_{max} of one sample was not measured.

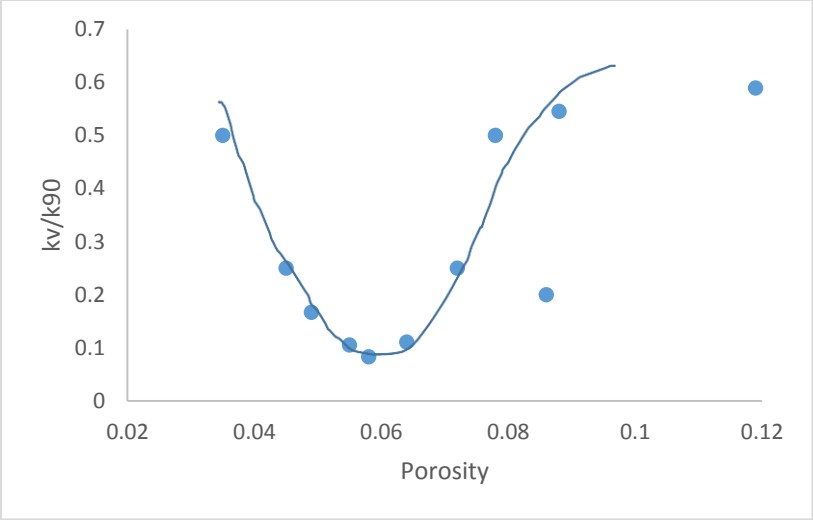

Figure 2.15. k_v/k_{90} versus porosity in the Cardium A (The line approximates the trend).

The correlation between the whole core porosity and permeability in the Cardium B is stronger than the Cardium A; A higher core porosity corresponds to a higher permeability. The trends between whole core porosity and log-permeabilities (k_{max}, k_{90}, and k_{vert}) appear approximately linear (Fig. 2.16). Similar to the Cardium A, the vertical permeability (k_{vert}) is smaller than the horizontal (k_{90} and k_{max}). The ratio k_{vert} /k_{90} shows an increasing trend with the porosity (Fig. 2.17).

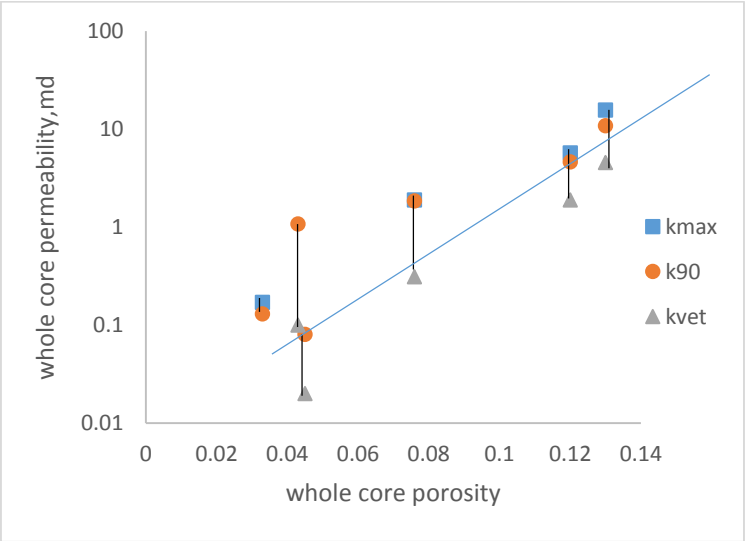

Figure 2.16. Whole core porosity versus whole core permeabilities in the Cardium B.

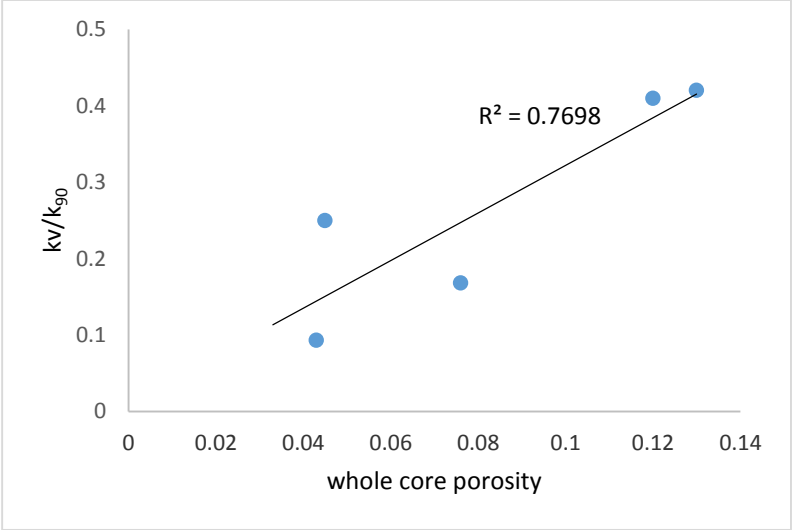

Figure 2.17. k_v/ k_{90} versus porosity in the Cardium B.

Another difference between the Cardium A and Cardium B is the correlation between core porosity and the wireline density log. In each whole core sample, the average density value was calculated. Because of the relatively constant mineralogy (shaly siltstone) in the Cardium A, the core porosity and density log correlate well (Fig. 2.18). In the Cardium B, the core porosity and density log correlate poorly because both shaly siltstone and conglomerate are present. Two relations may reflect different matrix densities (Fig. 2.19). When the porosity is 0, the density reflects the expected grain density value. From the lines (Fig.2.19), the grain densities are 2.99 and 2.81 g/cm^3 in the conglomerate and shale respectively. From the core grain density measurement, 2.99 and 2.81 g/cm^3 are a little larger than core analysis results, but still locate in the variable range (Fig.2.20). These high matrix densities indicate the existence of heavy minerals, such as siderite and pyrite. From XRD results, discussed below, their weights can reach to 5 %.

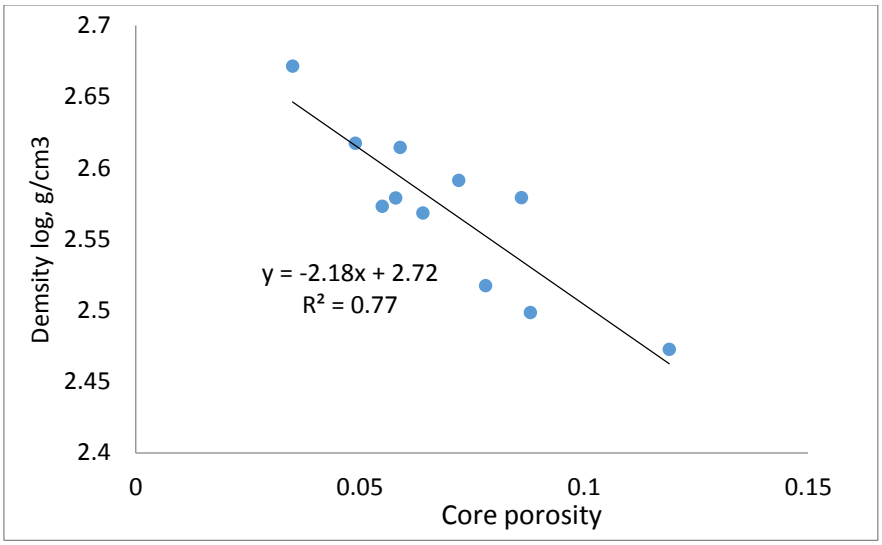

Figure 2.18. Density log versus core porosity in the Cardium A.

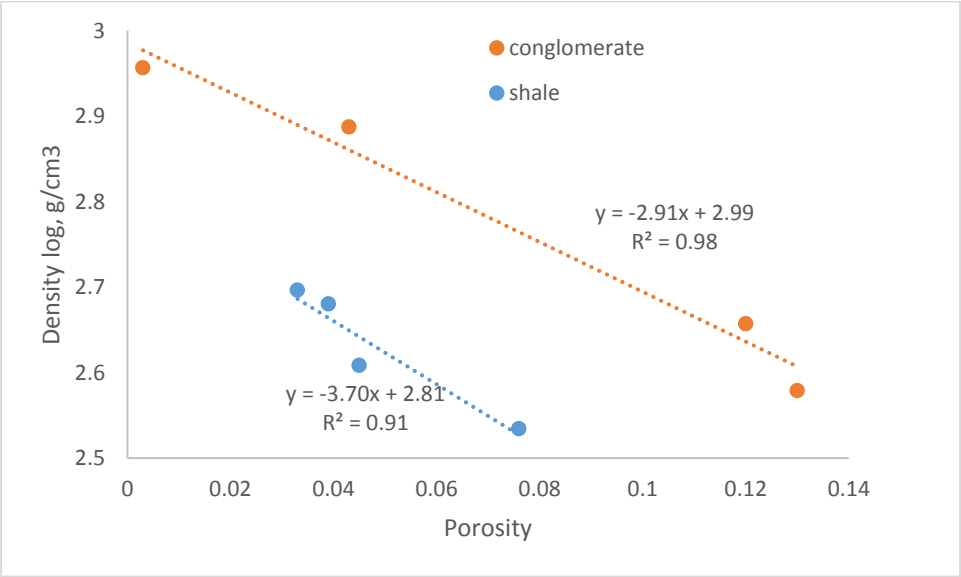

Figure 2.19. Density log versus core porosity in the Cardium B.

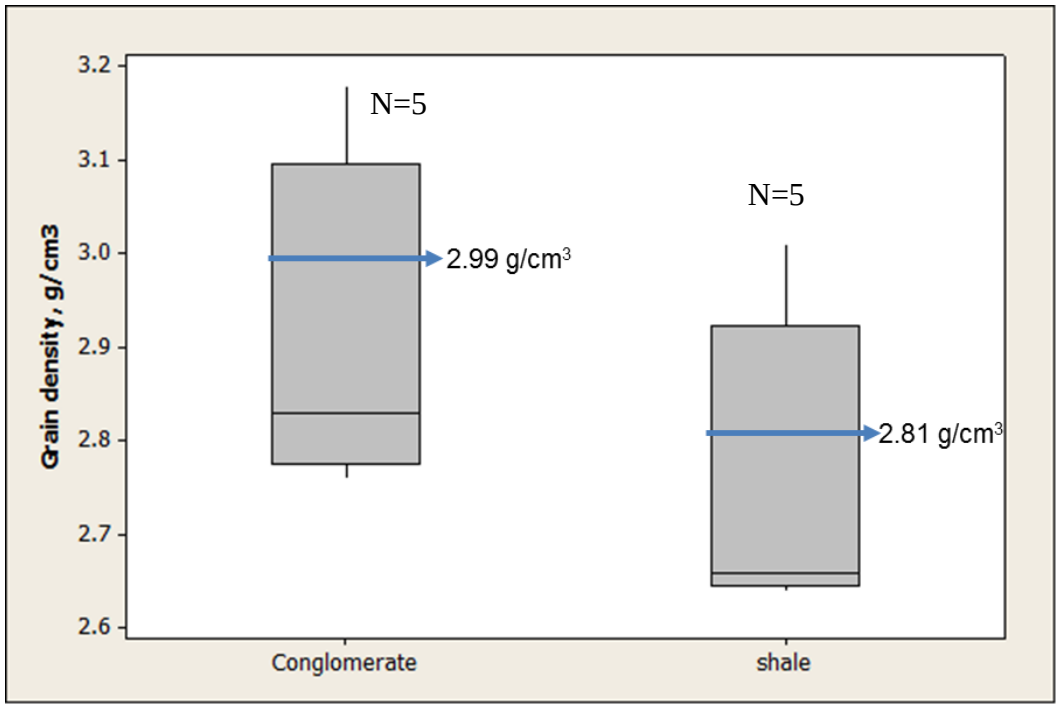

Figure 2.20. Core analyzed grain density between conglomerate and shale.

Aguilera (2002) proposed a parameter (r_{p35}) that uses permeability and porosity to estimate the pore throat aperture (Eq. 2.1). Aguilera (2014) and Clarkson et al. (2012) used r_{p35} to determine flow units in tight formations. The pore throat apertures (r_{p35}) calculated from the k_p are smaller than the k_{max} especially in the Cardium A (Fig. 2.21). The r_{p35} calculated using k_p is around 0.2 µm. However, this value increases to 0.2-1 µm when k_{max} is used. It indicates that the pore throat sizes predicted from horizontal whole core permeability (k_{max}) are larger than from probe permeability.

The conglomerate part from the Cardium B has a larger r_{p35} (>1 µm) and shows a clearly different flow unit compared with the tight Cardium A. Aguilera (2013) plotted permeability versus porosity for the Cardium tight oil reservoirs in the East Pembina area, shown in the light blue ellipse in Fig. 2.21. Only a small proportion of the Edson Field Cardium (red ellipse in Fig. 2.21) shows similar pore throat apertures (0.2 µm <r_{p35}< 1 µm). Most of our samples are located outside the blue ellipse, and have lower permeability and porosity. The tight Cardium Formations from East Pembina and Edson Field show a similar flow unit (similar r_{p35}), the latter one is even tighter.

$$r_{p35} = 2.665 \left[\frac{k}{(100\phi)}\right]^{0.45} \tag{2.1}$$

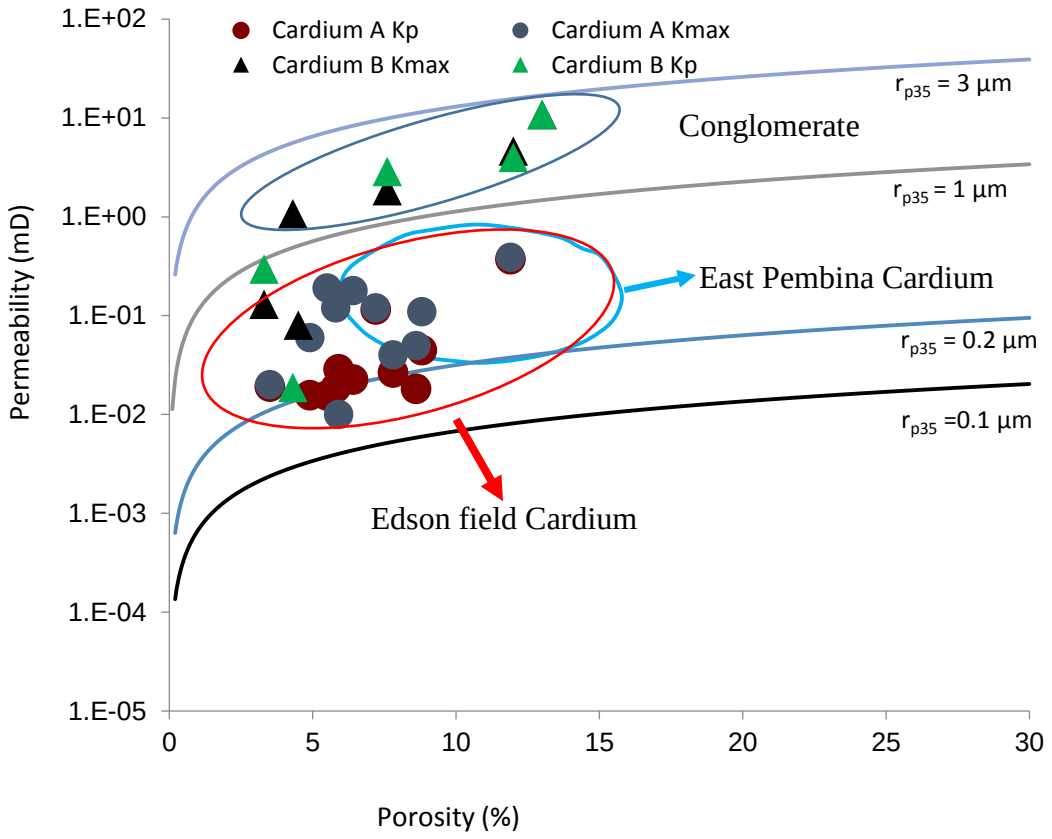

Figure 2.21. Permeability (k_p and k_{max}) vs. whole core porosity crossplot for the Cardium Formation. For the probe permeability, the arithmetic average is calculated for each whole core sample.

2.4 Mineralogical Compositions Analysis—XRD

Mineral content is another important rock characteristic that can be determined by x-ray diffraction (XRD). Five samples (three from the Cardium A and two from the Cardium B) were measured using XRD (Fig. 2.22). This provided identification of mineralogical composition, including quartz, clay, and other mineral weight fractions (main heavy minerals). All five samples have a high fraction of quartz (>75 %) and a low percentage of clay (<20 %). XRD also provided the relative percentages for the clay minerals (Fig. 2.23), which include smectite, illite, mica, kaolinite, and chlorite. The relative contents of these minerals are similar to each other in all five samples. All the smectites are observed in a mixed layer with illite. The main swelling clays come from the smectite/illite mixed-layer. The richest minerals are illite/mica, constituting around 50 %

of the clays. Due to the inherent limitations of the XRD quantification, the results should be considered semi-quantitative (Connolly, 2010).

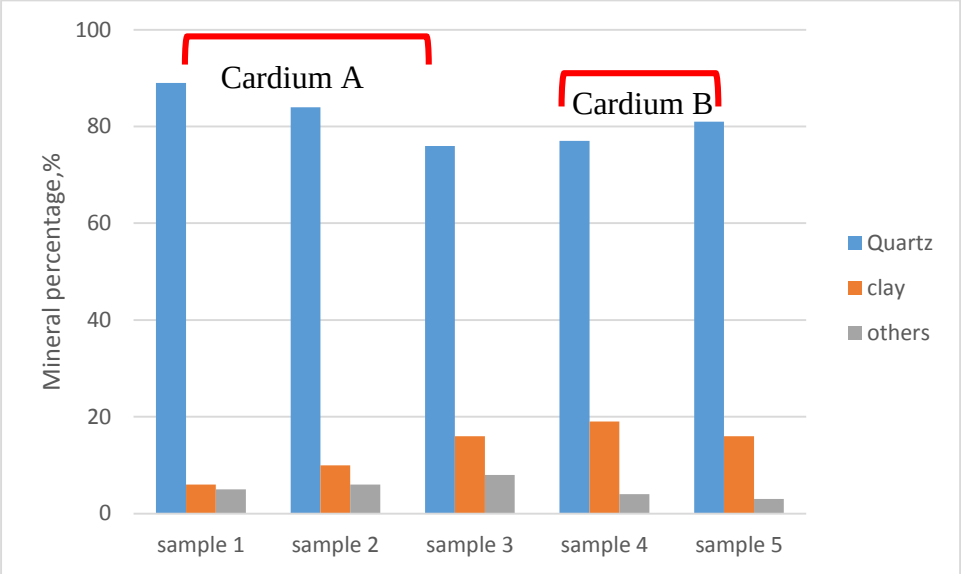

Figure 2.22. XRD mineral analysis result for Cardium A and B.

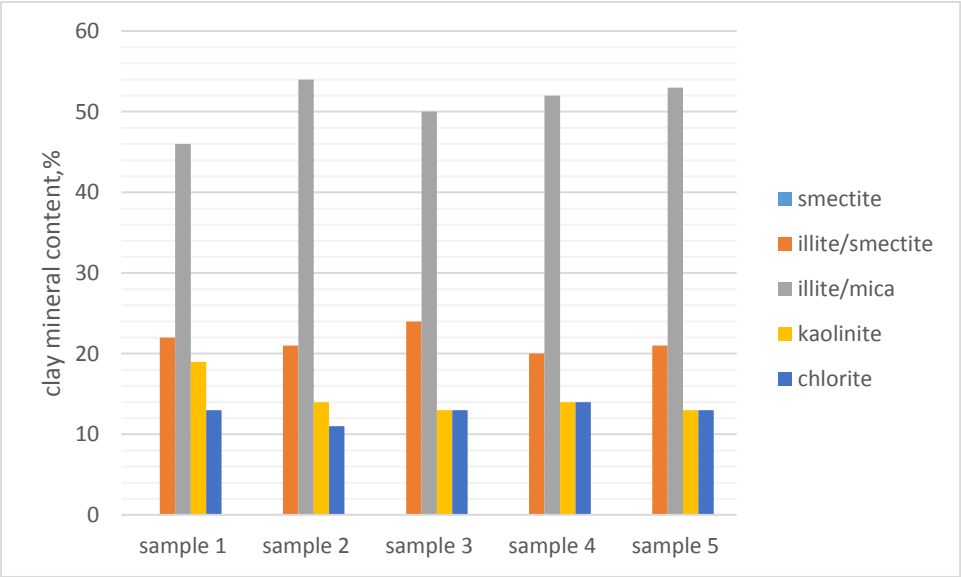

Figure 2.23. Clay mineral relative contents of the Cardium Formation.

Clay is an important factor that may affect the permeability. To compare the clay with permeability at these five XRD locations, we analyzed probe permeability (k_p) measurements. To reduce the measurement error, 11 cm × 3 cm grids are chosen at every XRD location (Fig. 2.24). The center location of the grid is chosen at the depth where clay composition is determined by XRD. The medium grid lines are located on the core

center-line. The top and bottom grids are 1 cm above and below the centre-line (Fig. 2.24). During measurements, any fracture effects are removed. At most of the locations, the k_ps did not show significant differences (Fig. 2.25).

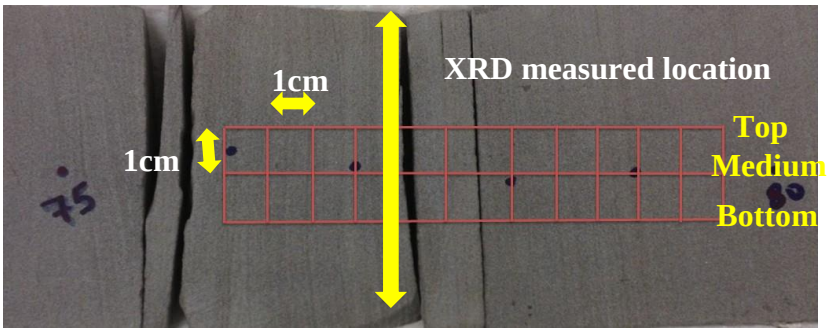

Figure 2.24. 3×11 probe permeability measurement grid.

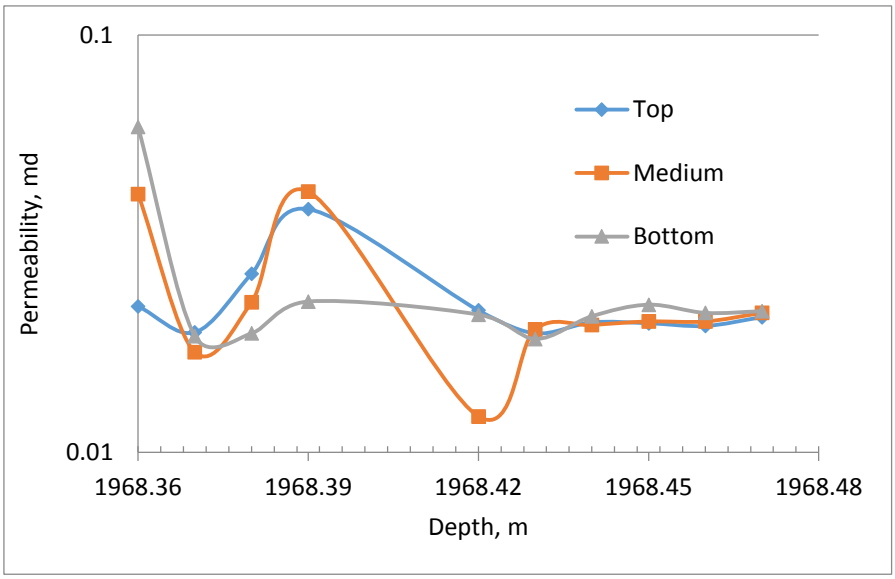

Figure 2.25. An example of the probe permeability measurements on different grids.

The GR is usually recognized as one of the most important indicators of clay, and has been called the "shale log" (Rider and Kennedy, 2011). The simple GR log shows a combination of potassium, uranium and thorium isotopes. Among the common sediments, shale shows the strongest GR response, leading to the model of larger GR values at relatively higher shale proportions. In both the Cardium A and Cardium B, shale intervals correspond with higher GR (> 100API) (Figs. 2.26 and 2.27). The quantified clay content from the XRD also shows a good correlation with the GR log (Fig. 2.28).

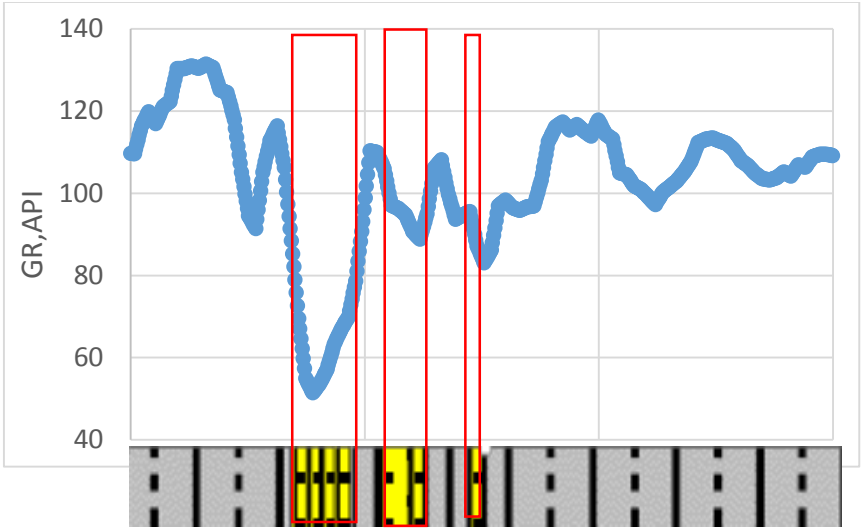

Figure 2.26. Simple GR log versus lithofacies in the Cardium A.

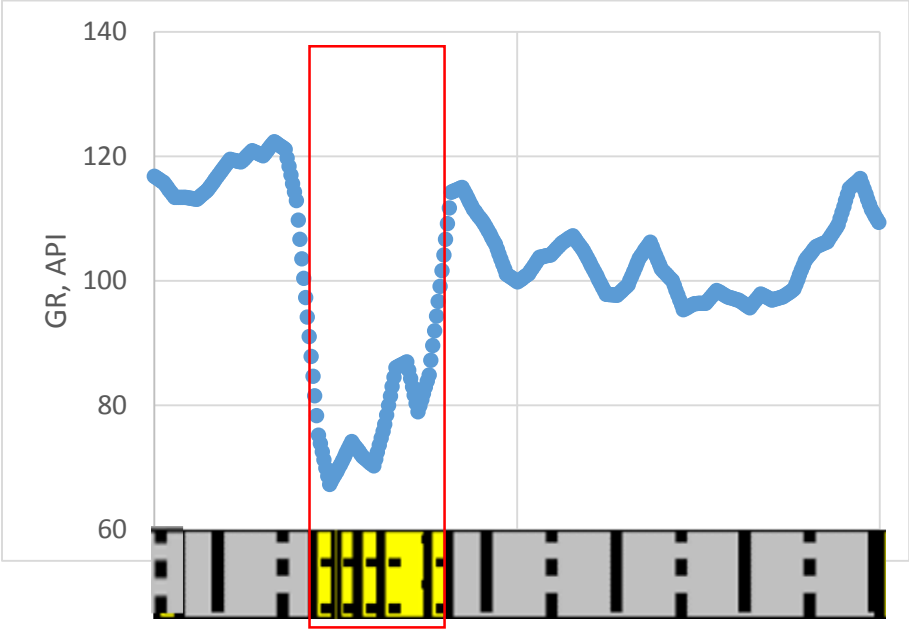

Figure 2.27. Simple GR log versus lithofacies in the Cardium B.

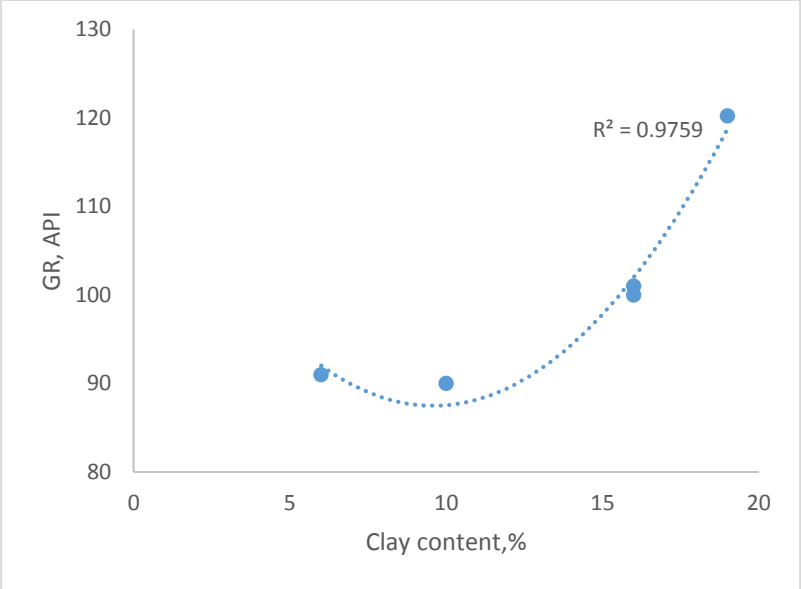

Figure 2.28. XRD clay content versus GR log.

According to the energy spectrum, potassium, uranium, and thorium radiation can be distinguished, creating the spectral GR log (SGR). Different clay minerals have their specific radioactive elements, so the SGR log can help identify the clay minerals. For example, illite contains the highest potassium amount, while chlorite has no potassium; therefore, the main contributor of potassium is the illite. The illite content from the XRD shows a strong positive linear relationship with the potassium log (Fig. 2.29).

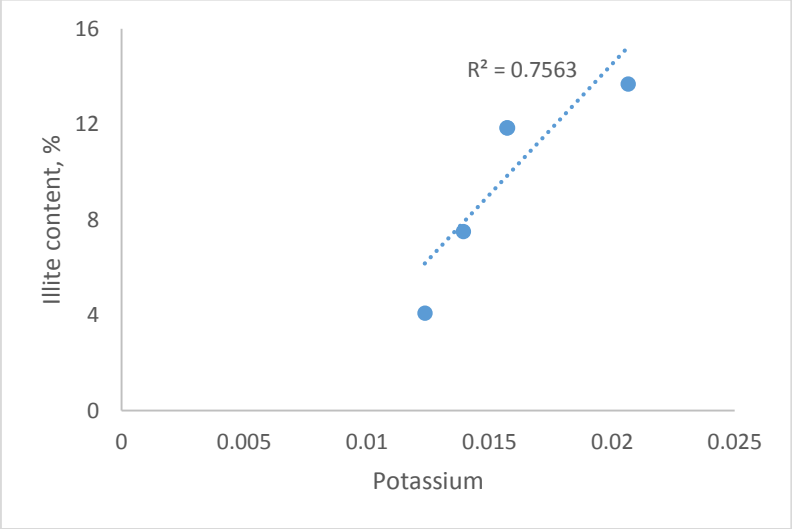

Figure 2.29. XRD illite content versus the potassium log.

From the 11 × 3 cm permeability grid in each XRD location, probe permeabilities were measured. In the Cardium A, three XRD samples are from siltstone. The permeability decreases with total clay and clay mineral (kaolinite, illite, and chlorite) contents in the silt (Fig. 2.30). In addition, the correlations between the SGR and clay minerals suggest that a basis exists for a relationship between SGR and permeability.

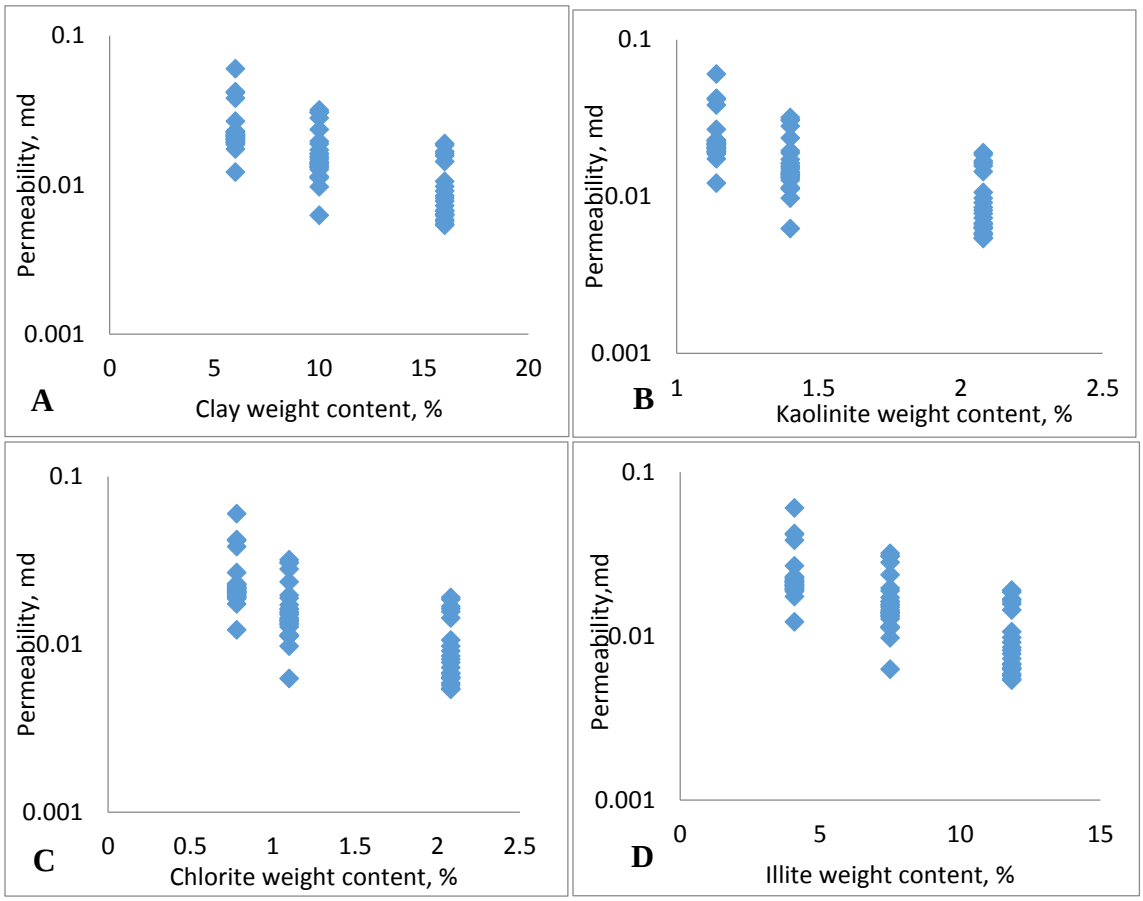

Figure 2.30. The clay and clay minerals relationships with the probe permeability of siltstones in the Cardium A (A. total clay; B. kaolinite; C. chlorite; and D. illite).

Both the GR and SGR logs show negative mild correlations with permeability (Fig. 2.31). At the intervals with small GR or SGR values, permeabilities show decreasing trends. There is a threshold effect (red lines) above which the permeabilities change little. For example, in the silt when the potassium content is smaller than 0.013, we can predict the permeability using a linear model. When the potassium content is more than 0.013, the permeability does not change much and floats around 0.01 md. It may be caused by the limitation of log resolution. We compare these four regressions before the cut off lines

(green lines in Fig. 2.31). Among these four logs, the potassium log shows the strongest sensitivity and the largest R^2 (Fig. 2.31 B), although they all have similar values of R^2.

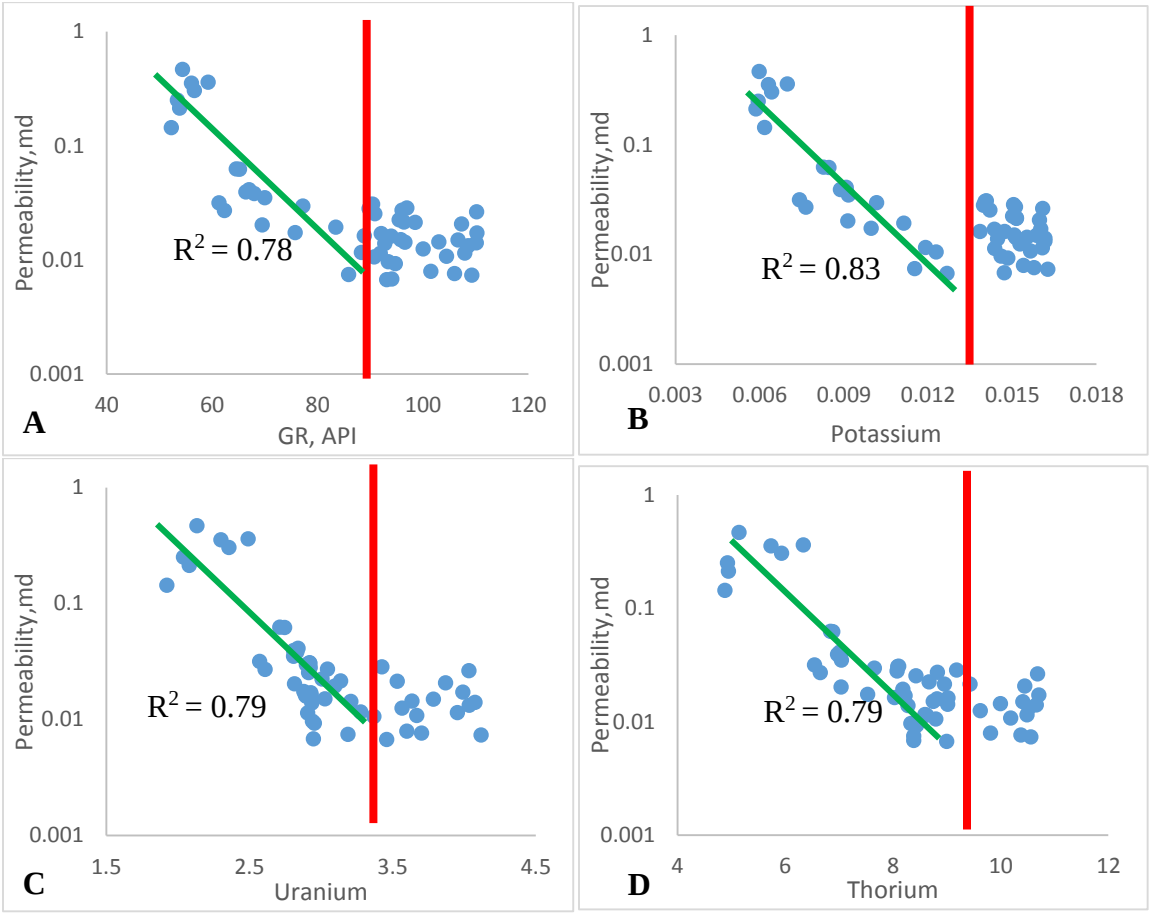

Figure 2.31. GR and SGR relationship with the siltstones permeability in the Cardium A (A. GR; B. potassium; C. uranium; D. thorium).

2.5 Conglomerate Permeability Analysis

In the Cardium Formation, the conglomerate is an important sedimentary feature. Compared to other Cardium lithofacies (siltstone/shale), the conglomerate has different depositional conditions, which creates different core textural characteristics, such as grain size, sorting, rounding. These characteristics are relatively homogenous in the siltstone and shale, which makes difficult to study their effects on the permeability. However, in the conglomerate, these properties can be quantified.

The resolution of probe measurements is around 0.6 cm, so 1 cm × 1 cm "windows" centered on the probe location is chosen from the core images (Table 2.1). In these core

image windows, the grains whose diameters are larger than 0.05 mm, are colored white and the remaining matrix is kept its original color. According to the color difference, the grain size, number, and volume proportion are counted (Table 2.1). Because the ratio of conglomerate thickness in the Cardium A to the Cardium B is 4:11, so three and seven "windows" are chosen from the Cardium A and Cardium B, respectively. In each window center, one probe permeability is measured. The Cardium B windows have more grains and smaller grain sizes than the Cardium A, which reflects different matrix supporting types. Some sorting coefficients are usually used to characterize the grain size sorting. The Trask Coefficient, which is the ratio of the 75th percentile to the 25th percentile (Selly, 2000), is calculated in both the Cardium A and Cardium B. The Cardium A conglomerate has a worse grain sorting (larger Trask coefficient) than the Cardium B, which corresponds lower permeability (Fig. 2.32).

The conglomerate matrix consists of very fine grains and has a relatively weak cementation, which contributes to the permeability. So a high conglomerate proportion usually leads to a low permeability (Fig. 2.33). It also depends on the probe location against the grain surface. If the probe is located on the grain surface or the part of the surface, it will decrease the permeability. From the window analysis, the conglomerate permeability mainly depends on grain volume proportion and grain size sorting. A lower grain volume proportion and better grain size sorting lead to higher permeability.

Actually, the core image analysis based on 1 cm × 1 cm window cannot cover all information. The image analysis result (Table 2.1) is based on the core sample surface condition. However, according to Meyer and Krause's (2001) probe flow model (Fig. 2.34), the probe permeability is affected by complex flow geometry. It is a simplification to use the surface to represent the whole flow region. However, different sections of one core sample with limited size do not show significant geological differences. Therefore, the analysis based one core surface is representative of the 3D flow complexity.

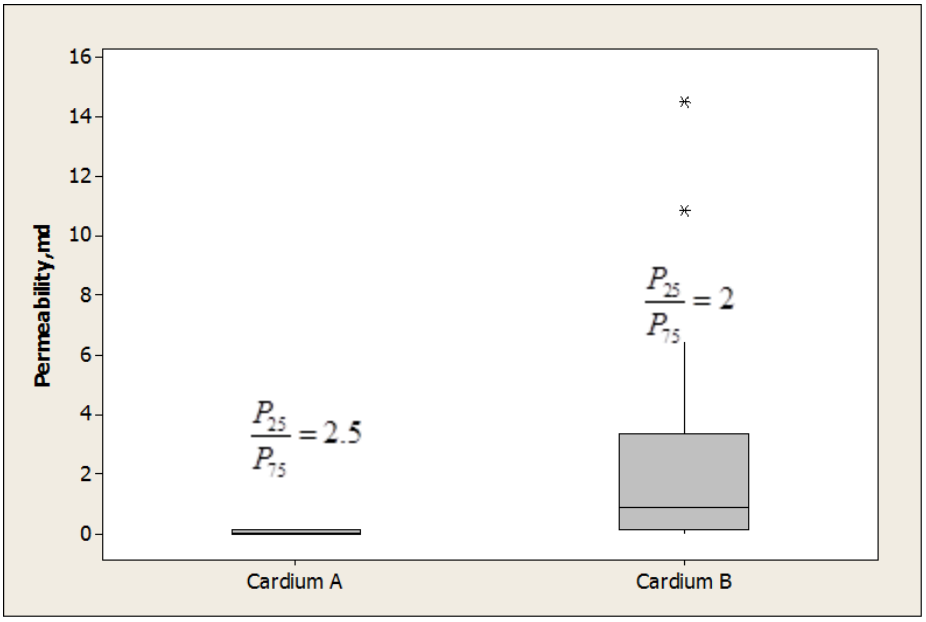

Figure 2.32. Box and Whisker plots of conglomerate permeability from the Cardium A and Cardium B, along with their Trask grain size coefficients.

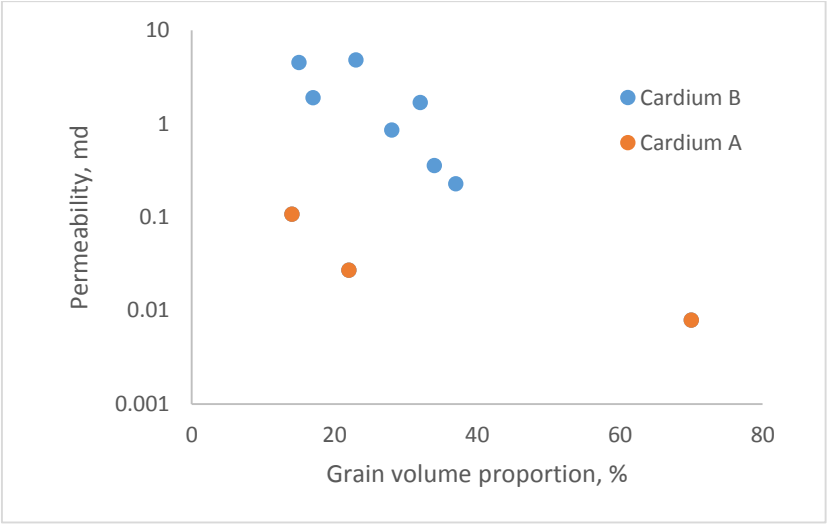

Figure 2.33. Grain volume proportion versus permeability in the conglomerate.

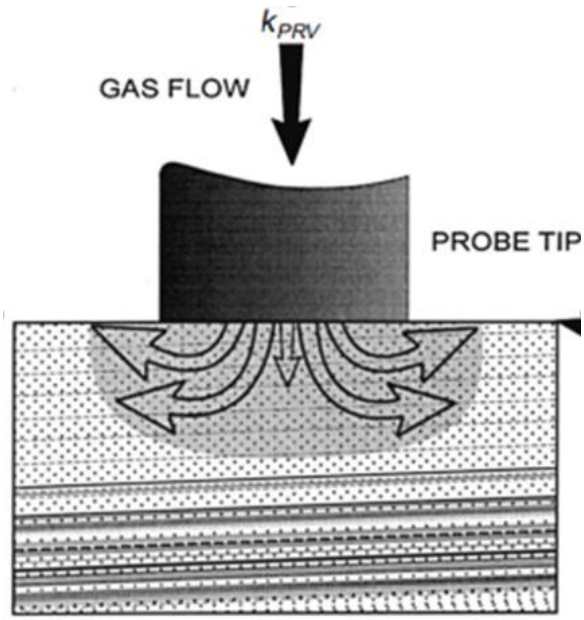

Figure 2.34. Schematic of preferential probe flow path to the sample surface (from Meyer and Krause, 2001)

Table 2.1. Grain parameter in the conglomerate (red color from the Cardium A; green color from the Cardium B)

"windows"	grain volume ratio(%)	biggest size(cm)	smallest size(cm)	grain number	probe Perm, md
	14	0.3	0.025	17	0.11
	70	0.92	0.033	5	0.0079
	22	0.42	0.017	11	0.027
	32	0.28	0.06	32	1.68
	28	0.21	0.057	24	0.48
	17	0.14	0.057	27	1.90
	15	0.28	0.057	30	4.51
	34	0.214	0.085	30	0.36
	37	0.357	0.07	40	0.23
	23	0.428	0.057	13	4.81

CHAPTER 3: PERMEABILITY CHARACTERIZATION AND PREDICTION USING CONVENTIONAL LOGS

3.1 Permeability Distribution and Variability

The properties of permeability, as one of the most important reservoir parameters, are continuously attracting attention. The basic statistical character of permeability, its distribution, is still being discussed. Law (1944) studied three samples from different depths and found that the log (k) followed the normal distribution in all three cases. Collins and Jordan (1961) described permeability statistical characteristics. They thought that one unique distribution of permeability existed in the ideal reservoir and that the permeability is randomly distributed in the actual reservoir. The porosity was recognized as a factor that controls the permeability distribution. They showed that samples have one permeability distribution with the same porosity.

In the Cardium Formation, the permeability shows very complex PDFs. According to probability plots for both the Cardium A and Cardium B, the permeability distribution cannot be described as either normal or log-normal (Figs. 3.1 and 3.2, respectively).

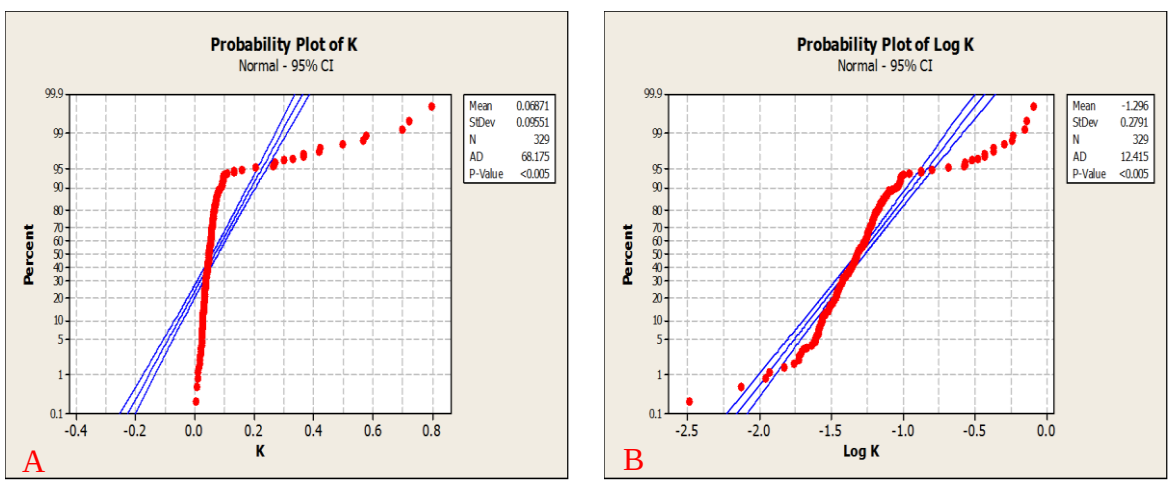

Figure 3.1. A) Probability plot of k in the Cardium A; B) Probability plot of log(k) in the Cardium A.

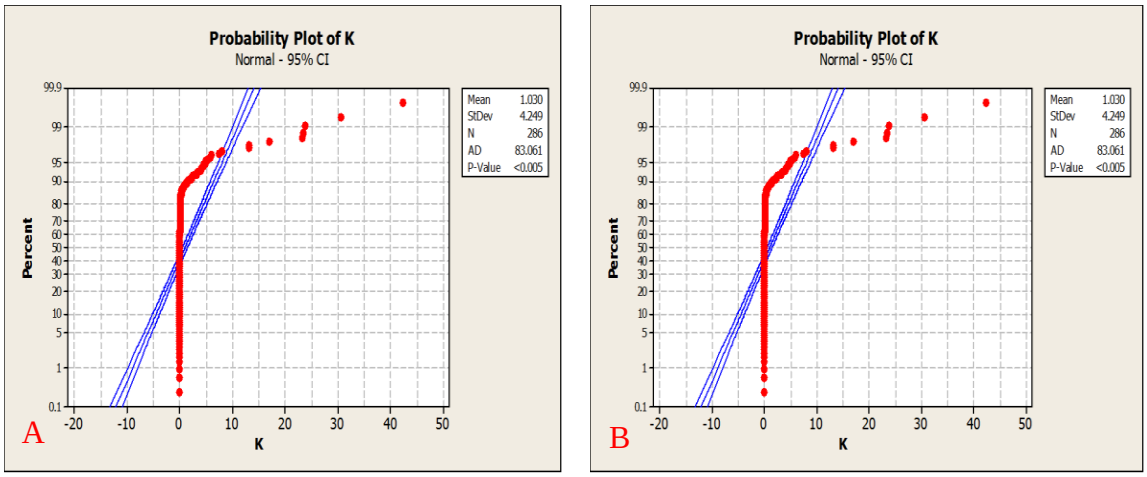

Figure 3.2. A) Probability plot of k in the Cardium B; B) Probability plot of Log(k) in the Cardium B.

Complicated facies may be the cause of the complex permeability distributions in the Cardium Formation. For example, the Cardium A can be divided into five intervals based on the lithofacies differences (Fig. 3.3). Intervals 1 and 5 mainly contain pure shale and shaly siltstone. Interval 2 is the conglomerate and interval 3 has a combination of conglomerate and pure shale. Relatively clean siltstone deposits are in interval 4. The probability plots of the log (k) from different intervals indicate a log-normal distribution (LND) in shale and shaly siltstone zones from intervals 1 and 5 (Fig. 3.4 A). Similar results are observed in other intervals, where the LND fits the unique facies permeability (Fig. 3.4). The same process can be applied in the Cardium B. Compared with the Cardium A, the facies in the Cardium B are relatively simple, containing pure shale and conglomerate. In the unique facies, like conglomerate, the probability plot of log (k) also shows an LND (Fig. 3.5). The collection of permeabilities in the Cardium Formation does not appear to have a unique distribution, but each facies permeability appears to be LND.

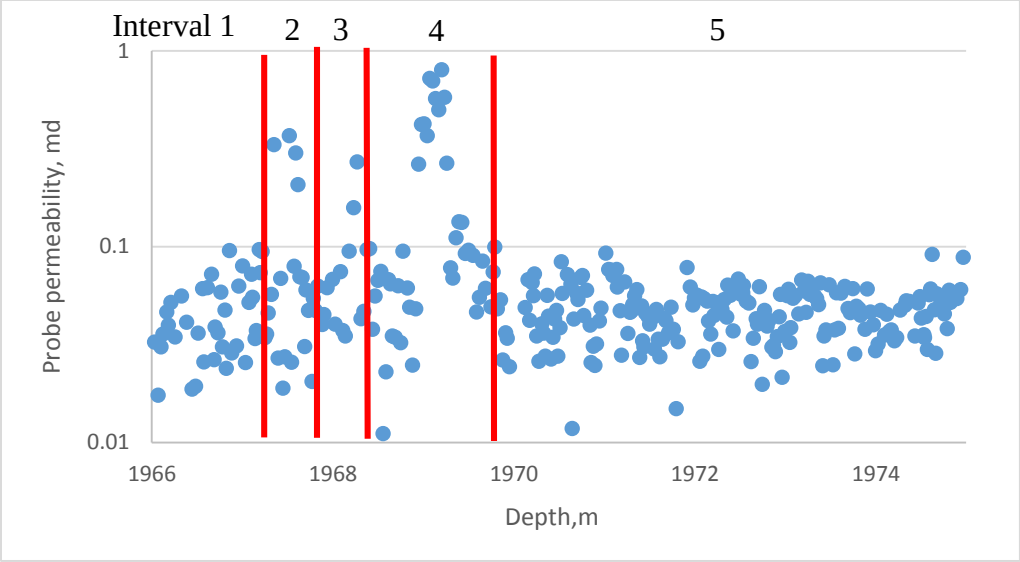

Figure 3.3. Permeability of the Cardium A and its five intervals.

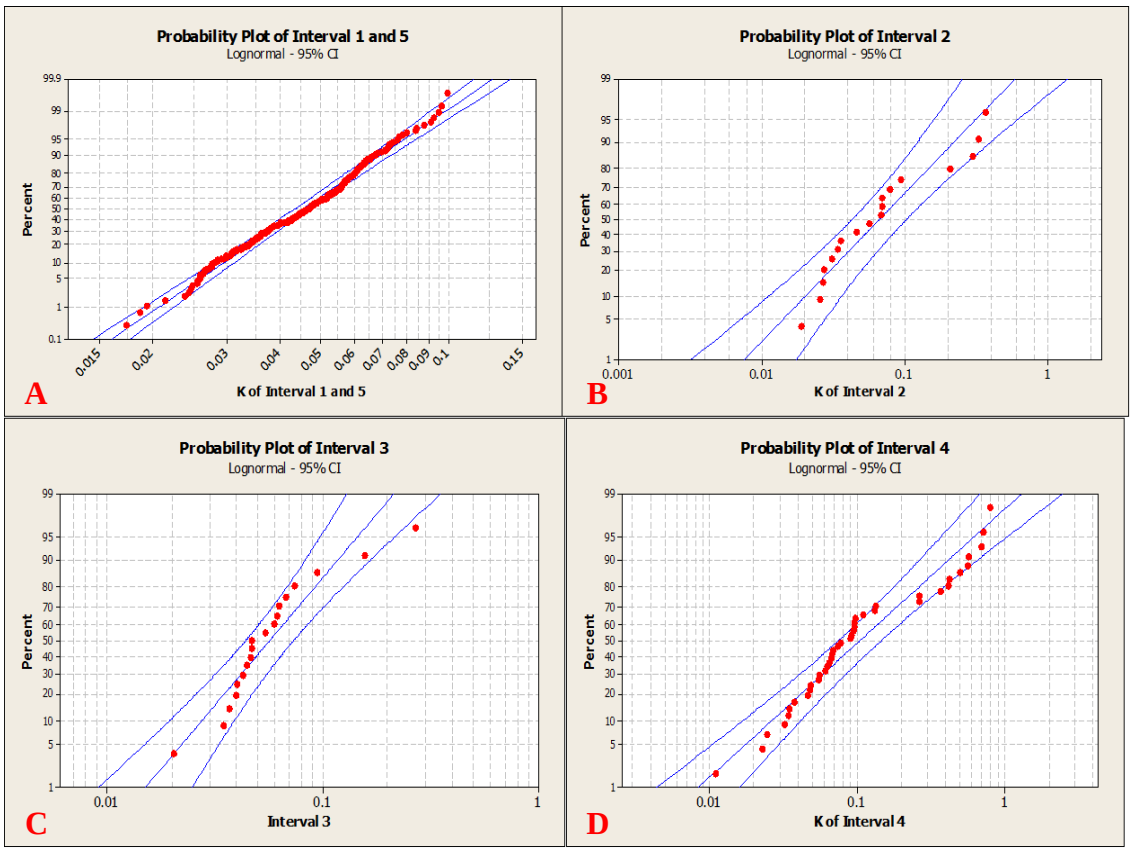

Figure 3.4. A) Log (k) probability plot of interval 1 and 5; B) Log (k) probability plot of interval 3; C) Log (k) probability plot of interval 3; D) Log (k) probability plot of interval 4.

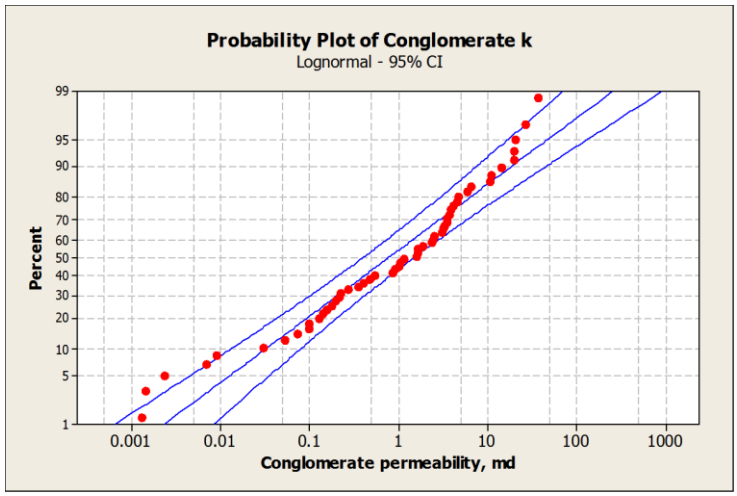

Figure 3.5. Log (k) probability plot of the conglomerate in the Cardium B.

The permeabilities used in the preceding distribution analysis are from probe measurments. Because of the small scale of the probe, a sufficient number of measurments are required to characterize the formation comprehensively. Corbett and Jensen (1993) recommended a simple rule to calculate the required sample number (Eq. 3.1). This equation is based on a 20 % error margin. In the Cardium A, the actual sample number (N_{actual}) is larger than the smallest requirement (N_{recc}) (Table 3.1), indicating our samples are sufficient to cover all the formation information. In fact, using the rule from Eq. 3.1, many measurements are unnecessary. The opposite case happens in the Cardium B, where N_{actual} is less that N_{recc}, meaning that the measurements in the Cardium B are insufficient to estimate the mean permeability at the 20 % tolerance level. There are, however, sufficient measurements to estimate the mean with a 45 % tolerance. The implications of this are that the probe permeabilities will provide reliable measurements for the Cardium A, but do not cover all the information for the Cardium B.

Corbett and Jensen (1993) divided the permeability heterogeneity into three categories according to the coefficient of variation (C_v). When $C_v > 1$, the formation belongs to the very heterogeneous category. A heterogeneous formation has a C_v between 0.5 and 1. When the $C_v < 0.5$, the formation is considered homogenous. When we use the probe permeabilities, both the permeability of the Cardium A and Cardium B present high heterogeneities, with $C_v > 1$ (Table 3.1). The heterogeneity of the permeability in the Cardium B is larger than in the Cardium A. The C_v based on the probe permeability is between the entire core horizontal permeability (k_{90}) and the entire core vertical

permeability (k_{vert}) in the Cardium A (Table 3.1). Due to the limited number and unique sample facies in the Cardium B, the whole core permeability calculated C_v is not representative.

$$N_{recc} = (10C_v)^2 \tag{3.1}$$

where $C_v = \frac{Standard\ deviation}{Arithmetic\ average}$

Table 3.1. Permeability variability parameters.

	Cardium A			Cardium B		
Parameters	C_v	N_{recc}	N_{actual}	C_v	N_{recc}	N_{actual}
Probe k	1.4	300	330	4	1600	305
Whole core k_{90}	0.93	86	11	1.34	178	6
Whole core k_{vert}	1.66	276	11	1.40	197	5

3.2 Experimental Design

Permeability directly measured from the core provides the most accurate estimate, but it is the most costly. Indirect permeability predictors are always being considered, among which well logs are the most attractive. The costs from core analyses were nearly 10 times greater than from the well logs (Yao and Holditch, 1993). In the Cardium A, we put conventional well logs and core permeability measurements together (Fig. 3.6). Two typical zones show particularity special properties. In Zone 1, the permeability is relatively high and the well logs show particular values. For example, GR and SGR (tracks 2 and 5) are the lowest and resistivity logs are the largest (track 4). However, in Zone 2, the horizontal permeability is high, but not all well logs show consistent responses. In the Cardium B (Fig. 3.7), the high permeability zone shows a similar trend to Zone 1 in the Cardium A. Except for these high permeability zones, it is very difficult to identify relationships visually between permeability and the well logs, especially in the shale part.

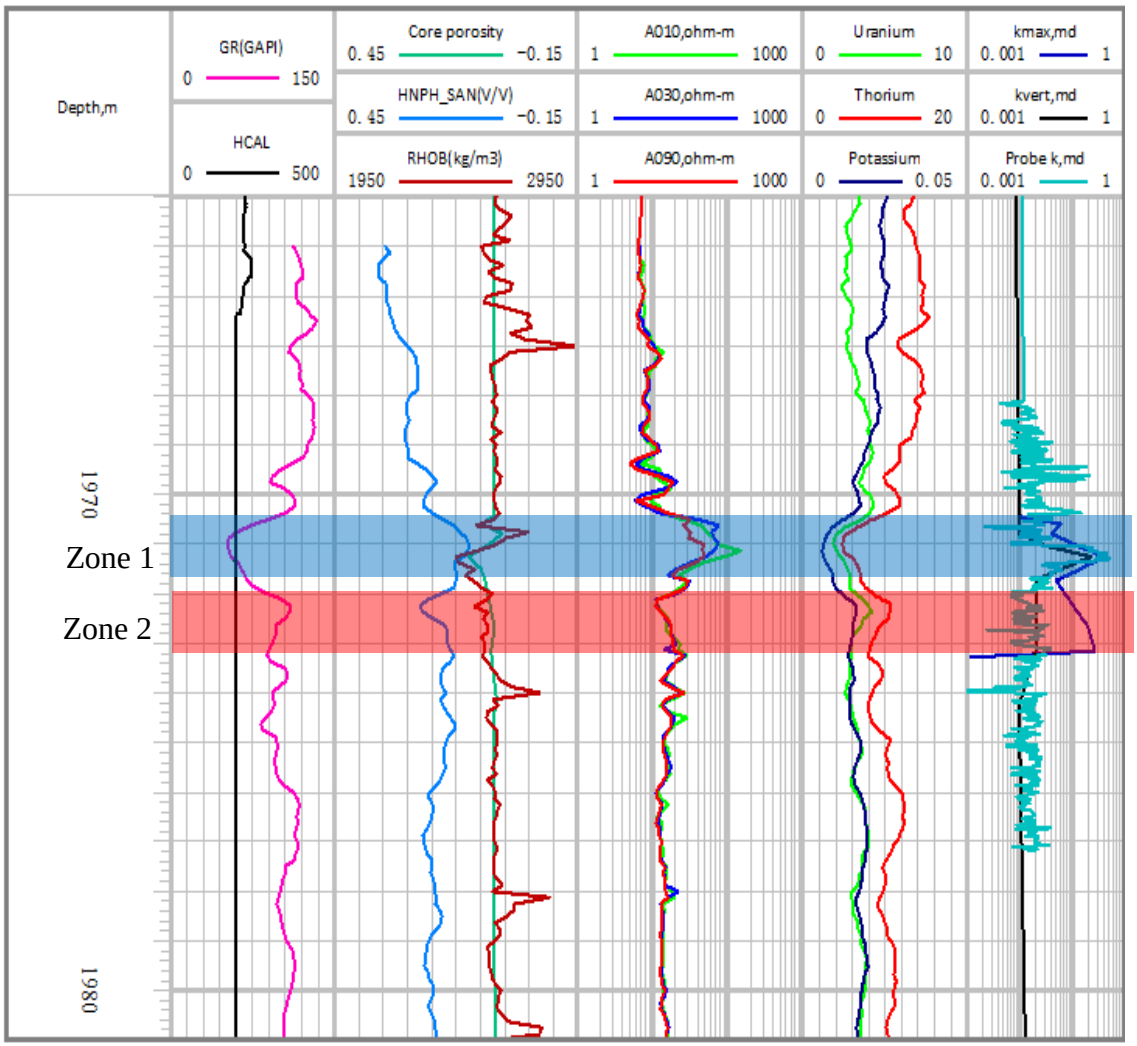

Figure 3.6. Typical well logs and core porosity and permeability in the Cardium A. Track 1: depth. Track 2: GR and caliper logs. Track 3: Density, neutron, and core porosity. Track 4: Array induction resistivity logs. Track 5: SGR logs. Track 6: Probe, horizontal and vertical whole core permeabilities.

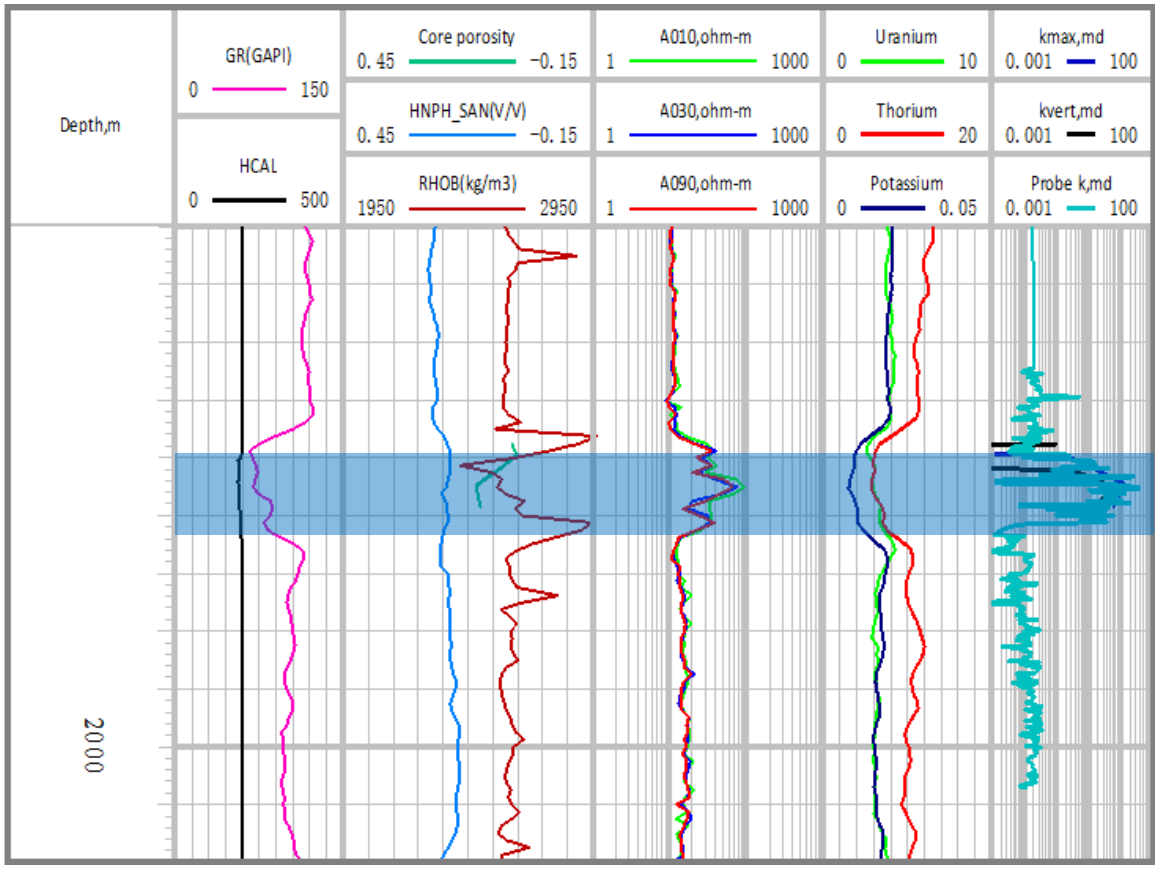

Figure 3.7. Typical well logs and core porosity and permeability in the Cardium B. Track 1: depth. Track 2: GR and caliper logs. Track 3: Density, neutron, and core porosity. Track 4: Array induction resistivity logs. Track 5: SGR logs. Track 6: Probe, horizontal and vertical whole core permeabilities.

We need a more systematic and data-based method to select potentially significant well logs and identify their relationships with the permeability. If we assume that well logs are various factors (explanatory variables) and the permeability is the corresponding response, experimental design can help to select potential impact factors (well logs) from complicated relationships with the least effort. Nine well logs have been taken as impact factors: array induction resistivities (A010 and A090), density porosity (DPH), gamma ray (GR), spectral gamma ray (potassium-HFK, thorium-HTHO, and uranium-HURA), photoelectric factor (PEF), and density (RHO). Relationships between the permeability and logs are complex in both the Cardium A and Cardium B. In the Cardium A, the deep resistivity (A090) seems to relate to the permeability as a single factor (Fig. 3.8). For the two-factor combination effect, deep resistivity (A090) and GR are the most significant. In

the Cardium B, the relationships are more complicated than in the Cardium A. No single factor shows a more prominent effect than others do (Fig. 3.9). The combined potassium and thorium, GR and PEF logs show more important influence on permeability than other logs do. We then will further analyze these significant single and double factors.

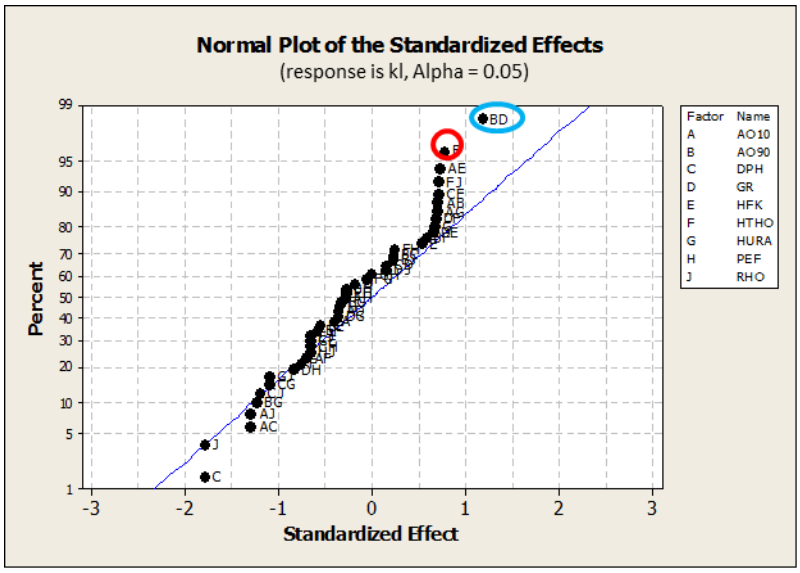

Figure 3.8. Plot of different well log effects in the Cardium A (significant factors are shown in circles).

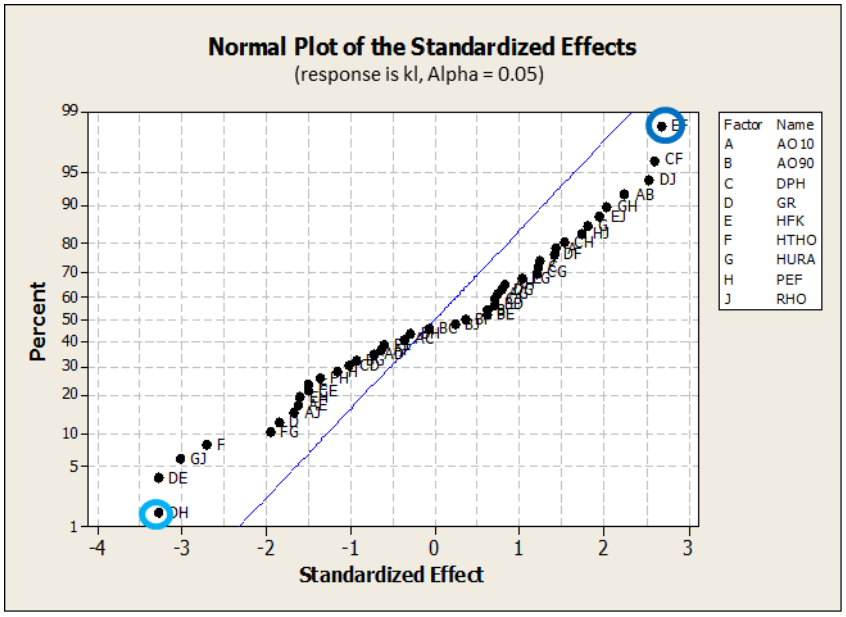

Figure 3.9. Plot of different well log effects in the Cardium B (significant factors are shown in circles).

3.2.1 Single Factor

From the experimental design analysis, the deep resistivity (A090) seems to affect the permeability significantly as a single factor. It is difficult to see an evident linear or other relationship between the deep resistivity and permeability (Fig. 3.10). There are two separate clusters of low and high permeability. In the low permeability cluster (<0.1 md), the permeability appears to be distributed randomly with the deep resistivity. In the high permeability cluster (>0.1 md), the permeability increases with an increase in the deep resistivity. In the shale and highly shaly siltstone intervals (low permeability zone), the shale has a more important effect on resistivity than the formation fluid does. The permeability and resistivity are usually low in the shale, causing the low permeability to correspond to low resistivity. However, the resistivity is more sensitive to the shale compared with the permeability. For example, in two shale intervals (A and B in the Fig.3.11), the permeability shows a similar character (Fig. 3.11 left Box and Whisker plot); but the resistivity presents a significant difference between each interval (Fig. 3.11 right Box and Whisker plot). This suggests why, in the shale zone, the resistivity is more variable than the permeability.

Although there is no a clear trend between the permeability and resistivity, there are still some clues about their relationship. All the high permeabilities come from high resistivities. So regarding the resistivity as the condition, the log (k) cumulative distribution function (CDF) is calculated. When the resistivity is lower than 30 ohm-m, all the permeabilities are smaller than 0.1 md. There are about 60 % high permeability (>0.1 md) when the resistivity is higher than 30 ohm-m (Fig. 3.12). In other words, if we want to look for the high permeability intervals, then high resistivity (>30 ohm-m) is a prerequisite. We need to find the best cutoff value to make our estimate with minimum error. For example, if we set 33 ohm-m as the cutoff value, this is 31% and 0% errors from the high permeability and low permeability part, respectively, giving a total error of 31%. According to the calculation, when 40 ohm-m is chosen as the cutoff, the total error is at a minimum (Fig. 3.13).

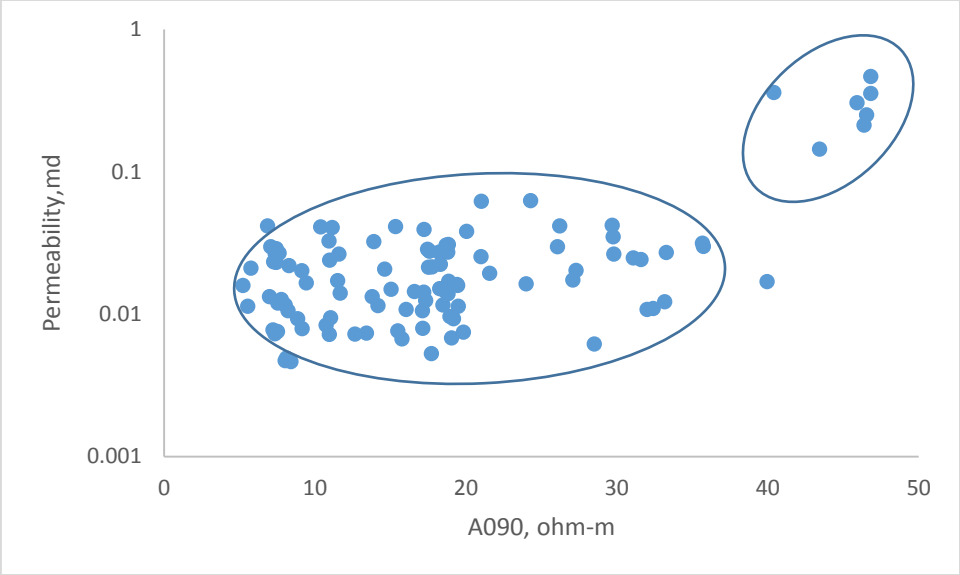

Figure 3.10. Deep resistivity (A090) versus permeability in the Cardium A.

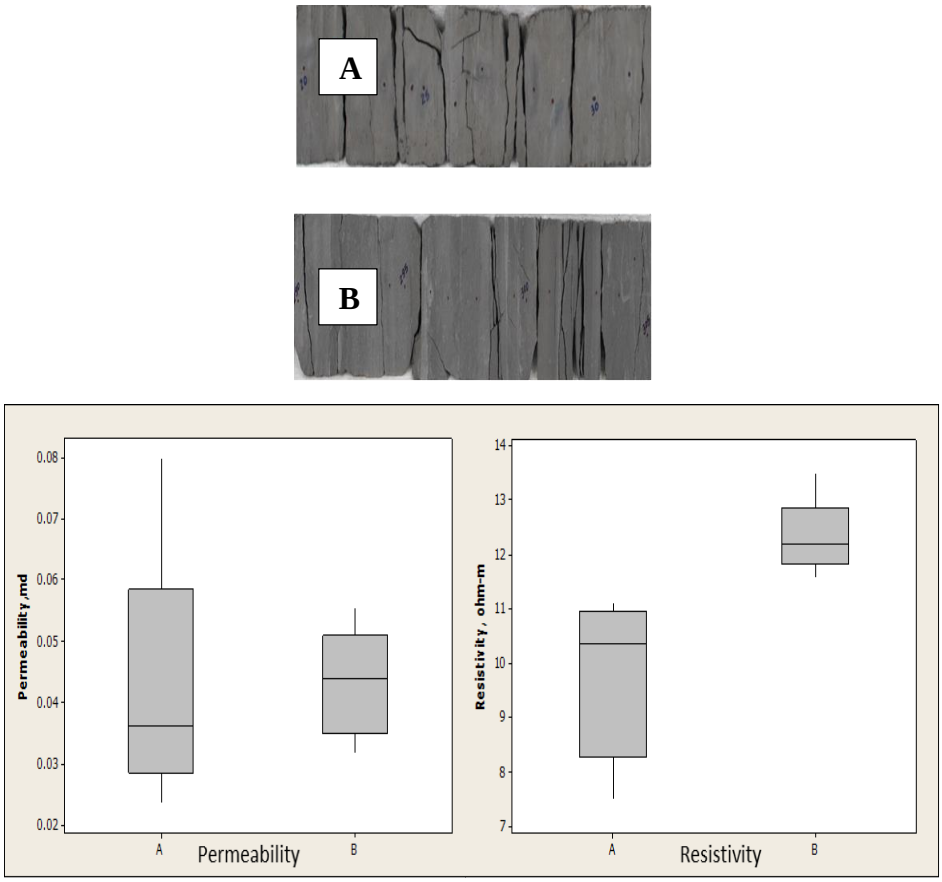

Figure 3.11. Box and Whisker plots of the permeability (left) and resistivity (right) in similar facies.

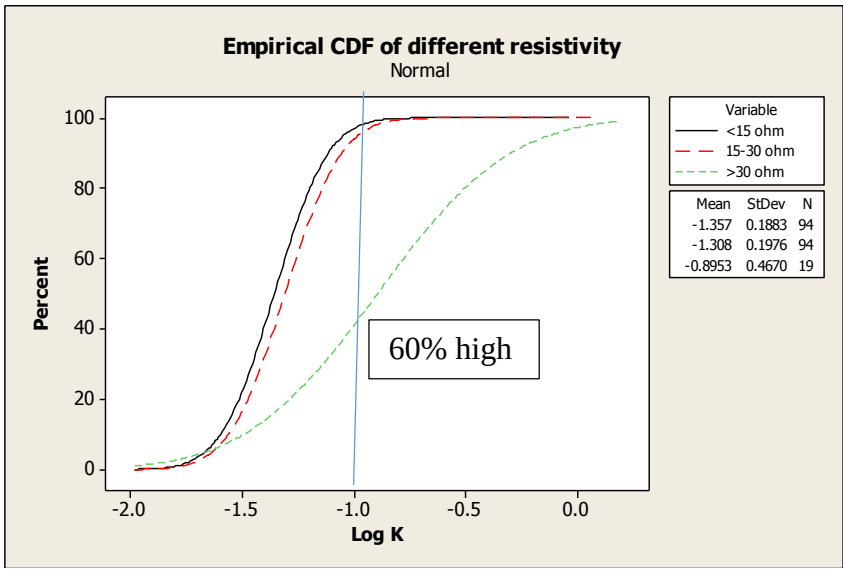

Figure 3.12. CDF of different log-permeability values in Cardium A.

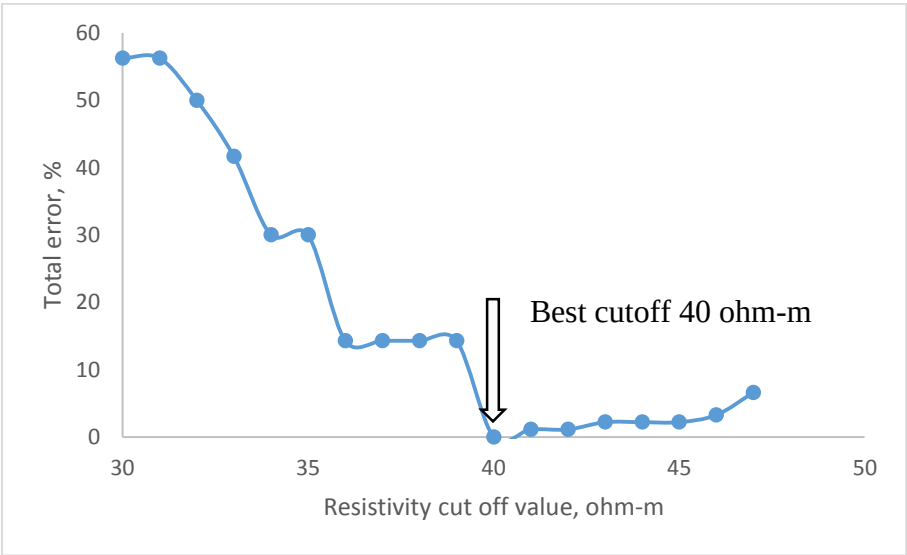

Figure 3.13. Total errors with different resistivity cutoff value.

From the experimental design, no single factor seems to have a significant effect on the permeability in the Cardium B. Evaluating the conditional probabilities, however, indicates a dependence between log (k) and log measurements. The GR log is chosen as the condition. When GR values are higher than 90 API, only small permeability values are observed. All high permeabilities come from the lower GR; in other words, there is a 70 % probability of high permeability when the GR is smaller than 90 API in the

Cardium B (Fig. 3.14). The same process is used to find the best GR cutoff value. The smallest error occurs when the GR is 88 API (Fig. 3.15).

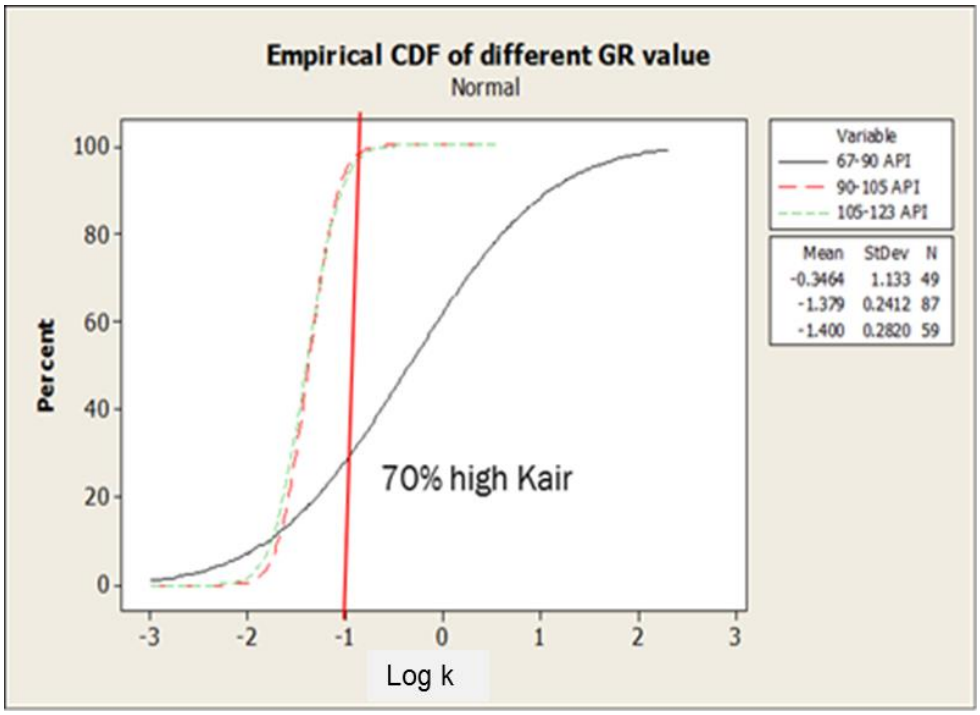

Figure 3.14. CDF of different log-permeability values in Cardium B.

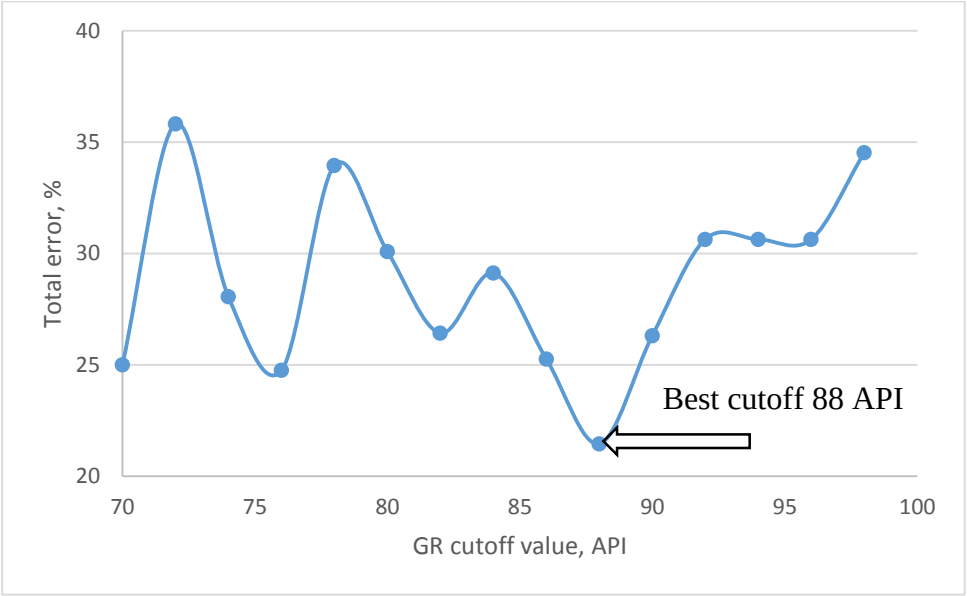

Figure 3.15. Total errors with different GR cutoff values.

3.2.2 Two-Factor Analysis

From the result of the factorial design analysis, the joint deep resistivity (A090) and gamma ray (GR) show a significant effect on the permeability in the Cardium A. But it is still difficult to correlate these two factors with permeability using a mathematical equation. Here we use the contour plot to show their relationships with permeability. The contour plot is formed by the two independent factors (such as X-GR and Y-A090) and the response (Z-permeability). Low permeability values occupy most of the zone plot (< 0.05 md), which corresponds to the lower A090 and no limitation for the GR. In the small GR (<90 API) and large A090 (>35 ohm-m) region, permeability is 0.05 to 0.1 md. With the medium permeability contour line further shrinking, GR (<75 API) and A090 (>37 ohm-m), the permeability increases to more than 0.1 md (Fig. 3.16). In the Cardium B, the combined potassium and thorium present a significant effect on the permeability. Because of the conglomerate effect, permeability in the Cardium B is larger than in the Cardium A. The high permeability values are concentrated in the small potassium and thorium region. As the values of potassium and thorium increase, the permeability decreases (Fig. 3.17), showing a similar relationship with the siltstone in the Cardium A. In the Cardium A siltstone, the permeability shows a negative relationship with the GR and SGR from the XRD in Chapter 3.

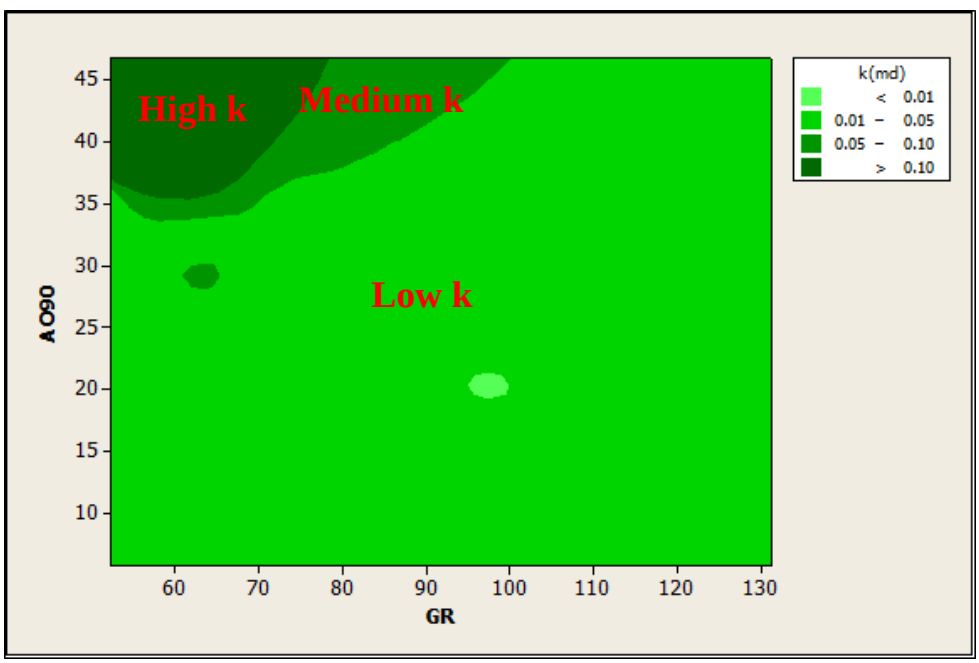

Figure 3.16. Contour plots of permeability versus A090 and GR in the Cardium A.

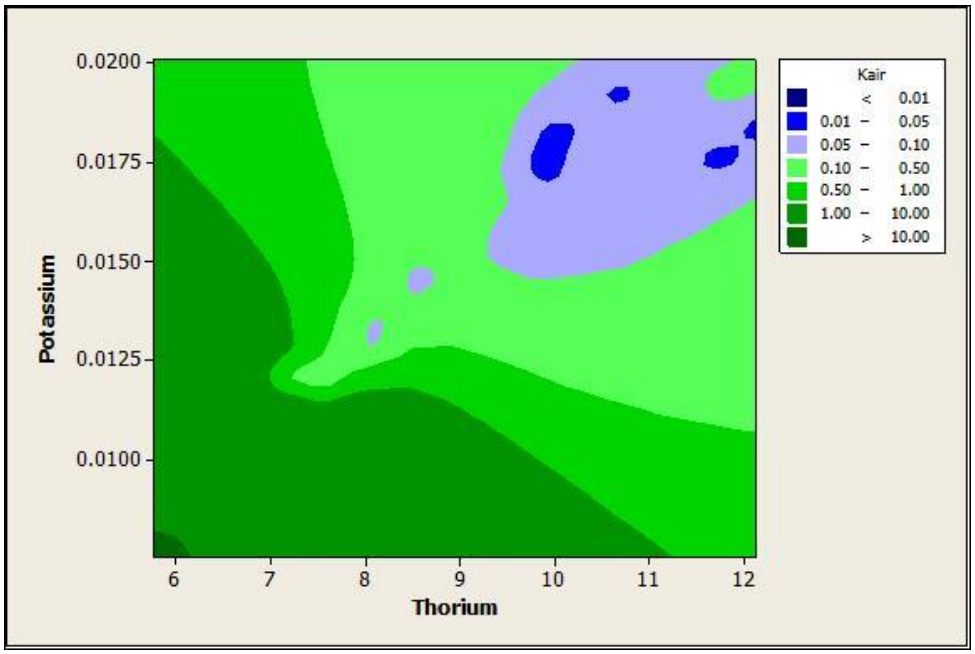

Figure 3.17. Contour plots of permeability versus potassium and thorium in the Cardium B.

3.3 Literature Permeability Calculation Model

Due to the complex nature of permeability, single or two well log factors cannot predict the whole range of permeability. Although the factor design helps to find significant factors, it is still difficult to predict the permeability using one or two factors. More potential well log factors need to be investigated. The literature is filled with reports of investigators used multiple well logs to predict permeability. Among those reports, Yao and Holditch (1993) presented a model, including porosity, deep and shallow resistivities, and GR (Eq. 3.2). Compared with other models reviewed in Section 1.2.2, their model is better suited for the lower permeability sandstone, which is similar to the tight Cardium Formation. From Chapter 2 (Figs. 2.18 and 2.19), the density porosity (ϕ_d) correlates well with the core porosity, so ϕ_d is used in the model. The A010 and A090 replace the deep and shallow resistivities, respectively from the array induction log.

$$k = \frac{U\phi^{e1}(1-\mathrm{I}_{GR})^{e2} R_{ild}{}^{e3}}{(R_{ild} / R_{sfl})^{e4}} \tag{3.2}$$

where U is a constant; ϕ density porosity; I_{GR} GR log index; R_{ild} deep resistivity (A090); and R_{sfl} shallow resistivity (A010);

Two typical intervals, shale and shaly siltstone, are applied separately with this model in the Cardium A. The model works well in the relatively clean siltstone part, where the modeled permeabilities agree with the measured values. In most of the shaly siltstone part, the model results approximate the measured permeability (Fig. 3.18 A). Permeability profiles in the Cardium A shaly siltstone correlate well with the model estimates, with a strong regression ($R^2 > 0.93$) based on the 1:1 line (Fig. 3.18 B). In the pure shale part, the correlation between the modeled and measured results is weaker than with the shaly siltstone. The actual permeability varies more rapidly than the modeled result (Fig. 3.19 A). The regression-based on the 1:1 line is weak with $R^2 = 0.40$ (Fig. 3.19 B). Comparing parameters in these two facies, the porosity shows a more significant effect on the shaly siltstone than the shale. Because of the homogeneous and tiny pores in the shale part, the porosity has not shown an effect on the permeability based on the e1 = 0 result shown in Table 3.2.

Table 3.2. Parameter values from the Cardium A and B.

Parameters	Cardium A		Cardium B	
	shaly siltstone	Shale	conglomerate	shale
U	0.0014	0.019	0.00046	0.039
e1	0.90	0	0.01	0.33
e2	0.01	0.098	0.05	0.6
e3	1.85	0.076	2.51	0.01
e4	0.69	0.10	0.3	6.39

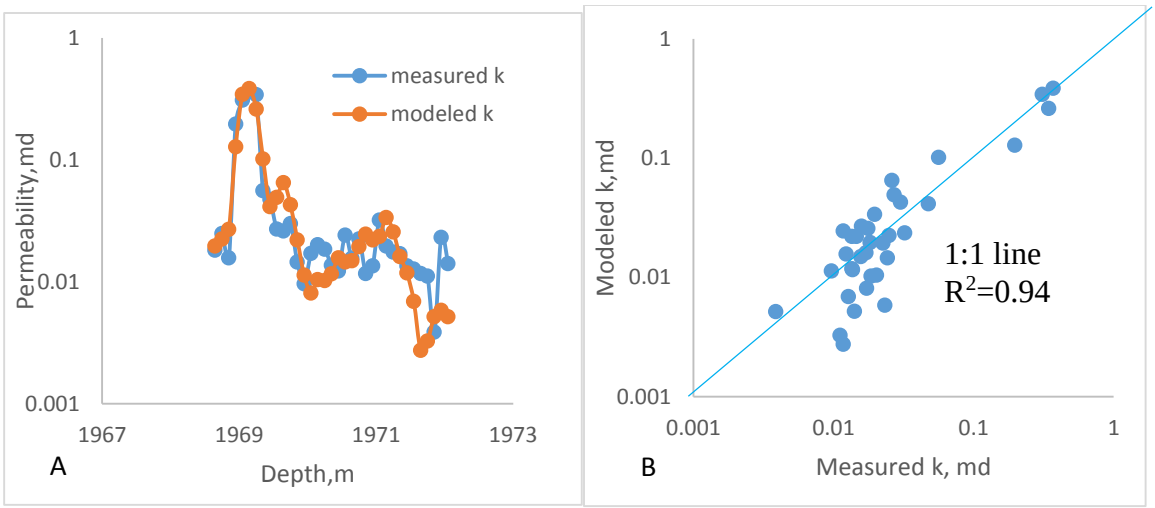

Figure 3.18. A) Measured and modeled shaly siltstone k versus depth in the Cardium A; shaly siltstone measured versus modeled k in the Cardium A.

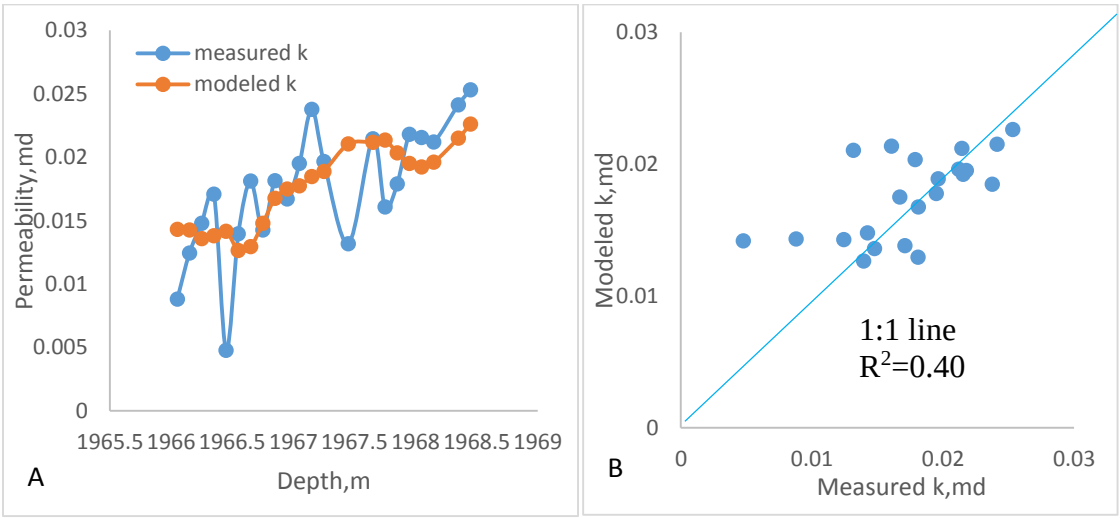

Figure 3.19. A) Measured and modeled shale k versus depth in the Cardium A; shale measured versus modeled k in the Cardium A.

The same process is repeated in the Cardium B, which has two separate facies: shale and conglomerate. In the shale interval, the result is similar to the Cardium A. The measured permeability changes more rapidly than the modeled result (Fig. 3.20). The result in the conglomerate part is not as good as in the shaly siltstone (Fig. 3.21). The conglomerate data is limited. From Yao and Holditch (1993), the model was more applicable for the shaly sands, which is supported in the Cardium Formation results. The shaly siltstone permeability can be estimated using this model more accurately ($R^2 = 0.94$) than the shale and conglomerate ($R^2 < 0.5$).

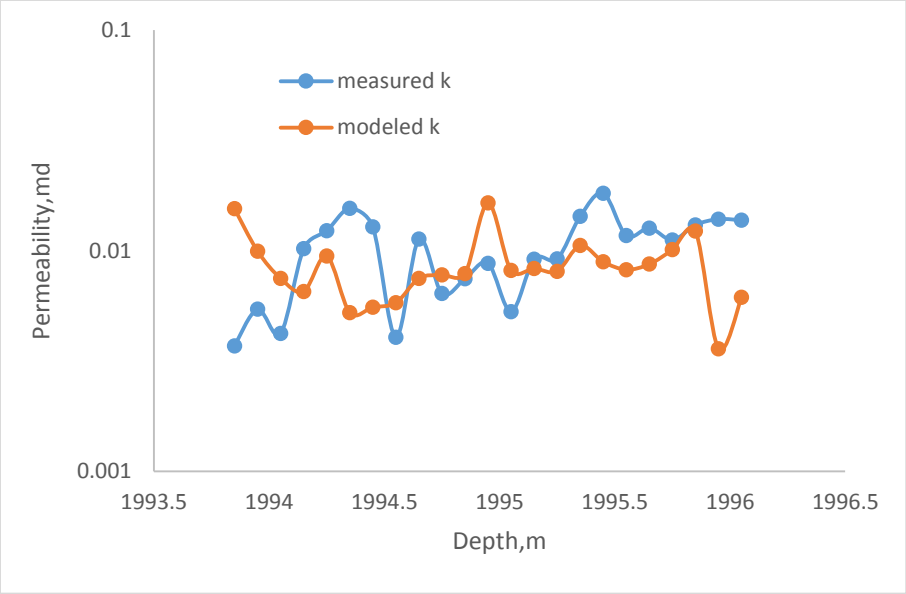

Figure 3.20. Measured and modeled shale k versus depth in the Cardium B.

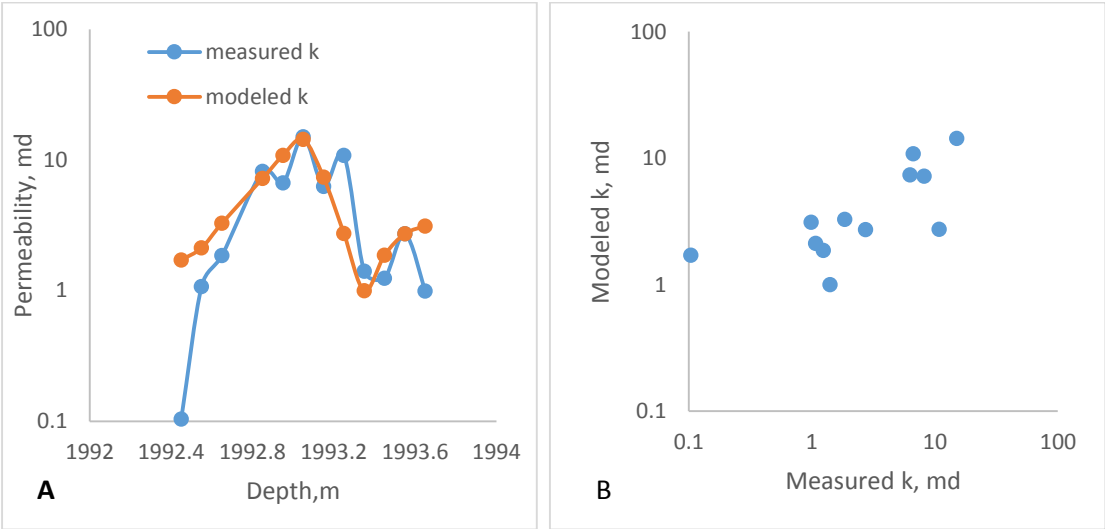

Figure 3.21. A) measured and modeled conglomerate k versus depth in the Cardium B; B) conglomerate measured versus modeled k in the Cardium B.

3.4 Semivariogram Analysis

Due to the thin laminations and small scales of reservoir layers, the probe permeability (k_p) shows a strong cyclicity (~5-10 cm) in the Cardium Formation (Fig. 3.22). These cyclicities should also be characterized by wireline logs if the logs have sufficient resolution. To investigate the cyclicity and consistency between the permeability and well

logs, a semivariogram (SV) is very useful (Jensen et al., 1996). Equation 3.3 is used to calculate the SV, where variables must be measured in the same distance. Since probe permeability measurements are not sampled with equal spacing, we chose every 10cm as one unit, then calculated the arithmetic average permeability in every unit to represent the interval. For example, at 1971.1 to 1971.2 m, the arithmetic average represents the 1971.15m. This average will reduce or eliminate some small cyclicities (less than 10 cm wavelength).

$$\gamma(\mathrm{k}) = \frac{1}{2} E\left[(\mathrm{Z}_i - \mathrm{Z}_{i+k})^2 \right] \tag{3.3}$$

where γ is semivariogram; and Z_i the variable at location i

Both the k_p and log (k_p) SV's are calculated, and these show similar trends (Fig. 3.23). The GR well log and k_p show different characteristics for the rock. The GR well log and k_p SVs present similar features overall in the Cardium A (Fig. 3.24). They both present a ~1.3 m hole effect, ie cyclicity. There are still some differences between these two SVs. The GR SV shows a steadier and smoother curve. The k_p SV curve is more varied and presents some small cycles (0.2~0.3 m). These differences are caused by different resolutions of these two measurements. The k_p has a higher resolution (~1 cm), which can reach the thin lamination scale, but the GR log can only detect bed and larger geological units. When comparing these two curves in the Cardium B, they are similar to each other (Fig. 3.25). In the Cardium B, the lithofacies does not have thin laminations, so small cycles do not appear in the k_p curve, as in the Cardium A. The SV interrogates the consistency and inconsistency between these two datasets.

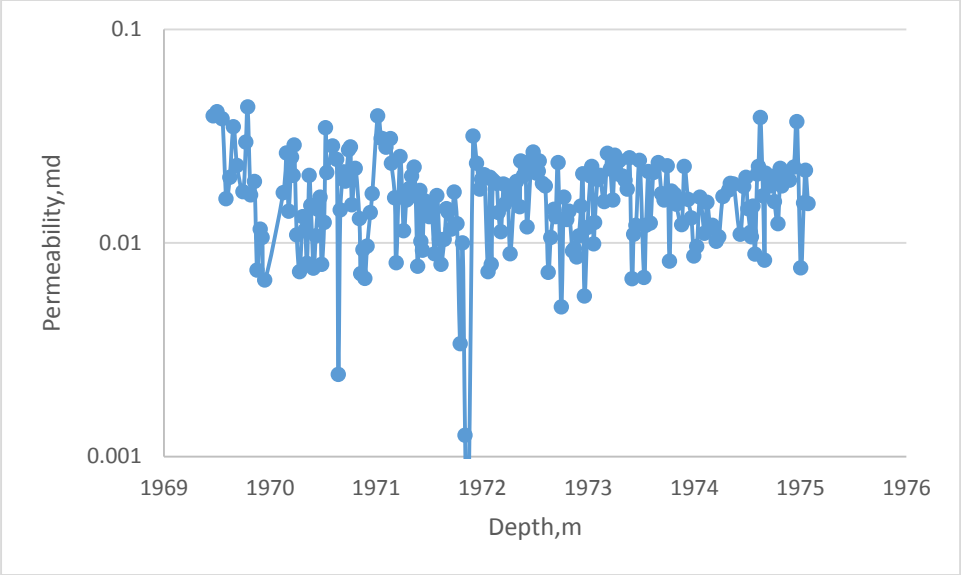

Figure 3.22. Slip-corrected probe permeability in the Cardium A.

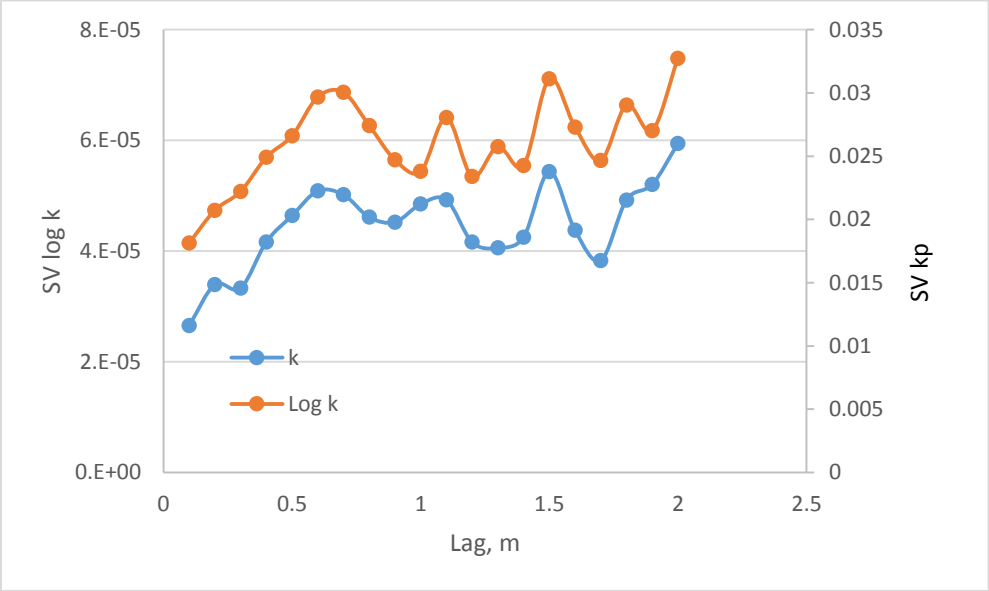

Figure 3.23. K_p and Log k_p SV in the Cardium A.

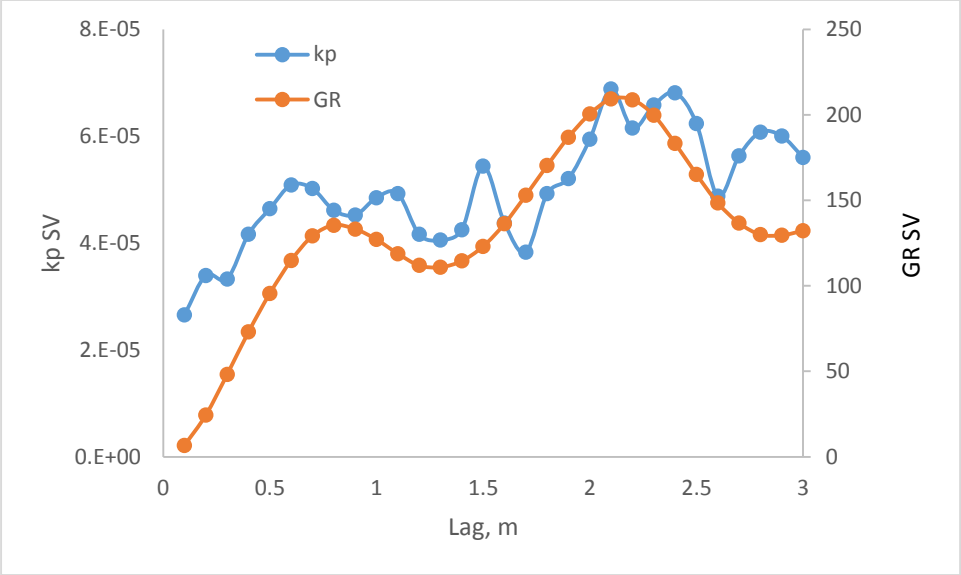

Figure 3.24. GR and k_p SVs in Cardium A.

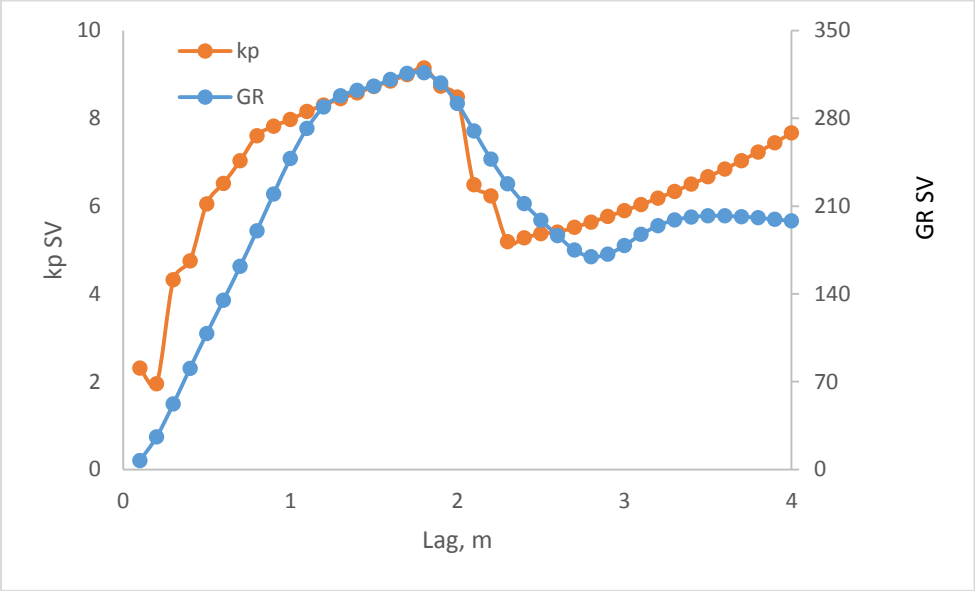

Figure 3.25. GR and k_p SVs in Cardium B.

As discussed, the SV detects the trends and cyclicities and their relationships between the well log (GR) and the probe permeability datasets in the Cardium Formation. If we decrease our focus scale from the formation to a specific small core sample, then the SV can also help to investigate the relationship between the permeability with the core image texture and fabric on a small scale. The core image SV can be calculated using Eq. 3.4, based on Eq. 3.3.

$$\gamma(\mathrm{k}) = \frac{1}{2(\mathrm{N}-k)} \sum_{i=1}^{N-k} (\mathrm{Z}_i - \mathrm{Z}_{i+k}) \tag{3.4}$$

where Z_i is the ith point pixel in the core image from Photoshop (PS); N is the number of data; and k is the lag distance.

In PS, the grey level varies from 0 to 255, where 0 and 255 represent black and white colors respectively. The 10 probe permeability measurements are processed from the middle line (labelled "medium") of the core (Fig. 3. 26). There are about 100 pixels in the PS image in the same location where k_p is measured (Fig. 3.26 below). k_p and core image SVs show similar cycles (Figs. 3.27 and 3.28). The circle in k_p SV is around 2.5cm, which is bigger than the core pixel SV. The core image pixel SV circle is around 0.5 cm, which reflects the original and smallest depositional unit. Another sample presents a steadily increase in the GR log, rock image pixel, and k_p SVs, reflecting the trend of increasing k and GR with depth (Fig. 3.29).

As a common statistic, the SV helps to "bridge" different depositional scales, from micro lamination (<1 cm) to bed (>20 cm). Between probe permeability and well log (GR as sample), the SV captures the consistency (cyclicity) and also inconsistency (resolution). The core image textural feature is quantified and connected to the permeability by the SV.

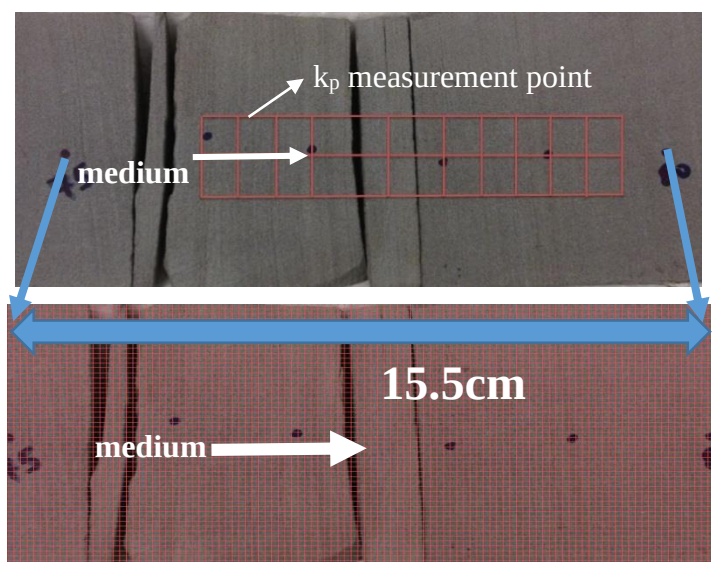

Figure 3.26. Actual (above) and processed (below) core imaged from Cardium A.

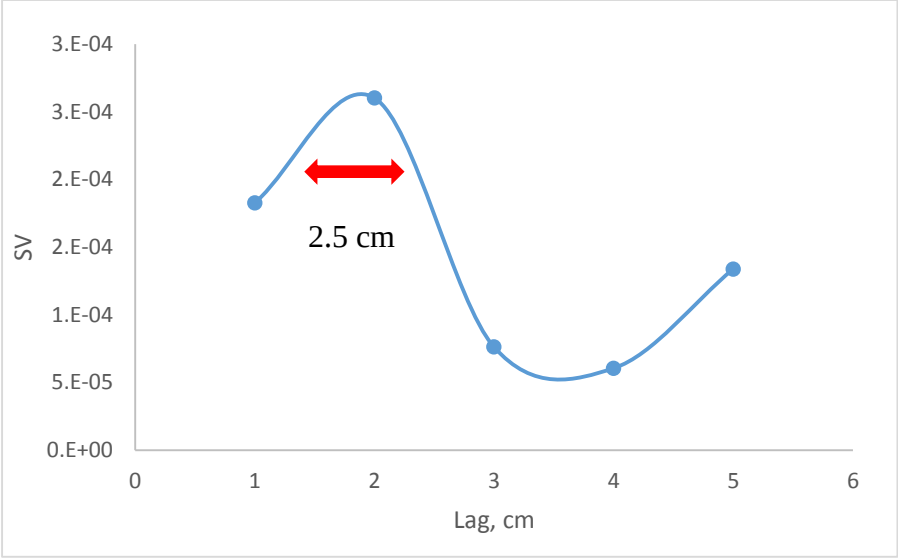

Figure 3.27. Probe permeability SV plot.

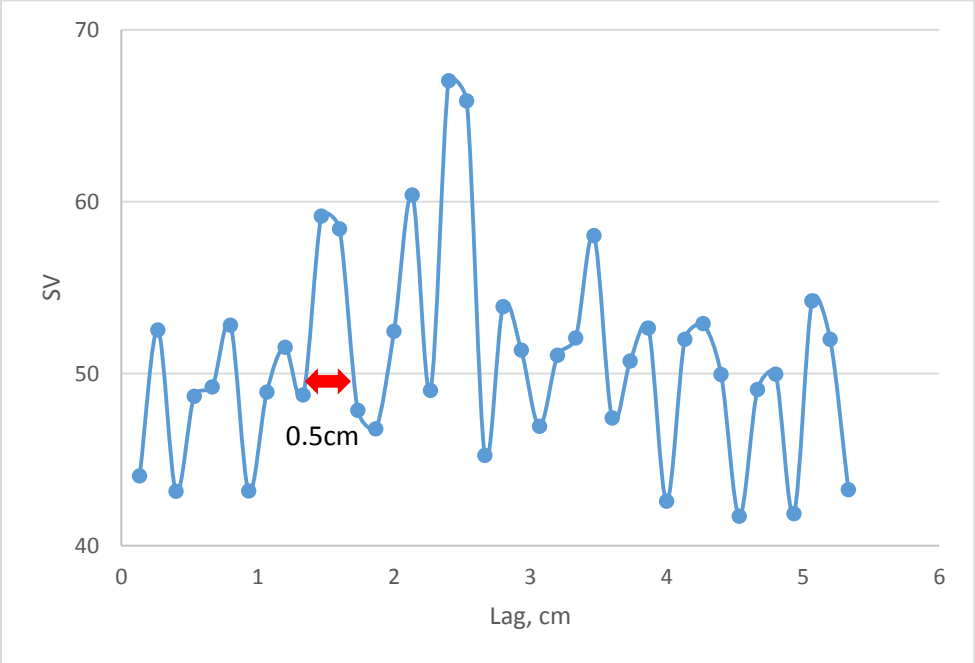

Figure 3.28. Core image pixel SV plot.

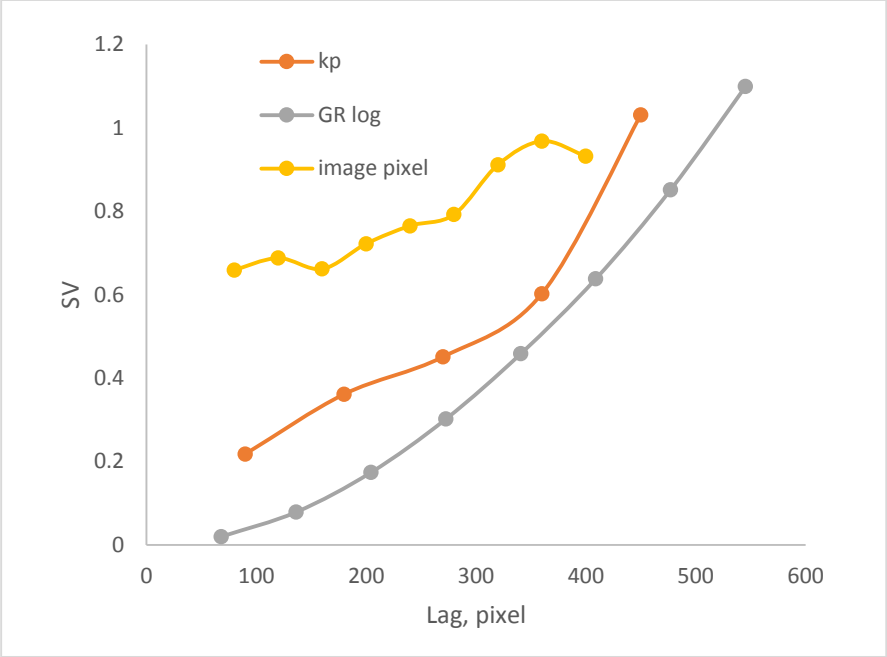

Figure 3.29. GR log, core image pixel, and k_p SVs.

CHAPTER 4: COMBINING NMR LOG AND PROBE PERMEABILITY TO PREDICT WHOLE CORE PERMEABILITY

4.1 Introduction

Following the discussion in Chapter 3, it is difficult to estimate the tight Cardium permeability using conventional well logs. Extremely low and highly variable values and the changing scales of these variations are major challenges to tight rock permeability prediction. Further challenges arise when well logs are used to predict permeability. The strong heterogeneity creates problems for permeability estimation using conventional logs in tight formations.

Nuclear magnetic resonance (NMR) logs have been used to predict permeability in conventional sandstone rocks with good success (Lowden, 2003; Minh, 2006; Daigle and Dugan, 2009) but their application in tight rocks has been more problematic. Two empirical models, the Schlumberger-Doll Research model (SDR, Eq. 4.1) (Kenyon et al. 1989) and the Timur-Coates model (TIM, Eq. 4.2) (Coates et al. 1991) have been widely used in conventional reservoirs.

$$k_{SDR} = a\phi^4 T_{2LM}{}^2 \tag{4.1}$$

where a is an empirical constant, T_{2LM} is the logarithmic mean of the transverse relaxation time T_2, and ϕ is the NMR porosity.

$$k_{TIM} = b\phi^4 \left(\frac{FFI}{BVI}\right)^2 \tag{4.2}$$

where b is an empirical constant, *FFI* is the free fluid volume, and *BVI* is the bound fluid volume.

These two methods give large errors when applied in tight formations. The SDR equation includes the mean of T_2, which doesn't cover all pore information and ignores contributions from small pores. The effect is amplified in tight formations, which have many small shale laminations between siltstones. These shale laminations play an

important role for the vertical permeability, which the SDR derived permeability will overestimate. The TIM model is not directly related to T_2, but depends on the T_2 cut off determination. Generally, 33 ms is selected for the T_2 cutoff in sandstone, which has been acknowledged to be an overestimate in tight formations (Xiao et al., 2011; Kerimov, 2013).

This chapter presents a new NMR-based permeability estimate which shows greater accuracy than the SDR and TIM models in a tight formation. It is independent of T_2 and cutoff values and includes more pore information. The model also helps to relate permeability measurements which have different scales and resolutions.

4.2 Data Set Description

Two typical intervals (1968.27-1972.45 m and 1989.89-1993.64 m) were chosen for routine core analysis on full diameter samples. The air permeability was measured at steady-state with a 3.45 MPa net confining pressure from three directions. In addition to the routine core analysis, probe permeameter (k_p) data were measured. A difficulty for tight formation permeability estimation comes is the inconsistency between these measurements. We analyzed probe and whole core permeability measurements for the Cardium core. Because these are common permeability measurements, many studies have described the methods and their comparison (e.g., Collins, 1952; Corbett and Jensen, 1992; Jones, 1994; Clarkson et al., 2012). In homogenous formations, some studies have reported agreement between probe and core permeability (e.g., Goggin et al., 1988; Garrison et al., 1996). However, in heterogeneous facies, the probe permeability values have been found to be larger than the core values; in some cases, there was more than one order of magnitude difference (Georgi and Jones, 1992; Gibbons et al., 1993; Meyer and Krause, 2001). In the Cardium A, the probe permeabilities show mixed relationships with horizontal (k_{max}) and vertical permeability (k_{vert}) (Fig. 4.2). Most k_{max} values are larger than k_p, some by more than one order of magnitude. Some samples however, such as Samples 1 and 5, show a good correspondence. The relations between k_{vert} and k_p are also mixed (Fig. 4.1), with good agreement for Samples 7 and 9, and 10, but weaker agreement for Samples 2 and 4. In general, the more variable is k_p, the more likely there

is disagreement between k_p and either k_{max} or k_{vert}. Similar trends between these measurements appear for the Cardium B data (Fig. 4.2).

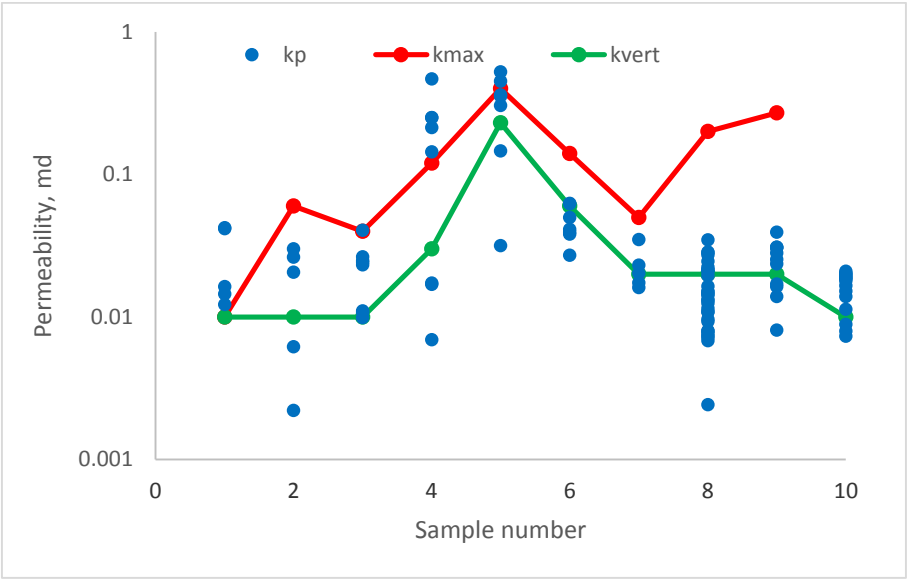

Figure 4.1. k_p ,k_{max}, and k_{vert} measurements from the Cardium A.

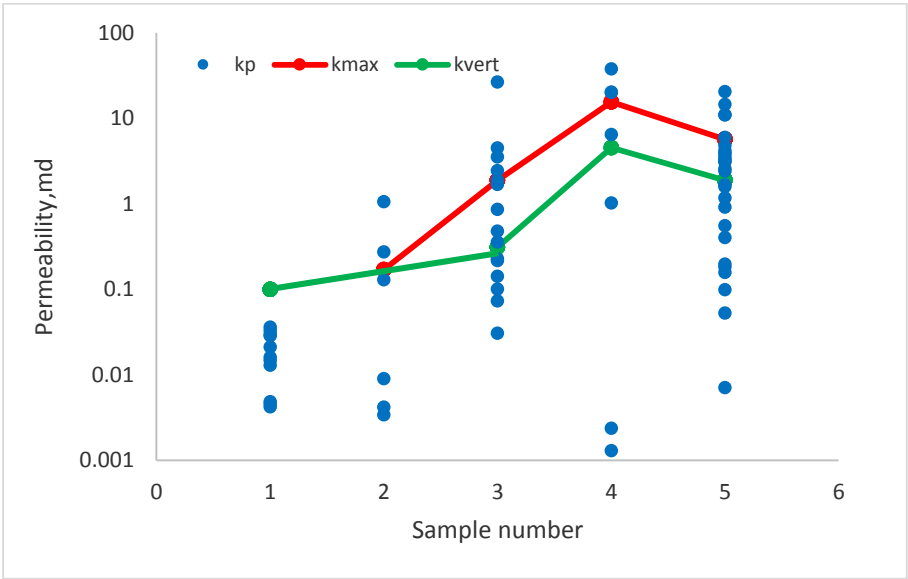

Figure 4.2. k_p ,k_{max}, and k_{vert} measurements from the Cardium B.

Except for the inconsistent value between these two measurements, direction cannot unify. For example, whole core permeabilities are divided into horizontal and vertical, but it is difficult to give a direction for probe permeability. One approach described by Corbett and Jensen (1992) to reconcile whole core and probe measurements is in the case

of laminated sediments. We assume that the core is well laminated with shale and siltstone (Fig. 4.3). The probe permeability is measured with a millimeter-scale probe tip and, when the tip is located between boundaries, it represents a unique facies value (Fig. 4.3 circle). If the probe permeability of the specific facies and their proportion are determined, the whole core permeability can be estimated by applying the arithmetic and harmonic averages to the probe values.

In order to estimate the proportions of the lithofacies, we use the NMR log. Different facies typically can be characterized by pore size. For example, shale contributes most of the micropores. The NMR T_2 spectrum provides the pore size distribution, giving a pore size-related lithofacies model with parameters derived from T_2 spectrum.

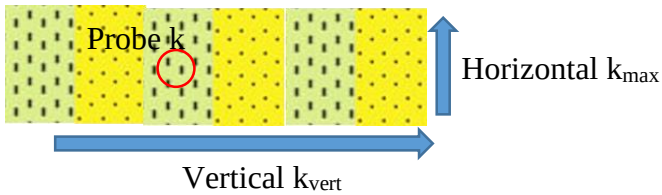

Figure 4.3. Core sample with shale and siltstone laminations showing core permeability measurements and a possible location for a probe permeability measurement (red circle).

4.3 NMR T_2 Processing for Lithofacies Proportions

4.3.1 NMR Response Physics

The NMR log is a useful and advanced tool for permeability prediction, compared to conventional logs. Its response is independent of complex geological parameters, such as lithofaces, and minerals et al, but it is mainly affected by pore fluids. From the NMR log, we can interpret porosity, and bound and free fluids (Fig. 4.4). The porosity from the NMR usually underestimates the core porosity in the Cardium Formation. The NMR based porosity is still greater than the density porosity because of complicate matrix (Fig. 4.5). However, the NMR biggest advantage comes from the T_2 spectrum, which is a rich source of pore information.

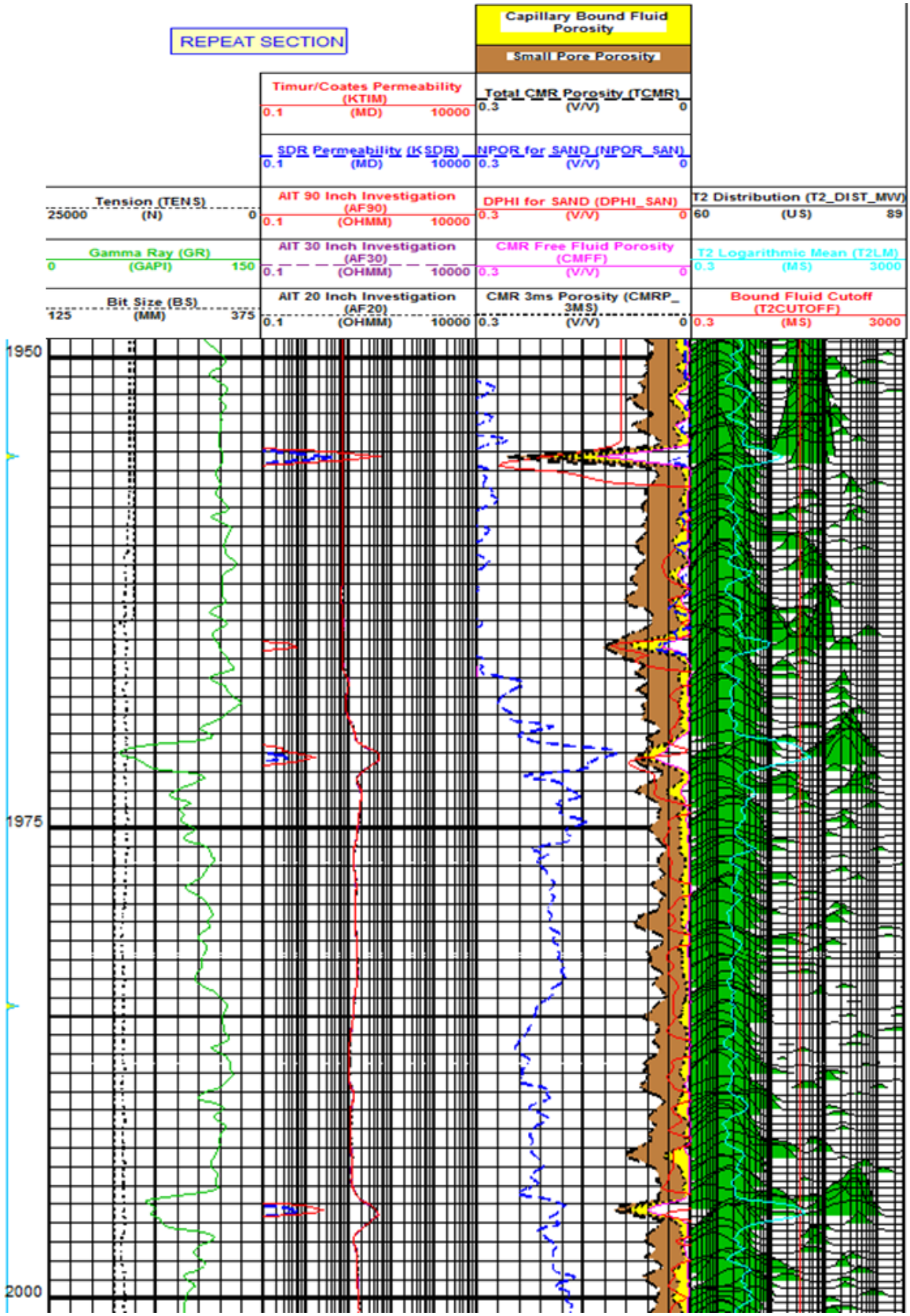

Figure 4.4. NMR interpretation plot in the Cardium formation (Schlumberger, 2010).

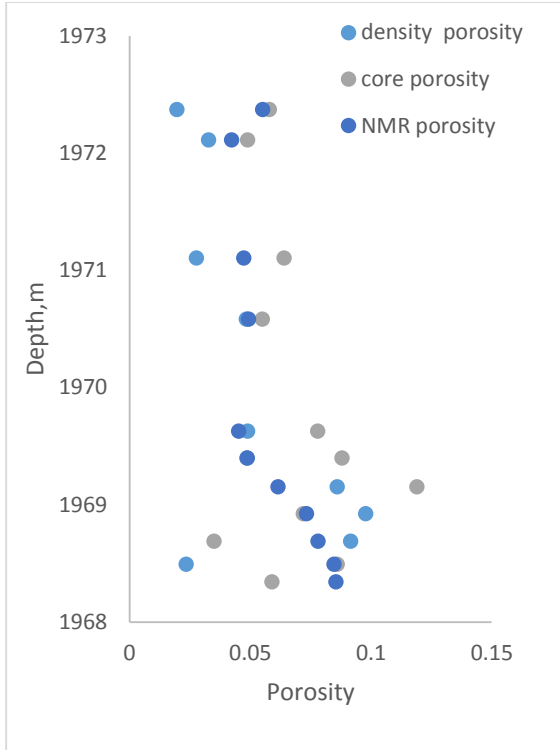

Figure 4.5. Core, density, and NMR porosities in the Cardium A.

The NMR T_2 relaxation time depends on fluid in the rock pores. There are main three relaxation components: bulk fluid process (T_{2bulk}), surface relaxation ($T_{2surface}$), and magnetic field gradient diffusion ($T_{2diffusion}$). T_2 is characterized by Eq. 4.3 (Kenyon, 1992). Because the Cardium Formation contains mostly water and light oil, T_2 is dominated by $T_{2surface}$. Therefore, we neglect the T_{2bulk} and $T_{2diffusion}$ components in the remaining discussion. $T_{2surface}$ is given by Eq. 4.4 (Kenyon, 1992). The NMR T_2 is proportional to the pore size.

$$\frac{1}{T_2} = \frac{1}{T_{2bulk}} + \frac{1}{T_{2surface}} + \frac{1}{T_{2diffusion}} \tag{4.3}$$

where T_{2bulk} relaxation time of the pore fluid; $T_{2surface}$ pore fluid surface relaxation; $T_{2diffusion}$ magnetic field gradient diffusion.

$$\frac{1}{T_{2surface}} = \rho_2 (\frac{S}{V})_{pore} \tag{4.4}$$

where ρ_2 surface relaxivity parameter; $\left(\frac{S}{V}\right)$ pore surface to pore volume.

4.3.2 Pore Size Distributions and T_2

Several studies have indicated that pore size is log-normally distributed (LND). The mercury intrusion porosimetry method has found LND pore sizes in cemented sediments (Diamond and Dolch, 1971, 1972; Shi, et al., 1991). Lindquist and Venkatarangan (2001) also found a LND sandstone pore sizes using X-ray tomographic image analysis. Another technique, the mercy injection capillary pressure test, (CMICPT) was used by Chuanyan et al. (2013), which also showed LND pore sizes in very tight core samples.

Since T_2 is directly proportional to pore size (Coates et al., 1999), the T_2 spectrum is also expected to be LND. Because the volume of investigation of the NMR response will likely include several lithofacies, the log (T_2) distribution may be expected to be a mixture of several normal distributions. Thus, the log (T_2) distribution needs to be decomposed in order to identify the lithofacies components and their proportions. This idea is similar to Genty et al.'s (2007) work, which used the NMR log to quantify porosity types in carbonate reservoir rocks. They used three Gaussian distributions (Eq. 4.5) to decompose the log (T_2) spectrum and got at most three components with nine parameters. The coefficient R^2 was used to assess the match (Eq. 4.6).

$$f_{\mathrm{model}}(\mathrm{T}_2^{'}) = \mathrm{A}\sum_{i=1}^{3}(\alpha_i)g_i(\mu_i,\sigma_i,\mathrm{T}_2^{'}) \tag{4.5}$$

where $g_i = \frac{1}{\sqrt{2\pi\sigma_i^2}}\exp\left\{-\frac{(\mathrm{T}_i-\mu_i)^2}{2\sigma^2}\right\}$, f_{model} is the approximated spectrum,

$T_2^{'} = \log(\mathrm{T}_2)$ and μ_i and σ_i are the mean and standard deviation of the ith component, respectively. A is a constant and:

$$R^2 = 1 - \frac{\sum(f_{mea}(T_{2,i}^{'}) - f_{\mathrm{model}}(T_{2,i}^{'}))^2}{\sum(f_{mea}(T_{2,i}^{'}) - \overline{f_{mea}(\mathrm{T}_{2,i}^{'})})^2} \tag{4.6}$$

where $f_{mea}(T'_{2,i})$ is the measured NMR response and $\overline{f_{mea}(T'_{2,i})}$ is the average of the measured NMR responses.

A similar method can be applied in tight clastic cases. We use Eq. 4.5 to fit and decompose the NMR T_2 spectrum. f_{model} fits well with the measured data (R^2 = 0.97, Fig. 4.7A). After the decomposition, there are nine parameters (μ_i, σ_i, and α_i for i = 1, 2, and 3) which show a relationship with pore characteristics (Fig. 4.6B). The components represent pore types with different sizes. According to the IUPAC classification (Everett, 1972), pore size is divided into three groups, which are micropores (<2 nm), mesopores (2-50 nm), and macropores (>50 nm).The first peak (smallest T_2 and i = 1) usually indicates micro-pores and is characterized by the first three parameters α_1, μ_1, and σ_1. α_1 is the proportion of the first pore type. These micro-pores mainly come from shale. Actually, α_1 is the representation of all rock types with micropore. Other facies such as siltstone can also contribute micro-pores but in this study, we assume that all micro-pores are in the shale. In this sample, α_1 = 0.37, which is interpreted as 37% of the sample porosity consists of micro-pores. For the micro-pores, μ_1 represents the log-mean pore size. Samples in strongly cemented and compacted conditions will have smaller μ_1. σ_1 reflects the log-standard deviation of the pore sizes that is determined by sorting. The parameters α_2, μ_2, and σ_2 for the second peak can be interpreted with a similar logic. The medium pores usually come from fine siltstone. The third component (if it exists) represents the largest pores, coming from coarse siltstone or sandstone. According to the geological interpretation for the nine parameters, a simple pore size related facies model (fine size – shale, medium size – fine silt, and coarse size – coarse silt or sand) can be constructed (Fig. 4.7).

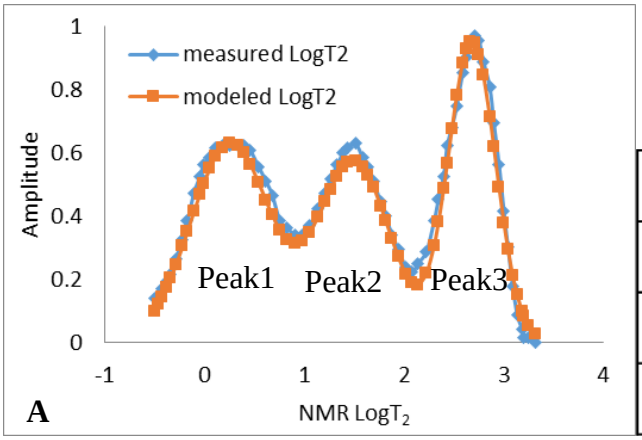

α_1=0.37	α_2=0.3	α_3=0.33
μ_1=0.26	μ_2=1.49	μ_3=2.67
σ_1=0.39	σ_2=0.35	σ_3=0.23
R^2=0.97		**B**

Figure 4.6. A) Example decomposition of Cardium B Log T_2 spectrum; B) Nine parameters from the decomposition

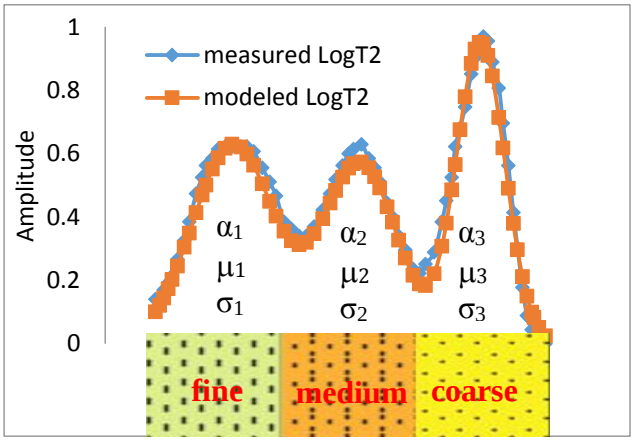

Figure 4.7. Pore size related lithofacies model and associated responses on the NMR log (T_2) spectrum.

4.4 Model Testing

The decomposition interpretation is based on several assumptions. We need therefore to test if these parameters are consistent with our actual core characteristics. We chose seven core samples from the Cardium A and B to compare with NMR decomposition results. For the pore size related facies model, there are three lithofacies with weights of α_1, α_2, and α_3. If α_i is consistent with the proportion of the appropriate facies from core analysis, it suggests that our interpretation of the parameters α_i is correct. The medium and coarse pore-size related facies are not easily identified in the tight Cardium formation, so in this study we use shale (α_1) as the best test.

We used image analysis for the determination of the shale proportion. In the conglomerate, the core comprises grains and matrix (Fig. 4.8A). They have different colors; the grain is white and the matrix is gray. We assume all the shale comes from the matrix. Using an image processor (Photoshop, PS), we can identify these two components using color range selection. Even very small grains can be detected, which makes the shale proportion estimate accurate (Fig. 4.8B). For the thin laminated shaly siltstone, it is difficult to distinguish the shale and siltstone visually (Fig. 4.9A). But, compared to the siltstone, the shale has more black, which can be detected by PS. After processing, the tiny shale layers can be distinguished and the proportion calculated (Fig. 4.9B). Figures 8 and 9 show binary-colored samples; because of sediment complexity however, sometimes 2 colors do not cover all components. The grains in the Cardium B, for example, show 2 color categories, black and white. The matrix is light yellow (Fig. 4.10A). In order to calculate the grain proportion, black and white are first selected (Fig. 4.10B and C). Then, after repeating the color selections, grain and matrix are distinguished.

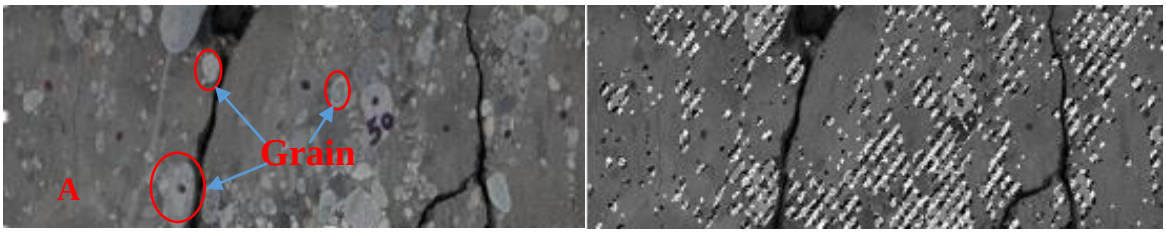

Figure 4.8. A) actual conglomerate core image; B) processed conglomerate core image in the Cardium A.

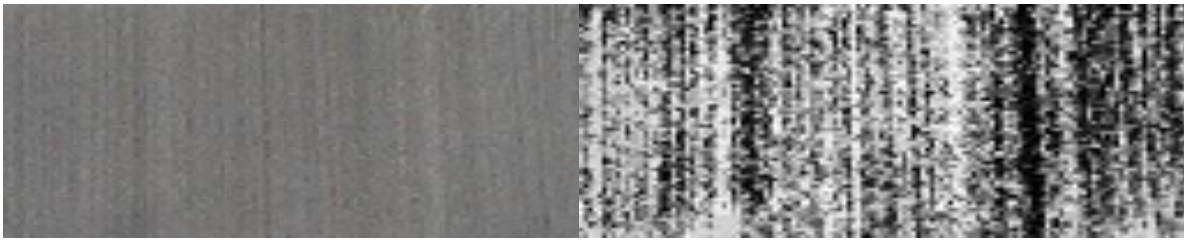

Figure 4.9. A) actual tiny laminated shaly siltstone; B) processed tiny laminated shaly siltstone in the Cardium A.

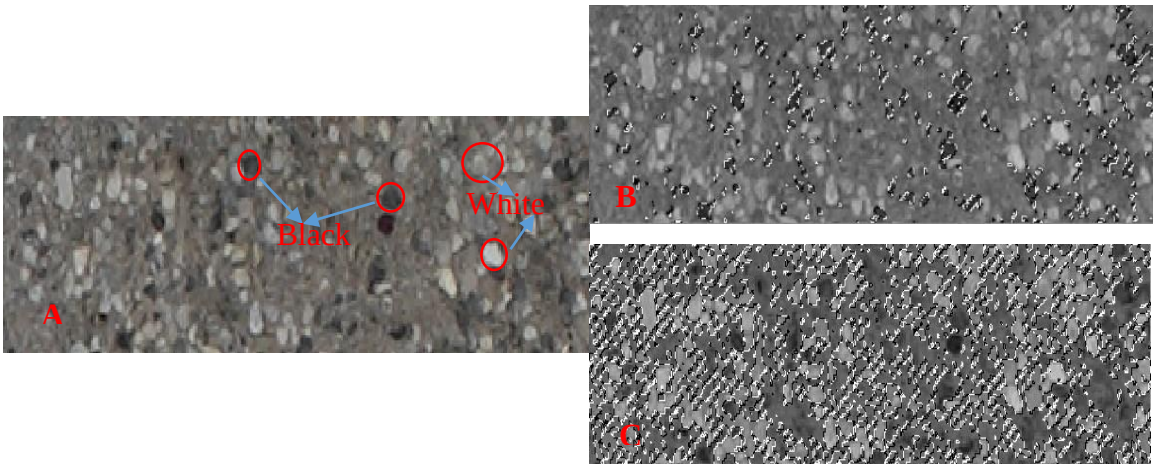

Figure 4.10. A) actual conglomerate core image; B, C) processed conglomerate core image in the Cardium B.

The NMR measurements of these intervals are analyzed to get α_1. If our interpretation regarding α_1 is correct, the shale proportions from core analysis should agree with the α_1 in the same sample. There is a strong relation between them in the Cardium A (Fig. 4.11A), meaning that α_1 from NMR is a good estimator for the shale proportion. Similar results are obtained in the Cardium B (Fig. 4.11B). The core image analysis results can be affected by the color threshold setting. For example, the color tolerance of 32 is used to identify shale and grain in the conglomerate shown in the Figure 4.8. If we change the threshold from 27 to 37 (± 16%), the proportions change by ± 2%. The core image derived shale proportion is affected by the color threshold value, but the effects are insignificant.

Besides the core image analysis, X-ray diffraction (XRD) can also be a measure of shale proportion. We processed five XRD analyses made on the formation. The relation between XRD clay content and α_1 appears to be a moderately strong linear relation (Fig. 4.12) but the XRD clay content is less than α_1. Two possible reasons account for the line not passing through the origin. One reason is that the shale (detected by α_1) is constituted not only by the clay minerals (as detected by XRD), but also tiny fragments and other minerals, especially quartz minerals. The other reason is because of the resolution difference of these two measurements; the XRD is more localized than NMR logs. In summary, these examples indicate α_1 correlates well with shale volume proportions.

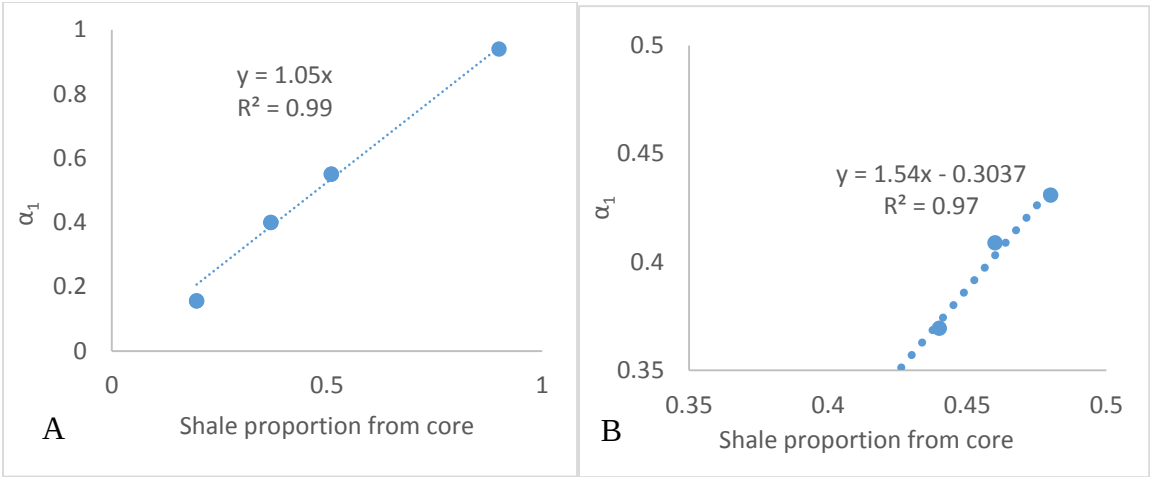

Figure 4.11. Shale proportion from core image versus α_1, A) is the Cardium A; B) is the Cardium B.

Besides our core samples, there are published studies that have shale proportions and NMR measurements. We used our model to fit these log (T_2) spectra and compared the α_1 with shale proportions. Minh and Sundaraman (2006) built a laminated sand-shale model and measured the NMR response. In this model, there is approx. 40% shale and 60% sandstone and the NMR measurement showed a bimodal response (Fig. 4.13). We used Eq. 4.5 to fit this curve. The model curve is matched well with the measured curve (R^2 = 0.98, Fig. 4.14 A and B). α_1 = 0.43, agreeing well with the laminated model value of 0.4.

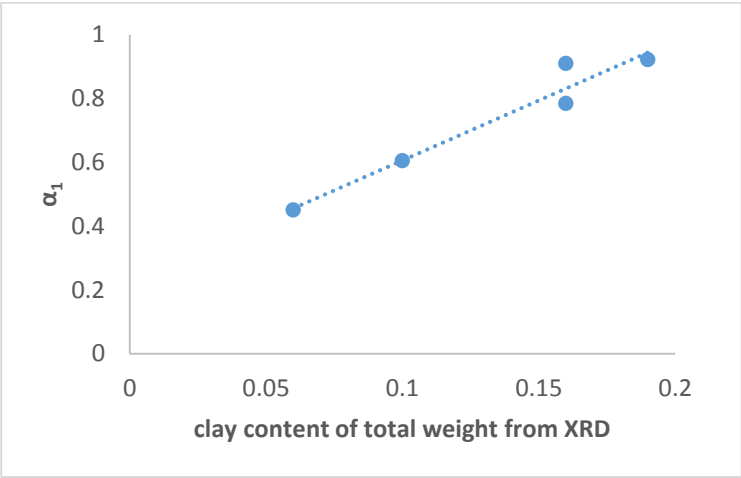

Figure 4.12. XRD clay content versus α_1.

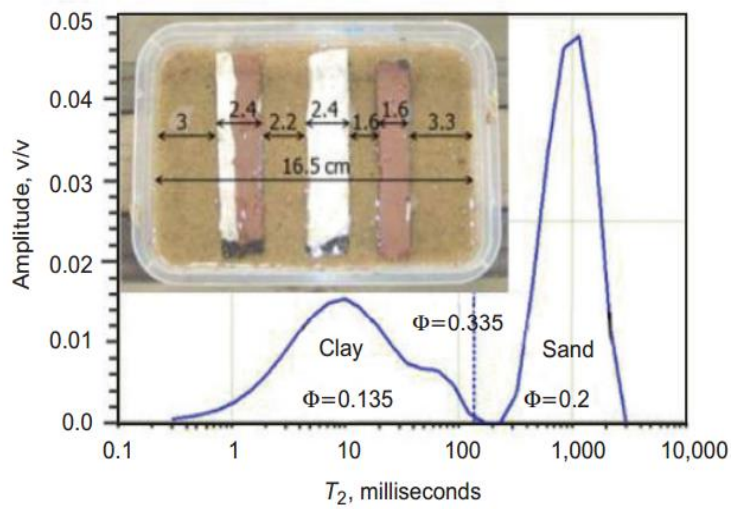

Figure 4.13. NMR experimental results of sand-shale laminations (Minh and Sundaraman, 2006).

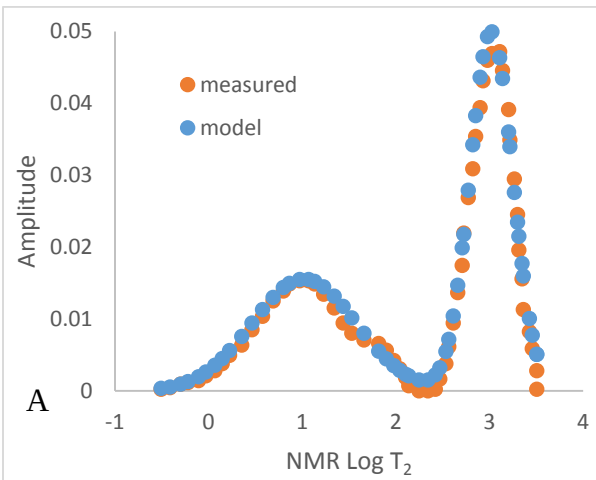

α_1=0.43	α_2=0.57
μ_1=1.02	μ_2=3.02
σ_1=0.55	σ_2=0.23
R^2=0.98	B

Figure 4.14. A) Measured (from Minh and Sundaraman, 2006) and modeled log T_2 curves; B) parameters from the decomposition.

Besides laboratory models, there are data from borehole measurements and core. For example, there is a 4.0 ft sample, which consists of 1.31 ft sand and 2.69 ft shale as measured from core (Minh and Sundaraman, 2006). This sample gives a 67% shale proportion and our analysis of the NMR data shows very good agreement with α_1 = 0.7 (Fig.4. 15). Summarize all 8 literature sample results, our model parameter α_1 correlates well with the micropore proportions (R^2 = 0.97, Fig. 4.16).

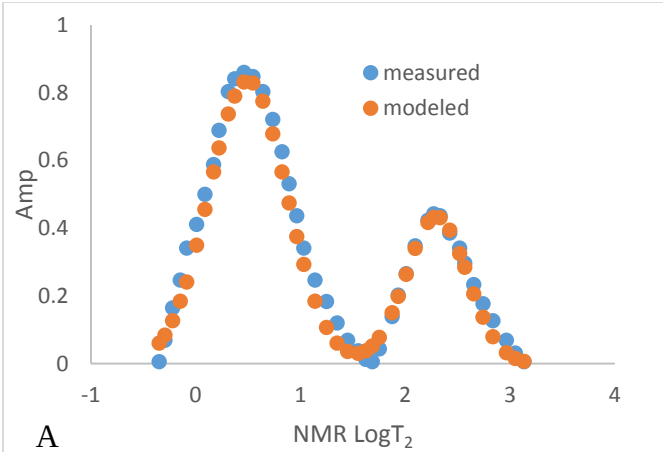

α_1=0.70	α_2=0.30
μ_1=0.49	μ_2=2.3
σ_1=0.37	σ_2=0.29
R^2=0.97	B

Figure 4.15. A) Borehole measured (from Minh and Sundaraman, 2006) and modeled log T_2 curves; B) parameters from the decomposition.

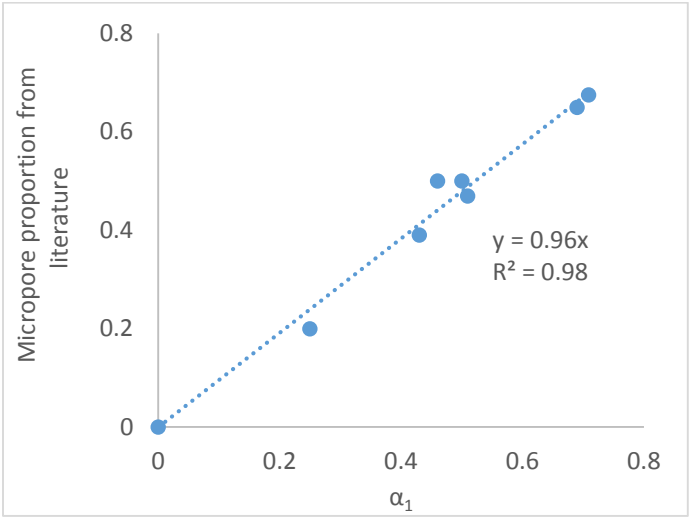

Figure 4.16. Micropore proportions (collected from Ostroff et al., 1999 Minh and Sundaraman, 2006; Bansal, 2013) versus α_1 from log T_2 decomposition.

4.5 Permeability Prediction

For the pore size model, different layers have specific proportions α_i and permeability k_i (Fig. 4.17). If α_i and k_i are known, the whole sample k_{along} and k_{across} can be calculated. When the flow is along the layers (Fig. 4.17A), k_{along} is obtained using Eq. 4.7 and corresponds to the whole core horizontal measurements (k_{90} and k_{max}). When the flow is

across layers (Fig. 4.17B), k_{across} is calculated using Eq. 4.8 and corresponds to the whole core vertical measurement (k_{vert}).

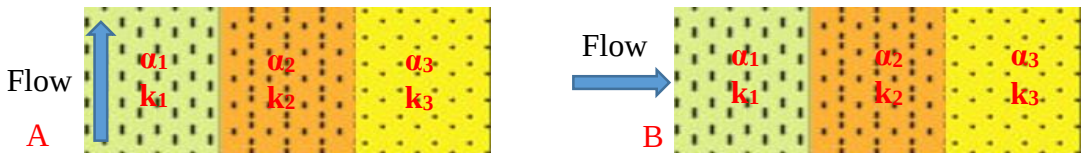

Figure 4.17. A) Flow along the layers; B) flow across the layers.

$$k_{along} = \sum_{i=1}^{3} \alpha_i k_i \tag{4.7}$$

$$k_{across} = \frac{1}{\sum_{i=1}^{3} \frac{\alpha_i}{k_i}} \tag{4.8}$$

We have confirmed that α_1 from the log T_2 spectral decomposition can represent shale proportions. Due to its high resolution relative to lamination thicknesses, the probe permeability may represent a unique facies value (Fig. 4.3). For each facies permeability k_i, the probe permeability can be used. Some sample measurements are strictly in shale (Fig. 4.18A) where the probe permeabilities (k_p) are samples of k_1 (Fig. 4.18B), which is not a single value but represents the distribution of possible shale permeabilities. A probability plot of k_p from very shaly intervals shows an LND (Fig. 4.19) with log k_1~ N (-1.88, 0.24^2). The permeability of the micro-pore rock can be described by this LND with log-mean -1.88 and log-variance 0.24.

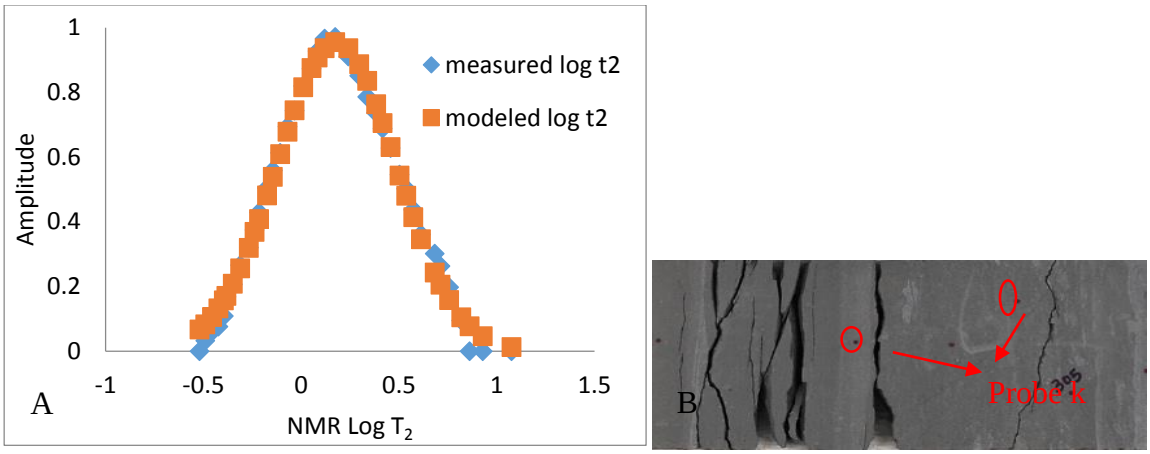

Figure 4.18. A) T_2 spectrum of very shaly zone (α_1 = 1) in Cardium A; B) probe measurement locations on the core.

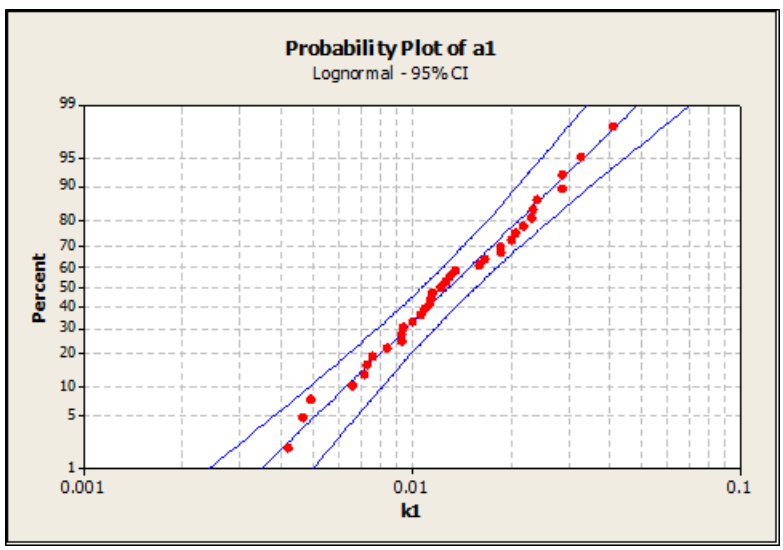

Figure 4.19. Probability plot of probe permeability from facies i = 1 in the Cardium A.

From the LND, we estimated the mean value for k_1 using Eqs. 4.9 and 4.10 (Agterberg ,1974):

$$\overline{k_1} = e^{\overline{\log x}} . \psi_n (s^2/2) \tag{4.9}$$

$$\psi_n(t) = 1 + \frac{n-1}{n} t + \frac{(n-1)^3}{n^2(n+1)} \frac{t^2}{2!} + \frac{(n-1)^5}{n^3(n+1)(n+3)} \frac{t^3}{3!} + \ldots \tag{4.10}$$

where $\overline{\log x}$ is the log-mean, s^2 is the log-variance, $t = s^2/2$, and n is the number of measurements.

k_1 = 0.014 md. The i = 2 and i = 3 facies permeabilities cannot be determined directly as we did with the shale facies because there are no samples with 100% α_2 or α_3 in this Cardium core. Moreover, distinguishing α_2 and α_3 from each other is quite difficult. So here we regard α_2 and α_3 as one lithotype. We chose some relatively "clean" samples. Those probe permeabilities are still affected by any shale present with permeability k_1. We removed the effect of k_1 using Eq. 4.11. The corrected probability plot of k_{2+3} also shows an approximately LND (Fig. 4.20), with log k_{2+3} ~N (-0.47, 0.18^2) giving $\overline{k}_{2+3}$ = 0.36 md.

$$k_1\alpha_1 + k_{2+3}(1-\alpha_1) = k \tag{4.11}$$

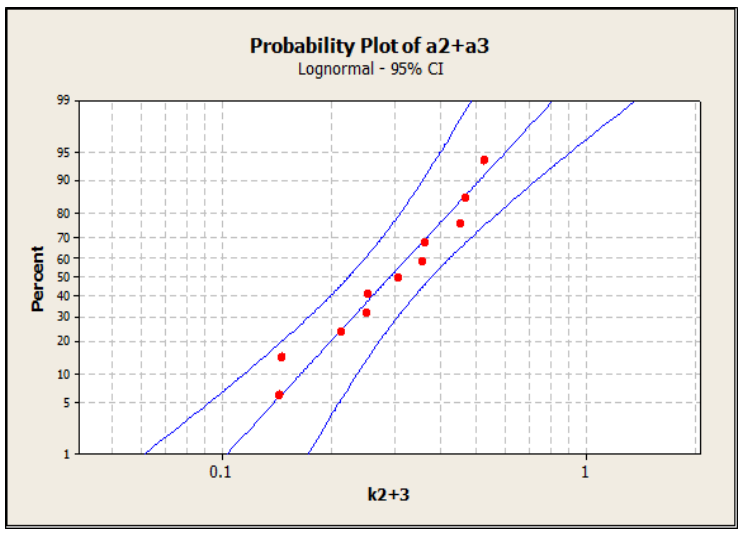

Figure 4.20. Probability plot of probe permeability from second and third facies (corrected for shale content) in the Cardium A.

After the facies proportions and permeability distributions were determined, we calculated k_{along} and k_{across} for the Cardium A and B whole core samples and compared these values to the measured whole core values. The k_{along} match well with core k_{90} and k_{max} at most intervals (R^2 > 0.8 for 1:1 line) (Fig. 4.21A). The k_{across} values show a weaker correlation with k_{vert} (Fig. 4.21B).

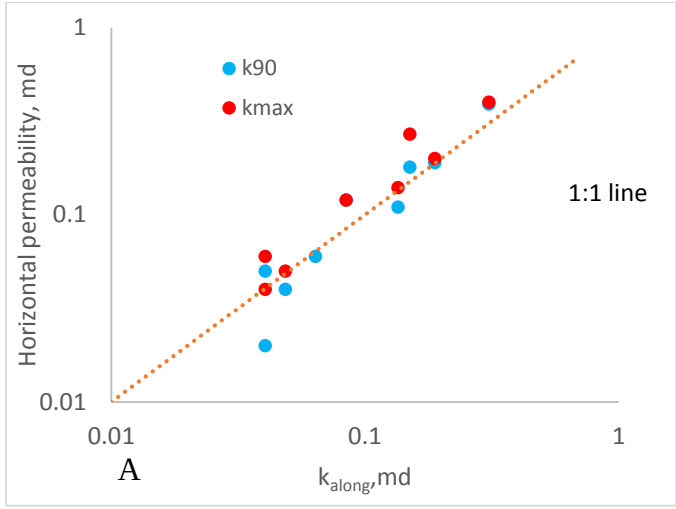

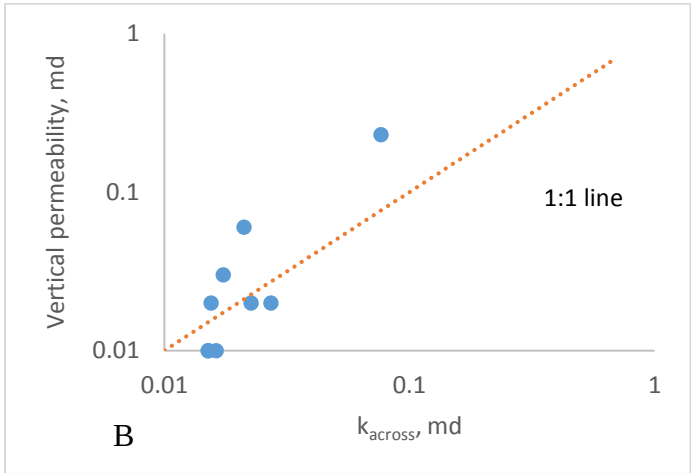

Figure 4.21. A) k_{along} versus k_{max} and k_{90}; B) k_{across} versus k_{vert} in the Cardium A.

Compared to the literature NMR permeability interpretation models, TIM and SDR, the most prominent advantage of our model is to more accurately predict directional permeability. The TIM and SDR permeabilities (k_{TIM} and k_{SDR}) give poor correlations with core results in this tight formation ($R^2 < 0.1$) (Figs. 4.22 A and B). But our model gives fair to good estimates for both horizontal and vertical permeability. Another advantage of this model is to bridge the scale differences between probe and whole core permeability.

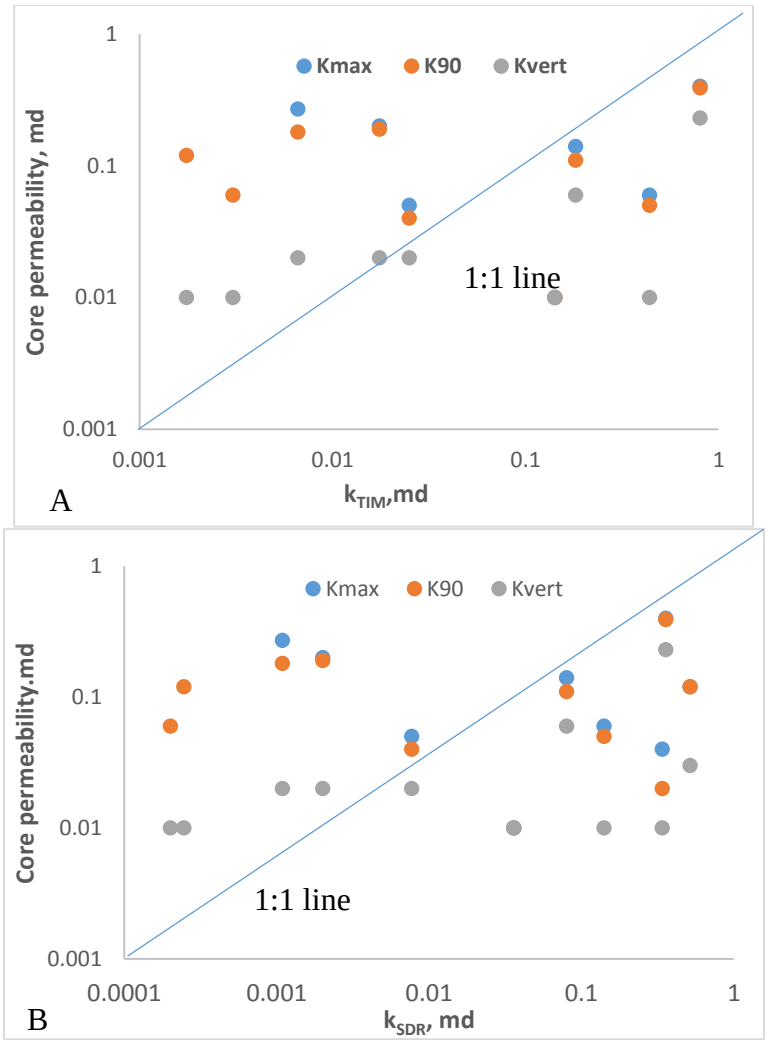

Figure 4.22. A) k_{TIM} versus core permeability; B) k_{SDR} versus core permeability in the Cardium A.

Using the probe permeability as a reference brings uncertainties. For example, even in the pure shale intervals, the k_p values are still variable. When we calculate the arithmetic and harmonic permeability, expected values are used to represent these distributions. However, expectations do not fully represent all the information of the probe permeability.

We used Monte Carlo to assess the effects of uncertainties in the values of k_1 and k_{2+3}, as reflected in the distributions of k_p, on the values of k_{along} and k_{across}. With the specified distributions log k_1~ N (-1.88, 0.24^2) and log k_{2+3}~N (-0.47, 0.18^2), an arbitrary number of observations can be generated using a computer random number generator. In this study, we chose 100 observations to compare with core results. For example, there is one

sample in which the horizontal core permeability k_{max} = 0.14 md and k_{90} = 0.11 md. Using Monte Carlo, 100 k_{along} estimates were created and compared with the core results. About 11% of k_{along} values are higher than k_{max} and 7% of them are lower than k_{90} (Fig. 4.23). Most (82%) of the k_{along} estimates locate between the k_{max} and k_{90}. For another sample, the permeability is very low (<0.1 md). About 20% the estimates are higher than k_{max} and 20% lower than k_{90}, (Fig. 4.24). These results suggest that our model is predicting values usually higher than k_{90}, but smaller than k_{max}.

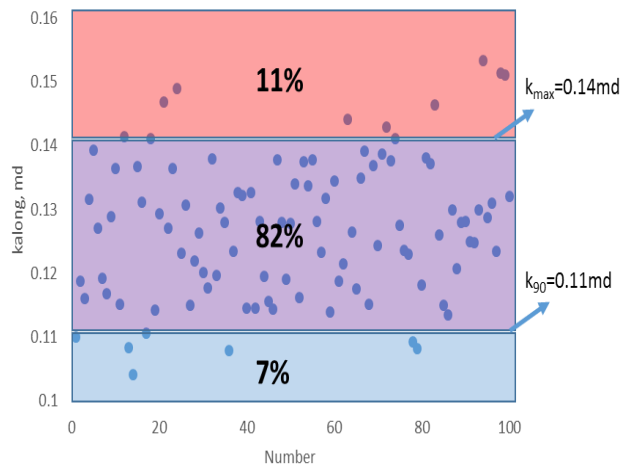

Figure 4.23. 100 k_{along} values created by Monte Carlo in the Cardium A.

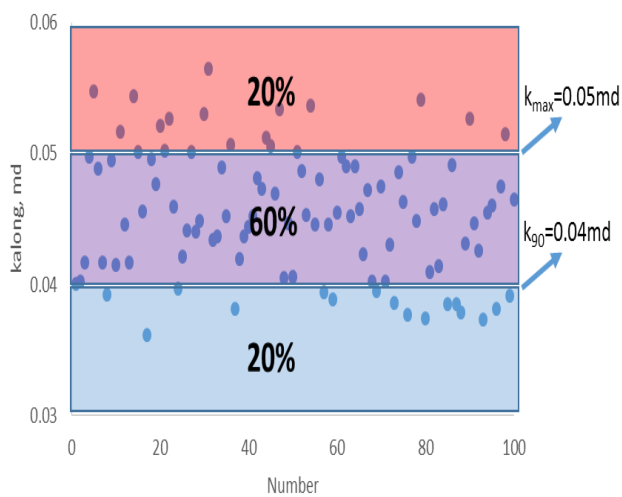

Figure 4.24. 100 k_{along} created by Monte Carlo in the Cardium A.

The same Monte Carlo process was repeated in the Cardium B. The probe permeability measurements from specific facies also exhibited LNDs, with log k_1~ N (-1.4, 0.18^2) and log k_{2+3}~ N (-0.46, 0.30^2) respectively. k_{along} and k_{across} were calculated and compared to core results. The correlations between model and core results are weaker than in the Cardium A, and it seems that there are two relations for each flow direction (Figs. 4.25 A and B). Because of the limited number of core measurements, it is difficult to determine the exact nature of these relationships and their causes. For k_{along} and k_h, Relation 2 is where the model results are very close to the core measurements, with observations distributed uniformly below and above core permeability (Fig. 4.26). Relation 1 is where the model results underestimate the core values by an order of magnitude. For k_{across} and k_{vert}, there also seem to have two relations, but all model results underestimate the core measurements. Monte Carlo analyses support this. All 100 k_h observations are smaller than the vertical core measurements (Fig. 4.27).

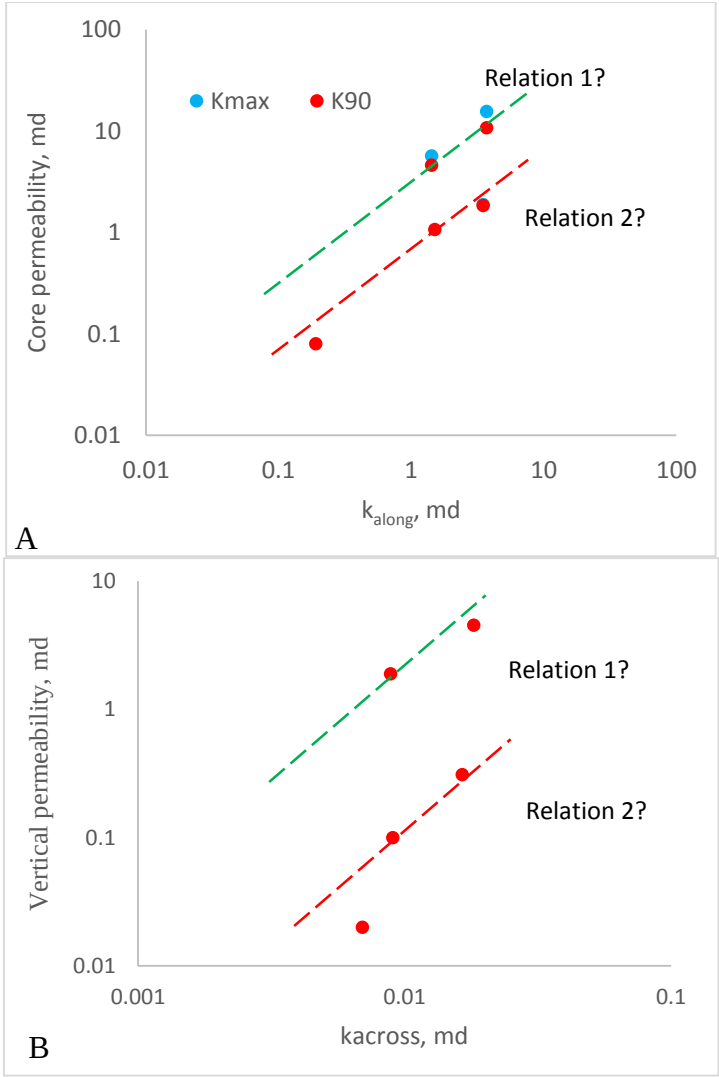

Figure 4.25. A) k_{along} versus horizontal core permeability (k_{max} and k_{90}) in the Cardium B; B) k_{across} versus vertical core permeability (k_{vert}) in the Cardium B.

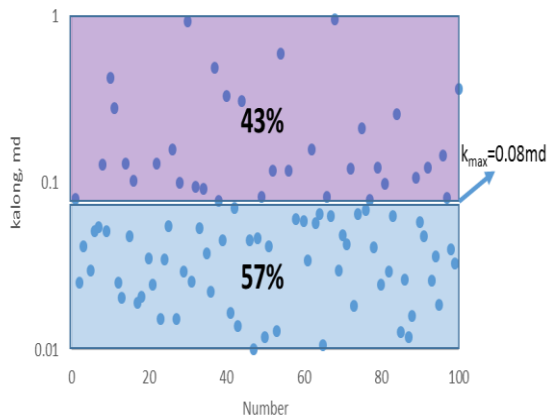

Figure 4.26. 100 k_{along} values created by Monte Carlo in the Cardium B.

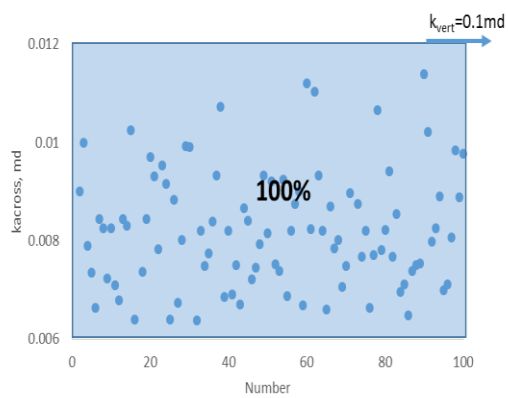

Figure 4.27. 100 k_{across} values created by Monte Carlo in the Cardium B.

4.6 Discussion

In obtaining the preceding results, we made several assumptions and approximations.

1) Some whole core permeability measurements are recorded as <0.01 md, which is the lower limit of measurement. We chose 0.01 md for these samples, which improved the quality of our k_{vert} predictor.

2) The NMR T_2 relaxation time is directly proportional to the pore size, without considering the fluid effect. Actually, in the Cardium, the fluids affecting the NMR measurements are light oil or water. Because of the similar viscosities of light oil and water, we think the effects are not significant.

3) We assumed that the main cause of permeability anisotropy is from the laminations. For the Cardium A, the cores are usually shale and siltstone laminations, corresponding well with this assumption. But in the Cardium B, the facies consists of a conglomerate and shale mixture, which is not consistent with the laminated layered system. This is one possible reason that we obtain a weaker relation between the model and core results in the Cardium B than the Cardium A.

4) We used a three-facies model in accord with the three peaks we often observed in the T_2 spectra. In tight formations, it can be very difficult to separate the fine and siltstone components (i = 2 and 3 facies in our model). So we assumed they are one lithotype but this decreases the match quality with k_{across}.

5) Only the first peak (α_1) was verified by the core and literature samples. In this study, all first components represent micro-porosity facies, because $\mu_1 < 0.6$. If we were analyzing NMR spectra for a conventional reservoir, the first component might not be caused by micro-pores. For example, in a clean sandstone sample, the first peak would correspond to relatively large pores, which should have a higher μ_1.

4.7 Conclusions

This research presented a new approach to interpret the NMR well log in tight formations. The NMR log T_2 was divided into at most three Gaussian components, which represent different pore sizes. The parameters (α_i, μ_i, and σ_i for i = 1, 2, and 3) from the decomposition have specific geological meanings. The literature samples and the Cardium core data, including core image analysis and XRD results, showed that α_1 correlates well with shale volume proportions. Some probe permeability measurements were chosen for the pore size-related facies model. Arithmetic and harmonic permeability values were calculated and compared to whole core horizontal and vertical measurements. Our permeability predictions showed moderate to strong correlations with core results. Compared to the literature models, the proposed model performed better. Monte Carlo analysis further confirmed the agreement between core and model results, especially in the Cardium A. Because of limited samples and complicated facies in the Cardium B, the agreement was weaker than for the Cardium A.

CHAPTER 5: SUMMARY, CONCLUSIONS, AND FURTHER WORK

5.1 Summary

This work has discussed different permeability prediction methods based on a tight Cardium Formation dataset from one well in the Edson Field. The main results are listed below:

1. The Cardium Formation in the research well is divided into the Cardium A and Cardium B. The high permeabilities (> 0.1 md) come from a small part of conglomerate and relatively clean siltstone in the Cardium A. The remaining parts of the Cardium A Formation have lower permeability, ~0.01 md. In the Cardium B, the conglomerate shows high permeabilities (> 0.1 md) while the shale has low permeability (~0.01 md).
2. In the Cardium A, the whole core porosity (ϕ) shows a weak correlation with whole core permeabilities (k_{max}, k_{90} and k_{vert}) of shaly siltstone, which indicates that the porosity is not the unique factor controlling permeability. The anisotropy (k_{vert} /k_{90}) reaches the largest at the medium porosity ~ 6%. Below and above this porosity, the anisotropy decreases. The correlation between ϕ and k in the Cardium B is stronger. The anisotropy shows an increasing trend with the porosity.
3. Clay minerals are measured using XRD at five samples. 11cm×3cm grids are chosen to measure probe permeabilities at every XRD location. The permeability decreases with increasing XRD clay contents in the silt interval.
4. The GR and spectral GR well logs show strong relationships with XRD clay measurements, which provide the basis for predicting permeability with the SGR or GR. Both GR and SGR logs however show negative mild correlations with permeability. The potassium log is the best permeability predictor.
5. There are no identifiable trends between conglomerate permeability and GR and SGR logs. Ten 1cm×1cm “windows” centered by the probe location were chosen from the conglomerate core image. The grain size, number, and location between the probe and grain surface best related to conglomerate permeability.

6. Complicated facies make the probe permeability values appear to be randomly distributed in the Cardium Formation, with neither a normal nor log-normal distribution. If we divide the Cardium Formation into different intervals according to the facies, the probe permeability shows a clear log-normal distribution in each interval.
7. Both the Cardium A and the Cardium B permeability are heterogeneous or very heterogeneous ($C_v > 1$). According to Corbett and Jensen's (1993) recommended rule, the actual probe measurment number (N_{actual}) is larger than the guideline requirement (N_{recc}) in the Cardium A. The N_{actual} is smaller than the N_{recc} in the Cardium B. The implications of this are that the probe permeabilities provide reliable measurements for the Cardium A, but cannot cover all the information in the Cardium B.
8. Experimental design helped to identify the deep resistivity (A090) and the deep resistivity (A090)-gamma ray (GR) combination as being one- and two-factor variables for permeability prediction in the Cardium A. The relationships are more complex in the Cardium B, and no single factor shows a significant relationship with the permeability. The combined potassium and thorium, gamma and photoelectric logs show more important influences on the permeability than other well log measurements.
9. For more than three well log factors, Yao and Holditch (1993) presented a model, including porosity, deep and shallow resistivities, and GR to calculate permeability. The model works best in the Cardium A shaly siltstone interval, with $R^2 = 0.94$. Shale and conglomerate show relatively weak correlations between the model and core measurements, with $R^2 < 0.5$.
10. Semivariograms (SV) characterize the cyclicity and consistency between permeability and well logs. Cyclicities of 0.2m and 1.3m wavelengths were identified in the permeability and GR log data, corresponding to bed and channel geological factors.
11. We developed a new approach for permeability prediction using the NMR log. The NMR log (T_2) was divided into at most three Gaussian components, which represent lithofacies with different pore sizes. The parameters (α_i, μ_i, and σ_i for i

= 1, 2, and 3) from the decomposition have specific geological meanings. The literature samples and the Cardium core data, including core image analysis and XRD results, showed that α_1 correlates well with shale volume proportions.

12. Some probe permeability measurements were chosen for the pore size-related facies model. Arithmetic and harmonic permeability values were calculated and compared to whole core horizontal and vertical measurements. Our permeability predictions showed moderate to strong correlations with core results. Compared to the literature models, the proposed model performed better. Monte Carlo analysis further confirmed the agreement between core and model results, especially in the Cardium A. Because of limited samples and complicated facies in the Cardium B, the agreement was weaker than for the Cardium A.

5.2 Future Work

This work provides a fundamental discussion about the traditional methods for the permeability characterization and prediction in first three Chapters. In Chapter 4, we try to use an innovative NMR based model to predict the permeability, which needs lots of work to improve.

1. Develop our models and methods further so they have fewer assumptions. Examples of assumptions are
    a. We assume the borehole fluids in our samples are not significant to our results. If possible, compare the lab NMR measurement on core sample saturated with brine water with NMR logging result.
    b. We do not have pure clean siltstone. If possible, use real clean siltstone to decrease the uncertainty.
    c. If the pressure differences between probe and whole core permeability measurements affect our model accuracy.
2. Further test our models – what have we overlooked or ignored? For example, the difference between probe and whole permeability caused by principle of measurements. If this difference has significant effect on the model result?

3. Extend the model so it can perform better or be applicable to other formations. For example, should we consider combining the resistivity, potassium, and NMR logs to predict permeability?
4. In the Cardium B, our model showed that there are two possible relationships between predicted and measured permeability. The lack of sampling (only 5 samples) increases prediction uncertainty. More conglomerate samples collection may help to solve this problem.
5. Well log (including NMR) based predictions for core permeability highly depend on the accuracy of core-log depth shifting. In this study, we tried same measurements (core and log GRs) and corresponding factors (e.g., core porosity and density) to help depth shifting. Also we chose some homogenous samples to text our shifting. The sample we used is relative small scale (0.5 m). I recommend if possible, choosing a larger or more samples to test will be better.
6. Besides the NMR model, Yao and Holditch model works well in our shaly siltstone intervals. In shale and conglomerate intervals, the model results become weak. We can see from the parameter that the porosity shows a negligible or no effect on them. Is it caused by the homogenous density porosity of the shale? If we use more accurate porosity measurement, not well log derived, will we get a better result?

REFERENCE

Abdulla, K., 2013, Middle Bakken wettability evaluation using NMR T_2 forward modelling and mineralogy: MSc thesis, p.36-41.

Agterberg, F.P., 1974, Geomathematics: Elsevier, p. 235.

Aguilera, R., 2002. Incorporating capillary pressure, pore aperture radii, height above free water table, and Winland r35 values on Picket plots: AAPG Bulletin, v 86, p.605-624.

Aguilera, R., 2014. Flow Units: From Conventional to Tight-Gas to Shale-Gas to Tight-Oil to Shale-Oil Reservoirs: SPE Reservoir Evaluation & Engineering, 17(2): 190-208.

Bansal, A., Xu, C.C., and Verdin, C.T, 2013, Improved petrophysical evaluation of consolidated calcareous turbidite sequences with multi-component induction, magnetic resonance, resistivity images, and core measurements: SPWLA 54th Annual Logging Symposium, New Orleans, USA.

Berg, R.R., 1970. Method for determining permeability from reservoir rock properties: Transactions Gulf Coast Association of Geological Societies, v. 20, p. 303–317.

Carman, P.C., 1939. Permeability of saturated sands, soils and clays: Journal of Agricultural Science, 29:263-273.

Chunyan, J., Shunli, H., Shusheng, G., Wei, X., Huaxun, L., and Yuhai, Z., 2013, The Characteristics of Lognormal Distribution of Pore and Throat Size of a Low Permeability Core: Petroleum Science and Tech., vol. 31, p.856-865.

Clarkson, C. R., Jensen, J. L., Pedersen, P. K., and Freeman, M., 2012. Innovative Methods for Flow-Unit and Pore-Structure Analysis in a Tight Siltstone and Shale Gas Reservoir: AAPG Bulletin, v. 96, pp 355-374.

Clarkson, C.R., Jensen, L.J., and Chipperfield, 2012, Unconventional gas reservoir evaluation: What do we have to consider? : J Natural Gas Sci and Eng, vol. 8, p. 9-33.

Clarkson, C.R., Pedersen, P.K. 2011. Production Analysis of Western Canadian Unconventional Light Oil Plays. In: Society of Petroleum Enginners: Conference paper. Canadian Unconventional Resources Conference, Calgary, Alberta, November 15-17, 2011.

Coates, G.R. and Dumanoir, J.L., 1973. A new approach to improve log derived permeability: SPWLA, Transactions 14th Annual Logging Symposium. P.27.

Coates, G.R., Xiao, L., and Prammer, M.G., 1999, NMR logging principles and applications: Halliburton Energy Services, Houston, 233p.

Coates, R., Miller, N. Gillen, M. and Henderson, G., 1991, An investigation of a new magnetic resonance imaging log: 32th Annual Logging Symposium, paper DD.

Collins, E., 1952, Determination of the transverse permeabilities of large core samples from petroleum reservoirs: J. App Physics, vol. 6, p. 681-684

Collins, R.E. and Jordan, J.K., 1961. Porosity and permeability distribution of sedimentary rocks: Society of Petroleum Engineers Journal.

Connolly, J.R., 2010. Introduction Quantitative X-Ray Diffraction Methods: http://epswww.unm.edu/media/pdf/09-Quant-intro.pdf.

Corbett, P., and Jensen, L. L., 1992, Variation of Reservoir Statistics According to Sample Spacing and Measurement Type for Some Intervals in the Lower Brent Group: The Log Analyst vol.33, p. 22-41.

Corbett, P.W.M. and Jensen, J.L., 1993. Quantification of heterogeneity, a role for the minipermeameter in reservoir characterization: Characterisation of Fluvial and Aeolian Reservoirs, C. P. North and D. J. Prosser (eds.), The Geological Society Spec. Publ. No.73, London, p433-442.

Daigle, H. and Dugan, B., 2009, Extending NMR data for permeability estimation in fine-grained sediments: Marine and Petroleum Geology, vol. 26, p. 1419-1427.

Diamond, S. and Dolch, W. L., 1971, Generalized Log-Normal Distribution of Pore Sizes in Hydrated Cement Paste: Colloid and Interface Science, vol.38, 234-244.

Everett, D.H., 1972 IUPAC, Manual of Symbol and Terminology for Physico -chemical Quantities and Units, Appendix, Definitions, Terminology and Symbols in Colloid and Surface Chemistry, Part I, Pure Appl. Chem., Vol. 31(4), p. 579.

Fisher, R.A., 1935, The design of experiments, Edinburgh: Oliver and Boyd.

Genty, C., Jensen, L.J, and Ahr, M., 2007, Distinguishing carbonate reservoir pore facies with nuclear magnetic resonance measurements: Natural Resources Research, vol.16, p.44-54.

Georgi, D.T., Jones, S.C., 1992, Application of pressure-decay profile permeametry to reservoir description: 16th Annual Society of Petroleum Engineers International Conference and Exhibition, paper SPENC 9212.

Goggin, D.J., Chandler, M. A., Kocurek, G., and Lake, L.W., 1988, Patterns of permeability in eolian deposits: Page Sandstone (Jurassic), northeastern Arizona: SPE Formation Evaluation, vol. 3, p. 297-306.

Jensen, J.L., Corbett, P.W.M., Pickup, G.E., Ringrose, P.S., 1996. Permeability semivariograms, geological structure, and flow performance: Mathematical Geology, 28(4): 419-435.

Jones, S.C., 1994, A new, fast, accurate pressure-decay probe permeameter: SPE Form. Eval, vol. 9, p.193-199.

Jones, S.C., 1994. A New, Fast, Accurate Pressure-Decay Probe Permeameter: SPE Formation Evaluation, 9 (3): 193-199.

Kenyon, W.E., Day, P.I., Stracley, C. et al, 1988, A three-part study of NMR longitudinal relaxation properties of water-saturated sandstones: SPE Form Eval, vol.3, p.622-636.

Kozeny, J., 1927. ‘‘Ueber kapillare Leitung des Wassers im Boden: Wien, Akad. Wiss., 136(2a), 271.

Krause, F.F., Deutsch, B., Jonier, D. et al., 1994, Cretaceous Cardium Formation of the Western Canada Sedimentary Basin: Canadian Soc. of Petroleum Geologists and Alberta Research Council, Special Report 4.

Krause, F.F., Deutsch, K.B., Joiner, S.D., Barlcay, J.E., Hall, R.L., Hills, L.V., 1994.Cretaceous Cardium Formation of the Western Canada Sedimentary Basin: Geological Atlas of theWestern Canada Sedimentary Basin, G.D. Mossop and I. Shetsen (comp.), CanadianSociety of Petroleum Geologists and Alberta Research Council, Special Report 4, URL http://www.ags.gov.ab.ca/publications/wcsb_atlas/a_ch23/ch_23.html.

Krumbein, W.C. and G.D. Monk, 1942. Permeability as a function of the size parameters of unconsolidated sand, Petr. Tech., 153-16.

Law, J., 1944. A statistical approach to the interstitial heterogeneity of sand reservoirs, Technical Publication 1732, Petroleum Technology 7, May 1944.

Levine, D.M., Ramsey, P.P., Smirt, R.K., 2001, Applied statistics for engineers and scientists: Upper Saddle River, New Jersey, Prentice Hall, p. 530-535.

Lim, J.S. AND Kim, J., 2004. Reservoir porosity and permeability estimation from well logs using fuzzy logic and neural networks: SPE Asia Pacific Oil and Gas conference and Exhibition, Australia, SPE 88476.

Lindquist, W.B, Venkatarangan, V., Dunsmuir, J., Wong, T.F., et al., 2000, Pore and throat size distributions measured from synchrotron X-ray tomographic images of Fontainebleau sandstones: J. Geophysical Research, vol.105, p.1-32.

Lowden, B., 2003, A new method for separating lithologies and estimating thickness-weighted permeability using NMR logs: SPWLA 44th Annual Logging Symposium, paper SPWLA-2003-FFF

Mageau, L., Zack, K., Bouchard, J., Stevenson, M., Steppan, G., Urness, G. 2012. Assessing the Cardium`s Second Generation- A Look at Horizontal Well Performance by Area. Energy, Raymond James. Pp. 1-111.

Meyer, R., and Krause, F.F., 2001, A comparison of plug-derived and probe-derived permeability in cross-bedded sandstones of the Virgelle Member, Alberta, Canada: The influence of flow directions on probe permeametry: AAPG Bulletin, vol.85, p.477-489.

Minh, C.C., and Sundararaman, P., 2006, NMR petrophysics in thin sand-shale laminations: SPE Ann. Tech. Conf. and Exhib. SPE-102435.

Mohaghegh, S., Balan, B., Ameri, S., 1997. Permeability determination from well log data: SPE Formation Evaluation, 12 (3):170-174.

Morris, R.L. and Biggs, W.P., 1967. Using log-derived values of water saturation and porosity: Transactions of the SPWLA 8th Annual Logging Symposium, paper X, 26p.

Nisael, A.S., Clarkson, C.R., Krause, F.F., 2012. Quantification of cm-Scale Heterogeneities in Tight-Oil Intervals of the Cardium Formation at Pembina, WCSB, Alberta, Canada: SPE-162837-MS.

Ostroff, G.M, Shorey, D.S, and Georgi, D.T., 1999, Integration of NMR and conventional log data for improved petrophysical evaluation of shaly sands:SPWLA 40th Annual Logging Symposium.

Rider, M., and Kennedy, M., 2011. The Geological Interpretation of Well Logs (third version), Chapter 2.

Saner, S., Kissami, M., Nufaili, S.A., 1997. Estimation of permeability from well logs using resistivity and saturation data: SPE Formation Evaluation, 12 (3): 27-31.

Shepherd, R.G., 1989. Correlations of Permeability and Grain Size: Ground Water, 27(5) pp 633-638.

Shi, D., Brown, P.W., and Ma, W., 1991, Lognormal simulation of pore size distributions in cementations materials: J. Am. Ceramic Society, vol.74, p.1861-1867.

Timur, A. 1968. An investigation of permeability, porosity, & residual water saturation relationships for sandstone reservoirs: The Log Analyst IX (4). SPWLA-1968.

Tixier, M.P., 1949. Evaluation of permeability from electric-log resistivity gradients: Oil and Gas J., 113.

Wyllie, M.R.J. and Rose, W.D., 1950. Some theoretical considerations related to the quantitative evaluation of the physical characteristics of reservoir rock from electric log data: Trans., AIME, vol. 189, pp.105.

Xiao, L., Mao, Z., and Yan, J., 2012, Calculation of irreducible water saturation (S_{wirr}) from NMR logs in tight gas sands: Appl Magn Resonance, vol. 42, p.113-125.

Xue, G.P., Gupta, A.D., Valko, P., Blasingame, T., 1997. Optimal transformations for multiple regression: application to permeability estimation from well logs: SPE Formation Evaluation, 12 (2): 85-93.

Yao, C.Y. and Holditch, S.A., 1993. Estimating Permeability Profiles Using Core and Log Data: SPE 26921.

APPENDIX 1

CDF: Cumulative distribution function is F(x), which is defined by $F(\mathrm{x}) = \mathrm{Prob}(\mathrm{X} \leq \mathrm{x})$. F(x) is the probability of a random variable X, which is small or equal to x (Jensen, et.al, 2000).

PDF: For a CDF F(x), which is defined as $F(\mathrm{x}) = \int_{-\infty}^{x} f(\mathrm{t})\,\mathrm{dt}$. The function f (t) is the probability distribution function.

ND: Normal (or Gaussian) distribution is a very common statistical concept, which has following PDF: $f(\mathrm{x};\sigma,\mu) = \frac{1}{\sqrt{2\pi\sigma^2}} \exp\left[-\frac{(\mathrm{x}-\mu)^2}{2\sigma^2}\right]$.

LND: Log-normal Distribution is a continuous PDF of a variable whose logarithm is ND.

APPENDIX 2

Probability plot (Chambers et al., 1983) is a direct method to test whether or not a variable follows a specific distribution. In this thesis, we use probability plots (Figs. 3.1, 3.2, 3.4, 3.5, 4.19, and 4.20) to evaluate probe permeability distribution. Variable data points are plotted against a given distribution (such as normal). If these points show a straight line, it means the variable follows the given distribution.

We use Minitab to produce these probability plots. Here is one sample plot (Fig. 3.1) from the content. In this plot, we assumed the variable normal distributed. The middle blue line which is the fitted distribution line. If these data points follow the straight line, it means that the variable is a normal distribution. Because it is only an assumed fitting line, the value of this line can reach to negative values. The two curved blue lines display approximate 95% confidence intervals.

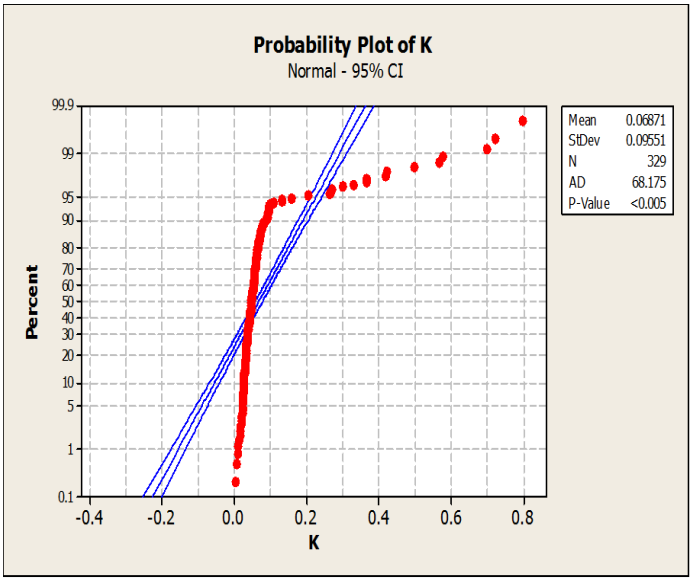

Figure 3.1. Probability plot of k in the Cardium A

APPENDIX 3

In order to gain the most information with the least effort, experimental design is one useful method. The idea for the design of experiment was first developed by Fisher in 1935. The experimental design method is used to select potential well log which has effect on permeability in this thesis. The results are shown in Figures 3.6 and 3.7 from Minitab. The following Equations (Levine et al., 2001) explain how these figures plotted: Assuming there are two impact variables (A and B) and one response variable (X), we define the following terms:

r = the number of levels of factor A

c = the number of levels of factor B

n' = the number of values (replications) for each cell

n = the total number of observations in the experiment

X_{ijk} = the value of k th observation for level i of factor A and level j of factor B

$$\overline{\overline{X}} = \frac{\sum_{i=1}^{r}\sum_{j=1}^{c}\sum_{k=1}^{n'} X_{ijk}}{rcn'}$$ is the overall mean

$$\overline{X_{i.}} = \frac{\sum_{j=1}^{c}\sum_{k=1}^{n'} X_{ijk}}{cn'}$$ is the mean of the i th level of factor A(where i =1,2….r)

$$\overline{X_{.j}} = \frac{\sum_{i=1}^{r}\sum_{k=1}^{n'} X_{ijk}}{rn'}$$ is the mean of the j th level of factor B(where j =1,2….r)

$$\overline{X_{ij}} = \sum_{k=1}^{n'} \frac{X_{ijk}}{n'}$$ is the mean of the cell ij , the combination of the i th level of factor A and j th level of factor B

The Among-group variation, which also called the sum of squares among groups (SSA). It represents the observation difference caused by factor A. The SSB and SSAB mean the difference due to B and AB. They are calculated by the Equations A-1, A-2 and A-3 (Levine et al., 2001).

$$SSA = cn' \sum_{i=1}^{r} (\overline{X_{i.}} - \overline{\overline{X}})^2 \quad \text{(A-1)}$$

$$SSB = rn' \sum_{i=1}^{r} (\overline{X_{.j}} - \overline{\overline{X}})^2 \quad \text{(A-2)}$$

$$SSAB = n' \sum_{i=1}^{r} \sum_{j=1}^{c} (\mathrm{X}_{ij} - \overline{X_{i.}} - \overline{X_{.j}} + \overline{\overline{X}})^2 \quad \text{(A-3)}$$

The effect of each factor (such as A) on the observation can be obtained using Equation A-4 (Levine et al., 2001).

$$Effect = \sqrt{\frac{SSA}{n' 2^{k-2}}} \quad \text{(A-4)}$$

According to the value of calculated effect, importance from factors (signal or double) can be ranked. The CDF for an effect is obtained as follow (Eq. A-5):

$$P_i = \frac{R_i - 0.5}{2^k - 1} \quad \text{(A-5)}$$

where R_i is the ordered rank of effect i; p_i is the CDF for order effect i; k is the number of factors.

The probability plot of different factors can be plotted with calculated p_i.